THESIS FOR THE DEGREE OF DOCTOR OF PHILOSOPHY

Synthesis and Applications of Colloidal Zeolites and Transition Metal Functionalized Ordered Mesoporous Carbons

WALTER JULIAN ROSAS ARBELAEZ

Department of Chemistry and Chemical Engineering

CHALMERS UNIVERSITY OF TECHNOLOGY

Gothenburg, Sweden 2020

Synthesis and Applications of Colloidal Zeolites and Transition Metal Functionalized Ordered Mesoporous Carbons

WALTER JULIAN ROSAS ARBELAEZ
ISBN 978-91-7905-403-8

Doktorsavhandlingar vid Chalmers Tekniska Högskola
Ny serie nr. 4870
ISSN 0346-718X

Department of Chemistry and Chemical Engineering
Chalmers University of Technology
SE-412 96 Gothenburg
Sweden
Telephone + 46 (0)31-772 1000

Cover:
A visual representation of the two types of porous materials investigated in this thesis: zeolites and mesoporous carbons. On the left hand side, a representation of solution equilibria between the silicate species in solution and the colloidal zeolites pointing towards a SEM image of actual colloidal silicalite-1 particles. The SEM points toward a sphere consisted of colloidal zeolite articles assembled and a representation of a cellulose-zeolite foam. On the right hand side, a representation of the iron- and carbon-nitrogen precursors that form graphene-like sheets that contain iron chelating active sites and this points to a TEM image of an actual ordered mesoporous carbon that points to a polarization curve obtained from PEMFC test.

Printed at Chalmers Reproservice
Gothenburg, Sweden 2020

Synthesis and Applications of Colloidal Zeolites and Transition Metal Functionalized Ordered Mesoporous Carbons

WALTER JULIAN ROSAS ARBELAEZ

Department of Chemistry and Chemical Engineering
Chalmers University of Technology

ABSTRACT

Porous materials have attracted a great deal of attention of the materials science community, owing to their physical and chemical properties including high surface areas, narrow pore size distribution, tunable pore diameters and variety of chemical compositions. These properties make them suitable for various applications such as adsorption, sensing, catalysis, energy, carbon capture and drug delivery. Zeolites and carbons are among the most commonly and extensively investigated porous materials. Zeolites are crystalline microporous aluminosilicate structures with multidimensional channel systems. During the last decades, they have been broadly used and studied in the fields of chemical synthesis and applications such as ion exchange, gas separation and catalysis. Due to the high demand for these materials in the chemical industry and their unique characteristics, there is still a need for understanding their formation in order to develop new synthetic methods and tailor their properties for specific target-oriented applications.

In this thesis, colloidal zeolite particles were prepared, studied and further utilized in two applications. One of the first goals was to understand the formation of colloidal zeolites and more specifically the premature termination of their growth during synthesis. A pH-dependent equilibrium between the condensation and dissolution reactions is presented in this thesis to explain this behavior. By a controlled decrease in pH of the synthesis mixtures, it was possible to shift the equilibrium towards condensation and to favor the increase in particle size and reach full conversion. We showed that it is possible to cycle between zeolite growth and dissolution by cyclic acid and base adjustments of the pH. In addition, we gained new insights about the duration of the nucleation stage. Likewise, the chemical solution equilibria growth mechanism was studied in the synthesis of colloidal ZSM-5 particles, and besides observing an increase in the particle size and conversion yield, shifting the dynamic pH-dependent equilibrium led to an improved incorporation of aluminum into the zeolite framework.

As the second goal in this thesis, we used the colloidal zeolite particles for the preparation of two new materials: a hybrid zeolite-cellulose foam for CO_2 capture and hierarchical micro-/mesoporous zeolite microspheres. The hybrid foams were produced by mixing colloidal silicalite-1 particles and cellulose nanofibrils/gelatin and applying a freeze-casting. The foams exhibited ultra-high loading of silicalite-1 particles and a linear relationship between the silicalite-1 and the CO_2 adsorption capacity with a selectivity towards CO_2-over-N_2. In addition, a novel mesoporogen-free evaporation-driven colloidal assembly was developed to prepare mesoporous silicalite-1 microspheres. The synthesized materials exhibited interconnected porosity, high pore volume, and the method can be used with other colloidal particles to tailor the pore size, pore volume and surface area. Moreover, the method does not require long preparation times or high temperature which has a positive effect on production at industrial scale.

Porous carbon materials have received growing interest due to their unique properties, including porosity, high surface areas, low density and electrical conductivity. Here, special attention has been casted on the development of N-doped mesoporous carbon for energy conversion in fuel cell technologies. Numerous efforts have been devoted to developing inexpensive platinum-free catalysts, active towards oxygen reduction reaction (ORR). In this thesis, we synthesized Fe-N-doped ordered mesoporous carbon (OMC) materials using different types of iron salt and studied the effect of the counter anion on their structural and catalytic properties. Although the change of the anion led to a significant increase in the Fe content in the resultant Fe-N-OMC, it was found by rotating disc electrode (RDE) and fuel cell measurements, that such increase does not provide an noticeable improvement in the rate of ORR, suggesting that the additional fraction of iron consists of less active Fe species.

Keywords*: colloidal zeolites; growth mechanism; hierarchical zeolites; CO_2 capture; Fe-N-doped ordered mesoporous carbon; fuel cell*

LIST OF PUBLICATIONS

This thesis is based on the work described in the following papers.

1. Establishing the Role of Solution Equilibria in Zeolite Growth
   Walter Rosas-Arbelaez and Anders E.C. Palmqvist
   To be submitted for publication 2020

2. Solution Equilibria-Controlled Growth of Colloidal Zeolite ZSM-5
   Walter Rosas-Arbelaez and Anders E.C. Palmqvist
   To be submitted for publication 2020

3. Hierarchical Micro-/Mesoporous Zeolite Microspheres Prepared by Colloidal Assembly of Zeolite Nanoparticles
   Walter Rosas-Arbelaez, Andreas J. Fijneman, Heiner Friedrich and Anders E.C. Palmqvist
   RSC Advances, 2020, 10 (60), 36459-36466

4. Bio-based Micro-/Meso-/Macroporous Hybrid Foams with Ultrahigh Zeolite Loadings for Selective Capture of Carbon Dioxide
   Luis Valencia*, Walter Rosas*, Andrea Aguilar-Sanchez, Aji P. Mathew and Anders E.C. Palmqvist
   ACS Appl. Mater. Interfaces 2019, 11, 43, 40424–40431
   *Authors contributed equally to this work

5. Influence of Iron Salt Anions on Formation and Oxygen Reduction Activity of Fe/N-Doped Mesoporous Carbon Fuel Cell Catalysts
   Samuel J. Fretz, Caroline Janson, Walter Rosas-Arbelaez and Anders E.C. Palmqvist
   ACS Omega 2019, 4, 18, 17662–17671

CONTRIBUTION REPORT TO THE LISTED PUBLICATIONS

1. Performed all experimental work. Shared data analysis and writing of the manuscript

2. Performed all experimental work. Shared data analysis and writing of the manuscript.

3. Responsible for all the experimental work and all the data analysis and most of the writing.

4. Responsible for the synthesis of the colloidal zeolites, the analysis of CO_2 adsorption, specific surface area, and scanning electron microscopy of the zeolites and the hybrid foams as well as data analysis of the same characterization techniques. Responsible for writing approximately half of the manuscript and contributing with the comments regarding the whole manuscript.

5. Responsible for the rotating disk electrode experiments, the SAXS measurements and supporting the fuel cell tests. Responsible for the data analysis and discussion of RDE and SAXS, and partly of fuel cell testing and supported in writing of the manuscript.

PUBLICATIONS NOT LISTED IN THIS THESIS

I. Correlated atomic-scale compositions, structures, and reduction activities of non-precious-metal mesoporous N-carbon electrocatalysts

   Shona M. Becwar, Zachariah J. Berkson, Niels P. Zussblatt, Ziyang Wei, Philipp Selter, Lele Peng, Rongli Liu, Walter Rosas Arbelaez, Anders E. C. Palmqvist, Xiangfeng Duan, Nina Fechler, Philippe Sautet, and Bradley F. Chmelka
   To be submitted for publication 2020

II. Multivalent ion-induced re-entrant transition of carboxylated cellulose nanofibrils and its influence on nanomaterials properties

   Luis Valencia, Emma M. Nomena, Susanna Monti, Walter Rosas-Arbelaez, Aji P. Mathew, Sugam Kumar and Krassimir P. Velikov
   Nanoscale, 2020, 12, 15652–15662

TABLE OF CONTENTS

This thesis is dedicated to my beloved mother Luz Marina Arbelaez
and to the best chemist, my father Carlos Rosas (R.I.P.)

"Be less curious about people and more curious about ideas"

Marie Skłodowska-Curie

1. Introduction

Porous materials are solids that contain pores, channels, or voids. In nature, there is a vast amount of porous materials such as wood, clays, zeolites, bones, biological tissues, among others, with interesting properties that have led many scientific efforts into synthesizing, studying, and mimicking such materials. Porous materials can be classified into three categories based on the pore size, according to the IUPAC[1]: microporous (aperture diameter < 2nm), mesoporous (aperture diameter of 2-50 nm), and macroporous (aperture diameter >50 nm). The porosity of such materials influences different properties including surface area, density, mechanical properties, and adsorption capabilities. The possibility of tuning these properties and the physicochemical interaction with external molecules has attracted enormous interest in catalysis, ion exchange, separation, and sensing, among others. Thus, in the last decades, many efforts have been dedicated to designing porous materials with tuned porosity and desirable surface properties along with different chemical nature (*i.e.*, inorganic, organic, and hybrid materials) that can be used in a wide range of applications from classical to cutting-edge technologies.

Zeolites are porous materials that have been extensively investigated since the development of the first synthetic zeolites in the 1940s.[2] Zeolites are mainly classified as inorganic microporous materials built with different arrangements and connections of silica and alumina tetrahedrons, leading to a great variety of zeolite framework structures, some with variable silica/alumina molar compositions, counting in up to 235 different types of both natural and synthetic zeolites.[3,4] Today, zeolites are one of the most used catalysts in the industry due to the strong acidity and molecular size, and shape-selective properties, which are exploited, *e.g.*, in oil refining and gasoline production, and in automotive aftertreatment systems as NO_x reduction catalysts.[5,6] Due to the high demand for these materials in the industry and the interest in understanding the physicochemical properties of zeolites and their performance in various applications, many efforts have been devoted to understanding their mechanism of formation and developing their synthesis methods. Zeolites are usually synthesized in batch systems under hydrothermal conditions using mixtures of silicate and aluminate solutions subject to high temperatures for specific periods of time. Several approaches have converged to a common formation mechanism from this synthesis system, comprising induction, nucleation, and growth/crystallization. Despite the positive results and efforts, there is still an incomplete understanding of the detailed processes dictating the growth and discontinuation of growth of zeolites in solution. Especially, the frequently observed termination of zeolite growth before reaching full conversion of the precursors has not been addressed to a considerable extent.

Over the years, the small pore size of zeolites has been identified as a limiting factor for some applications where diffusion plays a critical role (*e.g.*, catalysis, separation). This mass transport limitation may affect the shape-selectivity, the catalytic activity as well as its durability.[7] During the last three decades, the idea of incorporating either meso- or macropores in the porous structure has received a lot of interest since the combination of properties from both types of porosity brings up several advantages. Hierarchically structured porous zeolites have emerged as a promising alternative in which the porous structure can span different length scales from micro- to meso- and macropores. These materials are characterized by at least two levels of porosity, high surface areas, large pore accessibility, and high pore interconnectivity, which make them suitable for applications in which the transport of mass and/or ions need to be facilitated.[8] Although many hierarchical porous zeolites have been successfully developed, the optimization of interconnectivity between the different pores and the need for simple synthesis protocols that can reduce the production cost at a large scale, still represent significant challenges.

Since, zeolites are commonly obtained in aggregated powder form, their implementation in scaled-up applications such as in gas-separation systems is limited. The use of adhesives and inorganic binders to form zeolite-based materials typically leads to pore blockage and reduced gas uptake. In this context, a zeolite-composite material using a porous supporting material could potentially improve the system efficiency. Bio-based polymers such as nanocellulose and gelatin represent an attractive alternative as porous supporting materials, both from the environmental point of view as they are derived from abundant renewable sources, and also due to their exceptional properties *i.e.*, biodegradability, low cost, versatility of functionalization, and low density. Recently, foams, which are porous materials with open cells and extremely low densities, have been widely investigated for several applications, including heat-insulating materials, supercapacitors, super-absorbents, among others.[9,10]

Another class of porous materials that have been extensively studied are porous carbons. Porous carbon materials have interesting physicochemical properties (*e.g.*, chemical stability, electrical conductivity, high surface area, porosity, sorption capacity) which can be tuned and tailored for specific applications.[11,12] Classical applications in catalysis, gas separation, purification, and catalyst supports have been thoroughly investigated for porous carbons. Due to the good electrical conductivity and rapid electronic response, porous carbon materials have attracted attention in sensing, photochemical applications, and energy storage and conversion. Porous carbons are considered promising electrode materials for batteries, supercapacitors and proton exchange membrane fuel cells (PEMFC) since such materials meet several of the requirements needed for a suitable electrode.[13,14] Electrocatalysts are the core of the fuel cell wherein both oxidation and reduction reactions take place. Carbon can act as the support for catalytic platinum nanoparticles. However, the high cost and risk of depletion of platinum have retarded the massive production of such catalysts. This issue calls for cheaper alternatives, and therefore nitrogen-doped noble metal-free porous carbon catalysts have emerged as promising solutions. Although the development of such catalysts is still under continuous study and several synthesis variables need to be judiciously investigated, they have shown the potential to eventually replace platinum-based catalysts.

1.1 Objective

This project started through an interest in monitoring the formation of the building blocks during the synthesis of zeolites under certain conditions, which later led to the quest to understand the formation of zeolites. Despite of the many discussed mechanisms that intend to describe the growth of zeolites, there is still an incomplete understanding of some of the events during the synthesis process. With this work, we intended to explore an overview of a more plausible explanation, considering a chemical solution equilibrium as the driving force for the growth of colloidal zeolites. Thus, the importance of solution equilibria has been proposed and investigated for colloidal silicalite-1 and ZSM-5 particles in which certain synthesis conditions have been considered.

In addition, a novel synthesis of hierarchically structured porous zeolite was developed by using an evaporation-driven colloidal assembly process. This method offers a new alternative to synthesize hierarchical porous structures with no secondary pore template and at milder and faster synthesis conditions than previously reported procedures, and the potential to be implemented at large-scale production. In another approach for hierarchical porosity, the synthesis of hybrid cellulose-zeolite foams was developed providing high loadings of colloidal zeolite particles. The foams were developed and characterized for applicability to meet the pressing need for materials with large capacity to capture gaseous CO_2.

Recently, noble metal-free ordered mesoporous carbon catalysts for PEMFC have been developed and synthesize using iron-nitrogen doping methods. This project aimed to study the effect of the iron-salt counter anion on the physical and catalytic properties towards oxygen reduction reaction (ORR) by electrochemical evaluation including fuel cell testing. It was also attempted to shed light on the nature of the iron-chelating active site and to understand the differences in the incorporation of high content of Fe species in the catalyst aiming at improving the rate of the ORR reaction.

2. Background: zeolites

Zeolites are crystalline microporous aluminosilicates which consist of interconnected cages and channels formed by SiO_2 and AlO_4 tetrahedra. There exist both natural and synthetic zeolites. Synthetic zeolites outnumber the natural zeolites as a result of the multiple synthetic approaches that have been used to create uniform structures with tunable surface properties. By understanding the mechanism of the synthesis of zeolites, it can provide detailed information to prepare zeolites towards a specific application and foresee their performance in such application.

2.1 Synthesis of Zeolites

The synthesis of zeolites, as we know today, can be traced back to the late 1940s by the work of Richard Barrer and Robert Milton, discovering synthetic chabazite, zeolite A and X, among other types of zeolites.[15–18] However, not until the early 1960s, the introduction of quaternary ammonium cations was studied, which had a high impact on the zeolite synthesis, leading to the discovery of zeolite beta and later on to zeolite ZSM-5.[19–22] Since then, the number of synthetic zeolites has increased, including zeolite-like materials and zeotype materials such as microporous alumino-phosphates and titano-silicates.[23–25] Nevertheless, the understanding of the synthesis process of these materials started in the 1960s, when new zeolites were discovered, advanced modeling approaches and characterization techniques were implemented for the investigation of the mechanisms and evaluation of zeolites. In the 1990s, with the advent of the synthesis of colloidal zeolites from "clear solutions", it became possible to follow the formation of zeolites semi-*in-situ*. The crystal growth could be monitored by various techniques such as electron microscopy (EM), spectroscopy techniques, and dynamic light scattering (DLS), which could follow the nucleation and crystallization stages.[26–32] Most of the studies have been carried out on colloidal silicalite-1 particles due to the simplicity of the synthesis conditions, thermal stability, and ease of following crystal growth.

2.1.1 Hydrothermal Synthesis

Aluminosilicate zeolites are usually synthesized in batch systems under hydrothermal conditions using silicate and aluminate mixtures and subjected to temperatures between 80 and 200 °C for certain periods of time.[33,34] The hydrothermal synthesis is a reaction-crystallization process, which involves at least one liquid phase and both crystalline and amorphous phases. From the experimental perspective, hydrothermal zeolite synthesis can be described as follows: i) the reaction mixture (gel or suspension) containing silica or silica/alumina precursors and alkali or quaternary ammonium cations is prepared at high pH; ii) the mixture is heated, at least

to 80°C, in sealed containers (usually autoclave); iii) after reaching the synthesis temperature, the mixture remains amorphous for some time, after which it starts to transform into zeolite crystals; iv) progressively, the amorphous material crystallizes into a zeolite product, which is finally filtered/centrifuged, washed, and dried.[2] In addition, these synthetic procedures are also strongly dependent on various variables such as temperature, ageing time, agitation, concentration, pH, among others.

Based on observed results, a generalized mechanism has been suggested and broadly discussed, which includes three common stages: induction, nucleation, and crystallization periods and is classically described by an S-shaped crystallization curve shown in Scheme 1.[2,34]

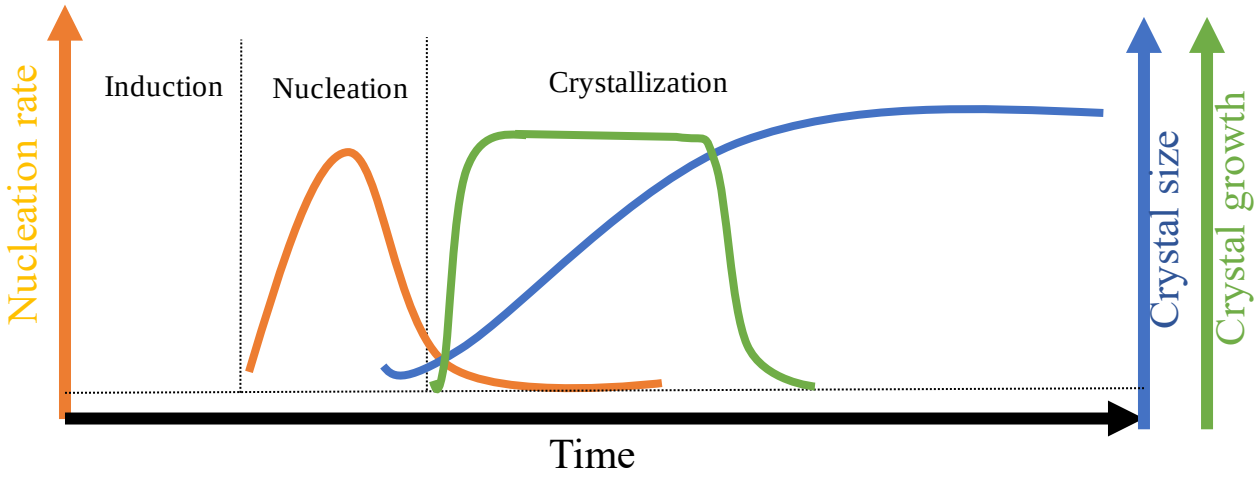

Scheme 1. *Representation of the nucleation, crystal growth rate, and crystal size of zeolites with an S-shaped curve (Taken and modified from reference.[34]).*

The transformation of the amorphous gel phase into zeolite crystals has been studied for many years. In the early 1970s, a transformation through polymerization and depolymerization assisted by an excess of hydroxyl ions was suggested. At the same time, it was proposed that the initial amorphous gel reaches an equilibrium with the liquid phase leading to a release of soluble species into the solution as the crystallization step takes place.[2,35]

The reactants such as silica/alumina precursors and structure-directing agents control the type of zeolite that is formed, and characteristics related to it. After the dissolution of the silica precursor, a first primary amorphous mixture is typically formed, which contains precipitated aluminosilicates or coagulated silica and alumina. This initial mixture, therefore, also affects the nucleation and crystallization behavior. Upon heating the primary mixture, it changes due to equilibration reactions leading to a repartition of components between the solid and liquid phases, which finally yields an intermediate or a "secondary phase mixture".[2,34] This intermediate has been thoroughly studied by nuclear magnetic resonance (NMR) spectroscopy, X-ray diffraction (XRD), electron diffraction, and Fourier-transform infrared (FTIR) spectroscopy showing that this second mixture differs from the initial gel and contains aluminosilicates with a more ordered structure similar to a crystalline zeolite.[36–39]

2.1.1.1 Nucleation

The change in the structural order of the primary mixture into the intermediate mixture or secondary phase mixture takes place due to a selection of particles with a specific critical size and degree of order that will further propagate as a periodic structure as crystallization. This event is called nucleation.

The study of nucleation in zeolites has been mostly focused on amorphous aluminosilicate gels mixtures. Besides, the nucleation of zeolites takes place in a very tiny fraction of the total mass, making it difficult to determine the location of such a fraction from the rest of the gel phase, which has a very similar composition. Thus, different experimental and theoretical studies have been carried out in order to monitor and understand the phenomena at this stage. A reported study investigated the isothermal nucleation rates based on crystal growth rates and particle size distribution.[40,41] This study assumes that, in a batch, the growth rate is the same for all crystals, and therefore the total growth time can be determined. The assumption also considers that the nucleation point for each crystal can be obtained by extrapolation to zero time, leading to a calculation of the nucleation distribution for the entire batch.

Another study reported the synthesis of zeolites at high temperatures in which the correlation between the ageing time and the particle size can provide information about the nucleation stage.[42] This correlation is more evident in the synthesis of colloidal zeolite particles where the ageing time takes place at low temperature, observing that the number of particles increases as the ageing time is prolonged.[43–45] It was also observed that when a two-temperature stage synthesis reaches the same particle size compared to a synthesis run at the initial temperature, the nucleation could be separated from the crystallization stage.

Autocatalytic nucleation was considered by some authors, in which the dormant nuclei are in the amorphous phase and therefore are activated during gel dissolution, as the dissolution rate increases with the growth.[46,47] However, there is no consistent explanation of such an assumption, and hence no model can reproduce the generation of nuclei as a function of the synthesis time. Nikolakis *et al.*[48] suggested another explanation for the release of nuclei, which considers the gel dissolution and nucleation as an interfacial event determined by the boundary between the gel and solution.

From all the experimental evidence and the different formulations of models that try to describe nucleation, it is observed that nucleation during hydrothermal synthesis is strongly influenced by the presence of amorphous components both in the liquid and solid phase wherein most of the cases is considered as a heterogeneous event. This behavior was observed in the synthesis of highly aluminous zeolites and aluminum-free silicalite-1, wherein the first observable crystals were nucleating on amorphous material, indicating the separation from the liquid phase.[40,49]

In summary, the zeolite nucleation process constitutes a sequence of steps from an initial random structure to a pseudo-crystal that can propagate in the growth stage. Thus, the first step is to form a non-homogeneous primary mixture. The second step will equilibrate to form an

intermediate or secondary phase containing small ordered areas or nuclei; a third step will establish a statistical distribution of the ordered nuclei to enable the structure to grow. Finally, the fourth step the crystal begins to grow on the established nuclei. [2,34]

2.1.1.2 Crystal growth

The zeolite growth is the last stage of the synthesis of zeolites, which is the most tangible stage with the appearance of crystals. This stage offers the possibility of monitoring its development by using different characterization techniques. Among the most common techniques used to monitor the crystal growth are particle counters that rely on light scattering and microscopy measurements, which have shown positive results at following the crystal growth.[2] However, it is well known that the products obtained in the synthesis can have different crystal shapes deviating from the spherical shape and can lead to multimodal particle size distributions. In such a case, it is extremely important to make careful analysis and interpretations. Therefore, incorporating other techniques in cooperation, such as optical or electron microscopies, could identify and interpret factors involved during growth of zeolites.

The growth rate is an important parameter that has been associated with understanding the growth of zeolites. The first growth rate determination using scattering techniques was on zeolite A and zeolite X, and later ZSM-5 and the analysis was performed by taking samples during the course of the reaction.[35,50] The first *in-situ* growth study was performed by direct observation of the ZSM-5 reaction mixtures in capillaries using an optical microscope. [51] Later on, modifications were made using special cells and an optical reflection microscope at 170 °C. Also, an interferometric technique was used to monitor the growth of the different faces of silicalite-1 particles.[52,53] The use of these techniques allowed to understand how the zeolite crystals assemble in gels or solution and could elucidate a possible mechanism for the growth process. In addition, some other techniques like atomic force microscopy (AFM) and high-resolution transmission electron microscopy (HRTEM) were also used to provide more details of the growth mechanism.[54]

The observations obtained from these techniques showed lower values of the linear growth rate than the other chemical systems at which the bonding was controlled by electrostatic or Van der Waals interactions (*i.e.*, salts) , evidencing the complexity of the bonding formation in zeolites.[40,55] Further, most of the plots of particle size versus time show a constant linear growth rate with a final tailing-off after the depletion of the building blocks. This behavior in the particle size development, along with the activation energies, have concluded that the growth rate is controlled by surface integration rather than dissolution rate or diffusion from the bulky liquid phase to the crystal.[41,56] This idea was supported later by Schoeman *et al.*, who studied the growth of colloidal silicalte-1 particles and obtained the best linear fitting of the growth rate by using a chronomal analysis that assumed a first-order surface reaction as surface controlled-growth mechanism.[26,57]

For macrocrystals, the linear growth rate has shown strong temperature dependence. Besides, the linear growth rate has been influenced by other synthesis variables at the same temperature

condition. Cundy *et al.* studied the particle growth rates in MFI systems, varying temperature, concentration, aluminum content, among others.[58] At a specific temperature, it was observed that silicalite-1 has the highest growth rate, but the rate was significantly reduced upon the addition of aluminum or ethanol. In a detailed study by Cundy *et al.*, a single synthesis molar composition was studied at 95 °C and other synthesis variations were made including reagents order, ageing time, stirring speed, and other parameters. Although, in all cases, the linear growth rate was maintained, and crystalline silicalite-1 was obtained, changes in the particle size distributions were observed.[40]

Other groups have studied the effect of dilution and pH on the particle growth rate. As in a *in-situ* study of silicalite-1 synthesis at 150 °C, the H_2O/SiO_2 ratio was varied between 75-300, observing a reduction in the growth rate in one of the growing dimensions.[59] Besides, the effect of pH on silicalite-1 at the initial gels, later treated with fluoride at 170 °C, showed an increase in the growth rate when changing the pH from 2.6 to 6.7.[60] However, this trend contradicts what has been observed in colloidal zeolite systems (usually < 100 nm) synthesized from clear solutions.

2.1.1.3 Growth models and formation mechanisms

From the observed results presented above, several authors have attempted to describe the crystal growth. One of these models considers that the growth mechanism occurs by the adsorption of layers controlled by surface nucleation instead of surface dislocations.[61] A simplistic overview of this, states that a building unit is adsorbed on the growing crystal and displaces to a location where the number of points is maximized or has the highest binding energy. After completing a layer, the growth can continue if a monolayer-nuclei is created (see Figure 1).

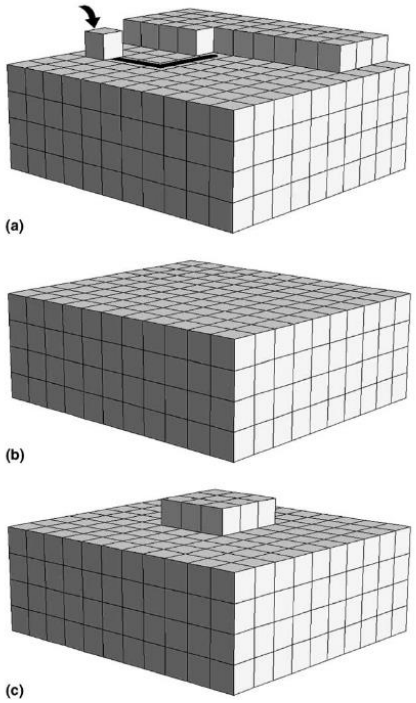

Figure 1. *A layer-by-layer mechanism in zeolite growth. A growth unit is adsorbed onto the growing crystal surface and migrates to a high energy site (a). Completion of a layer (b), further growth takes place only after the creation of island nuclei (c) (Taken from Cundy et al.[2])*

This growth mechanism was evidenced by AFM measurements on zeolite A, where square terraces (nucleation points) along the surface seem to merge, proceeding a progressive formation of elliptical terraces.[62,63] Based on these observations, a model was established and tested, concluding that the growth rate at the kink sites is the highest compared to other surface sites, indicating that the growth layer will proceed at the kink site. In addition, it was found that the surface nucleation rate controls the growth.

Although a macroscopic picture of the growth process was observed and modeled, there are still questions to answer from the molecular perspective. The molecular interactions are acknowledged as the main responsible for such a process. Thus, zeolite crystals are considered to grow in two possible ways: i) adding atoms or molecules (growth units) or ii) aggregation and attachment of preformed nanoparticles. The addition of smaller units has been considered the predominant mechanism for macrocrystals, which includes the growth by adding species at the level of silicate and aluminate anions. Considering that the main bonding in the crystal is T-O-T, where T is either Si or Al, its formation is subject to condensation reactions and hence facilitated by the dynamic polymerization-depolymerization of the aluminosilicate network. The cations play a crucial role in structuring the framework, since they are attached to the surface and interact with the growing units from the solution. This interaction leads to the coordinated water being exchanged by silicate units that assemble in an orderly fashion around the cation. In order to proceed with the growth, another cation must attach to the surface of the growing zeolite so that the propagation can continue.[2]

2.1.1.4 Growth of colloidal zeolite particles

Colloidal silicalite-1 particles were synthesized for the first time in 1994 by Persson *et al.*[26] (now Palmqvist) from "clear solutions" at temperatures lower than 100 °C. As a result, several investigations were conducted to understand the crystal growth mechanism. Many of these investigations were carried out using dynamic light scattering (DLS) measurements. The linear growth rates at this temperature condition exhibited lower values than the gel-based synthesis, making colloidal zeolites suitable for mechanistic growth studies.[64–66]

From all the reported experimental evidence, in the synthesis of zeolites from clear solutions, it was observed the presence of subcolloidal particles of around 3 nm or so-called "nanoslabs" after the hydrolysis of alkoxysilanes in alkylammonium derivates (see Figure 2). This study led to a vast number of papers dedicated to the concept of "nanoslabs".[32,66–70] In this approach, primary amorphous nanoparticles with a diameter of 3-4 nm are formed by condensation-polymerization of silicate anions. These particles aggregate and densify to give amorphous clusters with a size less than 10 nm containing a layer of the structure-directing agent[71,72] that subsequentially aggregate and densify to form crystalline particles at least 50 nm in diameter.[2] However, several authors have deemed the aggregation of "nanoslabs" as an implausible growth mechanism of silicalite-1 since depolymerization or reconstruction of the growth units is necessary to yield an ordered structure.[73–76]

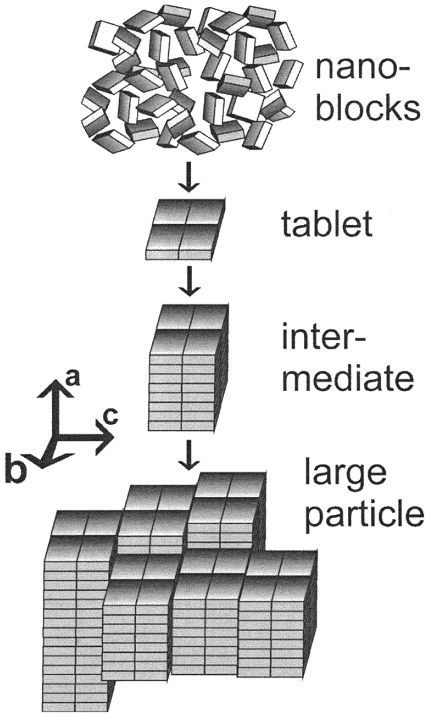

Figure 2. *Schematic representation of the formation of Silicalite-1 material by "nanoslab" mechanism. (Taken from reference[65])*

The molecular growth model instead includes successive additions of cations (TPA+ or small cationic TPA-silicate complexes) and negative silicate monomers at the growing zeolite surface.[2,77] Equilibration between the growing zeolite and the dissolved species in the solution

is continuously re-established during the zeolite growth. In favor of the molecular growth model, it is well known that there is a fundamental equilibration mechanism of Si-O-Si bond making and bond breaking at the surface of silica and silicates, based on condensation and dissolution reactions catalyzed by hydroxyl ions.[78] As the zeolite growth process gradually depletes the growth units in solution, it will reach a point (at high pH conditions) where this equilibration results in the rate of dissolution being equal to the rate of condensation. At this point, the zeolite growth seems to stop suddenly and is why the yield typically does not reach 100% conversion to zeolite. In this thesis, we present the influence of a condensation-dissolution dynamic equilibrium on the zeolite growth and further explain the premature termination of zeolite growth and provide a route to achieve full conversion. In addition, we also find information about the nucleation stage during the zeolite synthesis based on studies of the dynamic equilibria solution reactions. These will be discussed later in Chapter 5 and in more detail in Paper 1 and Paper 2.

2.2 Applications of Zeolites

Zeolite properties usually depend on the zeolite framework and chemical composition. Zeolite frameworks can be classified according to the size of the pore opening ring size, which corresponds to the pore windows: small pore (≤8-ring), medium pore (10-ring), large and extra-large pores (≥12-ring). Zeolite frameworks obtain a negative charge for each aluminum atom, and such charges can be compensated by exchangeable extra-framework cations offering versatility. The additional species in the pores of zeolites can be removed, leaving space for a sieving effect of guest molecules based on their size, polarity, and shape.[4] The coupling between the zeolite pores and the catalytically active sites located inside enables the feature of shape-selective catalysis towards the formation of products. Zeolites can also encapsulate and stabilize metal agglomerates or nanoparticles, leading to host-guest composite materials with outstanding properties. All these characteristics along with the low manufacturing costs make zeolites suitable for industrial chemical applications in catalysis, adsorbents for water and gas purification, and ion exchangers.[79]

Zeolites have been commonly used as catalysts in oil-refining and petrochemical processes like gasoline production via catalytic cracking.[80] Recently, other applications in renewable energy and environment such as exhaust gas catalysis, oxidation of hydrocarbons, and CO_2 capture, among others, have given zeolites a lot of interest. Colloidal zeolite particles have shown positive results in the traditional applications and have also emerged as an alternative for new applications, such as membranes, sensing and electronics platforms, drug delivery, cosmetics and food, medical applications, and in preparation of hierarchically porous materials.[79,81] In this thesis, we present two studies in which colloidal silicalite-1 particles are used to prepare spherical hierarchically structured zeolites and hybrid zeolite materials for applications in CO_2 capture and are described in more detail in Paper 3 and Paper 4.

2.2.1 Hierarchically structured zeolites

Zeolites have microporous ordered structures with larger surface areas, high adsorption capabilities, thermal and hydrothermal stabilities, among other advantageous characteristics. Zeolites have been widely used as heterogeneous catalysts in many industrial applications especially petrochemistry and oil refining. However, an important observation considers that intracrystalline diffusion in small micropores, limits the performance of zeolites in catalysis and adsorption processes.[82–84] Limitations in diffusion not only reduces the catalytic activity but also reduces the selectivity and durability of the catalyst.[7] Some of these limitations, especially diffusion, can be overcome with either zeolites holding ultra-large pore sizes or using colloidal zeolites.[85,86] Reduction in the particle size have shown improved volumetric diffusion rate into and out from the zeolite and thereby enhanced catalytic conversion rate. Also, the reduction of zeolite particle size increases the outer specific surface area of the material, which for reactions involving bulky molecules may be favorable.[81]

A desirable strategy to tackle diffusion limitations is incorporating either meso- or macropores in zeolite materials which lead to a hierarchical porous structure. This strategy has attracted a lot of interest, since the combination of properties from both types of porosities could potentially enhance the mass transport of reagents and products in and out from the active catalytic site.[82] In the last two decades, several researchers have focused on developing strategies to form hierarchical porous zeolites. The synthesis protocols can be divided into three different categories of materials: micro-meso-macroporous zeolites, micro-macroporous zeolites, and macro-mesoporous zeolites. From the perspective of the catalytic application, a micro-mesoporous material with high catalytic activity is preferable, since mesopores have a desired pore size domain for improved mass transport.[106,109] Although various micro-mesoporous zeolites synthesis approaches have been successfully developed, the optimization of interconnectivity between the different pores and the importance of simple and scalable methods, still represent major challenges.

Micro-mesoporous zeolite structures have been mostly prepared by three different approaches: post-treatments, solid templates, and soft templates.[82] The post-treatment approaches involve the dealumination of zeolites via acid leaching and desilication and have been widely employed at the industrial scale.[82] Unfortunately, these strategies yield a reduction in crystallinity and leave amorphous residues, which interfere with the catalytic process and reduce the catalytic activity. Carbon has been used as a solid template in different forms to generate mesoporous zeolites. For example, nanosized carbon particles which were encapsulated in growing zeolite microparticles (*i.e.*, ZSM-5, MEL, TS-1) and after calcination, formed cave-like mesopores.[87–89] However, this strategy limits the accessibility and mass transfer in the catalytic process of molecules larger than the micropore diameter. Although the use of ordered mesoporous carbons such as CMK-3 was investigated, disordered mesopores were obtained, forming in some cases, cave-like mesopores. This result shows that it is still difficult to replicate the mesopores from the carbon template. On the other hand, carbon aerogels have shown better results due to the large mesopores and thicker walls, leading to a monolithic morphology.[86,90] Other organic aerogels were used as templates, as was the case of urea and formaldehyde when polymerized

with the presence of nano-zeolite solution, forming uniform microspheres with an adjustable secondary pore architecture. [91,92]

In the soft templating approach, an organic surfactant is usually employed, which is in direct contact with the silica species during the crystallization process[82,93,94]. Thus, the surfactant is highly critical, since its stability, morphology, and interaction with the silica species dictate the mesopore formation. Several examples of surfactants have been used in the preparation of zeolites. Hydrophilic cationic polymers tend to strongly interact with silica species, and the high-temperature stability makes them suitable for the synthesis of the micro-mesoporous structured materials. Polydiallyldimethylammonium chloride (PDADMAC) has been used as a template in crystals of zeolite beta, ZSM-5, and FAU, exhibiting a disordered mesopore size distribution.[95–97] Amphiphilic organosilanes have also been used in the formation of mesoporous MFI zeolite, and other types of aluminosilicate zeolites since the positive charge interacts with the silica species and the long-chain contributes to the mesopores formation.[98–100]

Although many researchers have successfully synthesized micro-mesoporous zeolites by the aforementioned templating strategies, they have not generated large mesoporous due to the high crystallization temperatures of zeolites. In addition, these approaches are expensive, quite limited in template sizes, and sometimes lack of crystallization of the alumina tetrahedrons within the zeolites, which are critical to ensure catalytic activity.

The indirect templating has been a less investigated set of synthesis to prepare mesoporous zeolites, but it can solve some of the mentioned limitations of the above strategies.[93,101] Indirect templating routes for the synthesis of hierarchical structure zeolites are mainly characterized for not using any template, and thus it is a more cost-friendly alternative. Indirect templating involves the transformation of another templated material into a hierarchically structured zeolite material or by controlled deposition of zeolite crystals onto a templated material. Only few indirect templating strategies have been reported like steam-assisted crystallization (SAC), solid-phase crystallization, and nanofusion.

For example, to synthesize hierarchical mesoporous zeolite beta, the SAC method has been used in mixtures with concentrated gel precursors and structure-directing agent tetraethylammonium hydroxide (TEAOH). This method yielded a large mesopore size up to 60 nm and pore volumes of 0.9 ml/g.[102,103] The ultra-small beta particle-assembly causes the mesoporosity, and its growth continues by dense packing of the gel, and upon SAC, the nanoparticles condense into porous networks.

Quasi-solid-state methods are similar to the SAC used to prepare micro-, meso-, and macroporous titanium silicalite-1 (TS-1).[104] In this method, a mixture of dry-gel precursors combined with TPAOH and TEOS were mixed with glycerol and then was hydrothermally aged. The gradual transformation from the amorphous precursor to the crystalline TS-1 retained the hierarchical structure due to the quasi-solid-state system that contains glycerol, which enables the reaction to proceed slowly, avoiding the collapse of the porous structure.

Nanofusion is a strategy similar to the quasi-solid-state approach which uses concentrated precursor gels impregnated with TEAOH and are subject to hydrothermal conversion, yielding instantly 20-40 nm fused nanoparticles forming compacted aggregates that are separated by filtration[105]. Nanofusion shows high conversion and is more economically viable to produce mesoporous zeolites with tuned mesopores from 15 to 35 nm as a result of reaction time.

All these methods have successfully incorporated, at least, the second degree of porosity without using secondary templates or sacrificial template. Also, these synthetic approaches have enlarged the pore size and, in some cases, increased the surface areas and pore volume. However, these methods still use high crystallization temperatures, long preparation times (*e.g.*, ageing and/or reaction times), low yield, and non-defined morphologies of the products. In this thesis, a novel synthesis method for preparing mesoporous zeolites with the absence of mesopore template, and shorter preparation times and milder temperatures has been developed and more details are presented in Chapter 6 and Paper 3.

2.2.2 CO_2 capture in zeolites

The combustion of fossil fuels has led to a release of approximately 32 Gt of CO_2 annually, generating a dramatic climate change.[106] Most of the CO_2 emissions are generated from industrial thermal power stations, refineries, cement- and steel production. Several strategies have been proposed and investigated to tackle this global environmental issue and minimize the emissions, such as optimization of energy efficiency, clean coal technologies, afforestation and reforestation, and the use of renewable energies, among others. One very promising approach to minimize the CO_2 release from the above sources is Carbon Capture and Storage (CCS). CCS has been considered a technology that can potentially reduce the amount of CO_2 emissions up to 90%.[107] One of the advantages of this approach is that it could eventually be implemented at existing energy infrastructures.[108] The basic concept of CCS is to sequestrate and compress CO_2 generated from large source points, transport and deposit underground the crust of the earth or in empty oil-reservoirs.[107–109] However, the capture step seems to represent the most expensive part of the entire process, and its cost must be reduced in order to be implemented in the current energy system. One of the most common materials used for the capture process are "liquid" amines such as alkanolamines.[108,110] These amines are highly corrosive and must be appropriately diluted, leading to large solution volumes and large thermal losses upon heating and cooling off the solvent. This issue has led to the quest of finding new alternatives, as in the case of solid sorbents. Various porous solid materials have been suggested as potential candidates, such as activated carbons, metal oxides, metal-organic framework (MOFs), and mesoporous silica. Among these materials, zeolites appear to represent an alternative due to their sieving and adsorption characteristics along with low-cost industrial production.

Zeolites have been considered one of the best inorganic solid sorbents for CO_2 capture due to strong electric fields in the framework and its interaction with molecules with dipole or quadrupole moments as is the case of CO_2 molecule. The mechanism of CO_2 adsorption on zeolites shows that the physisorption of the gas molecule occurs as a result of a linear orientation by an ion-to-dipole interaction between the zeolite and CO_2 molecules.[111] In addition, zeolites

have structures and active sites which make them highly shape- and size-selective and suitable for capturing CO_2. Several types of zeolites have been considered as promising candidates for CO_2 capture, below some of them will be briefly discussed.

Zeolite A is one of the most investigated zeolites for gas separation and CO_2 capture. It has a Si/Al molar ratio of around 1 and also has large cages and narrow pore windows of 8-membered rings that are comparable, in size, with the kinetic diameters of N_2 and CO_2.[108,112] The pore window of zeolite A can be adjusted by changing its counterion (*e.g.*, K^+, Na^+, Ca^{+2}) leading to zeolite 3A, 4A, and 5A, respectively. The number denotes the size of the pore window opening (*i.e.*, 3Å, 4Å, 5Å). Zeolite A has high electrical gradients, which might influence the high CO_2 uptake capacity. In one of the first studies, zeolite NaA exhibited a capacity to adsorb 4 mmol CO_2/g at 273K and 101 kPa.[113] Also, when the Na^+/K^+ ratio was varied in zeolite NaKA, it strongly influenced the adsorption capacity and CO_2-over-N_2 selectivity, showing an enhanced selectivity and rapid uptake in comparison to zeolite NaA.[114–116] Another study investigated zeolite A with higher Si/Al ratios (≤5) and observed that the most increased uptake was a ratio of two and lower for ratio one and ratio five.[117] Further, it was observed that zeolite A regenerates much more as the silica content increases due to the reduction of isosteric heat of CO_2 adsorption.

Zeolite NaX is another type of zeolite that has been extensively studied for CO_2 capture.[108,118] It has cages interconnected by 12-membered ring openings and a Si/Al molar ratio of approximately 1, and sodium cations balance the charge. The adsorption of CO_2 in this zeolite occurs via equilibrium mechanisms where CO_2 is mostly physisorbed, and a tiny amount of the gas is chemisorbed.[108] Zeolite NaX has shown to have higher uptake capacity than zeolite A obtaining a CO_2 uptake of 5.5 mmol/g, whereas their zeolite A reached 3.5 mmol/g.[119] In addition, it has also shown high uptake at low pressures than in activated carbon which has a much higher surface area.[120] However, the uptake of CO_2 on zeolite NaX can be strongly reduced when water is present in the gas mixture due to the high hydrophilicity of the zeolite. This observation was found in a study that investigated the effect of water in the gas mixture, showing a reduction from 3 mmol/g at 0.1 bar to 1.2 mmol/g. [121,122] Water molecules tend to adsorb strongly to the cations, reducing the electrical field gradients within zeolite, and therefore CO_2 cannot adsorb on it. The use of more hydrophobic zeolite NaX or to regulate the adsorption of CO_2 over water could be one of the alternatives to mitigate this problem.[121,122]

Zeolite Y has a very similar framework to zeolite X but has a slightly higher Si/Al molar ratio of 2-3 and a lower number of cations, making zeolite Y less hydrophilic.[108] Zeolite Y has also been investigated as an adsorbent for CO_2 capture, involving temperature and pressure variations and exchange in the cation from sodium to barium and lanthanide.[123,124] The latter showed that LaY and BaY have weaker chemisorption than NaY. Further studies on ion-exchanged zeolite Y were developed; one investigated the effect of the strong interaction of the CO_2 on the cations and oxygens within the framework of zeolite CsY and KY at low pressures.[125] Other reported ion-exchanged zeolite NaY with cations of copper (II), calcium, nickel (II), and chromium (III), and observed a significant reduction of the CO_2 uptake.[126]

Zeolites are preferred to be more hydrophobic for CO_2 capture applications since most of the flue gases contain significant amounts of water that strongly interferes with the CO_2 adsorption process. Zeolites with a high Si/Al molar ratio tend to be more hydrophobic. Zeolite beta has shown higher hydrophobicity due to the large Si/Al molar ratio (*i.e.*, 8). Ion-exchanged zeolite beta with potassium ions showed the best performance over other type of cations (*i.e.*, Na^+, Li^+, Ba^{2+}, Ca^{2+}, Mg^{2+}), having a CO_2 uptake of approximately 3 mmol/g at 298 K and 1 bar and selectivity over nitrogen between 17-28.5.[127] Changes in the charge compensating cation (H^+ by Na^+) and in the Si/Al molar ratio resulted in differences in the CO_2 uptake and selectivity.[128] Moreover, synthesis methods play a significant role in the adsorption of CO_2; that was the case for zeolite beta synthesized in microwave conditions, exhibiting an enhanced CO_2 uptake of 2.16 mmol/g, compared to 1.94 mmol/g for zeolite beta prepared under conventional hydrothermal synthesis. This improvement was attributed to the higher incorporation of aluminum content and more hydrophobic synthesis.[129]

Zeolites can also be prepared as CO_2-selective permeance membranes for CO_2 capture, as is the case of MFI-type zeolites that are highly siliceous zeolites, increasing the hydrophilicity and offering the possibility to have a better separation of CO_2 from flue gases in humid conditions. Various zeolite MFI membranes were reported exhibiting uniform thickness and preferable permeation for CO_2. One study prepared high silica ZSM-5 membranes, exhibiting an interesting preference for CO_2 gas, which flows through faster than helium and hydrogen gases. Moreover, it had a CO_2/air separation factor of 3 and permeance of 5 x 10^{-7} mol/m^2s Pa.[130] Surface-modified ZSM-5 zeolite membranes exhibited a CO_2/N_2 separation factor of approximately 15 at 373 K at feed pressure 400 kPa and permeance of 3.6 x 10^{-8} mol/m^2s Pa. Moreover, it was explained that the permeation of CO_2 is governed by adsorption and diffusion through the zeolite micropores.[131] Zeolite MFI membranes have also been investigated upon variation of the Si/Al and the effect on the permeance and selectivity towards CO_2. A study prepared ZSM-5 membranes with three different Si/Al molar ratios (*i.e.*, 152, 47, 26) supported on alumina discs to separate CO_2 and methane.[132] The permeances for CO_2 were 1.42 x 10^{-5}, 9.8 x 10^{-6}, and 7.1 x 10^{-6} mol/m^2s Pa and CO_2/CH_4 separation factors of 1.4, 2, and 3.1, respectively, at 298 K and feed pressure of 700 kPa.

Various investigations have studied silicalite-1 membranes as potential CO_2-sorbent membranes due to the suitable channel window size and high thermal stability.[133] Several silicalite-1 membranes were reported studying single or binary mixtures of CH_4 and CO_2.[134–137] It was observed that defect-free membranes are more favorable for CO_2 permeation and selectivity over methane, showing a higher adsorption affinity of the zeolite to CO_2. A silicalite-1 membrane was reported with the straight channels uniformly aligned and studied for the separation of CO_2 and hydrogen.[138]It exhibited permeance for CO_2 of approximately 5.0 x 10^{-6} mol/m^2s Pa and a CO_2/H_2 ratio of 31 and CO_2/CO ratio of 15 at 273 K and feed pressure of 9 bar.

In Chapter 6 and in Paper 4, a new hybrid zeolite bio-based foam is presented and discussed. In these foams colloidal silicalite-1 particles are utilized as a model to determine the potential of using bio-based foams as supporting materials. This was done in order to replace the classical

binders used to process zeolite materials which prevent them to exploit the maximum capacity in catalysis and separation applications.

3. Background: Ordered Mesoporous Carbons

Porous carbon materials have attracted considerable attention due to their outstanding properties, including large surface area, high pore volume, good thermal and mechanical stabilities, electric conductivity, low density, high abundance of precursors, and easy processing.[11,12,139] Therefore, many applications have utilized porous carbons, such as gas separation, water purification, catalyst supports, gas storage hosts, and electrodes for energy storage and conversion. From a mass transport perspective, mesoporous carbons are especially attractive. Their pore size span (2-50 nm) enables access to a larger number of molecules, and their specific surface area does not reduce significantly compared to microporous carbons. Many efforts have been devoted to synthesize mesoporous carbon using a variety of preparation methods such as chemical or physical activation or combination of both;[140,141] catalytic activations of carbon precursors with organometallic compounds;[142,143]carbonization of thermosetting or a pyrolyzable component;[144,145] and carbonization of aerogels under supercritical drying conditions.[146–148] However, all these methods lead to broad pore-size distributions with non-uniform porous structure.[149] This disorder might affect the performance in many of the energy applications. Ordered mesoporous carbons (OMC) is a class of mesoporous carbons in which the pore size distributions are narrower, and the pores are ordered on the mesoscopic scale. This class of porous carbons has emerged to overcome the mass transport issues existing in classical ordered microporous materials (*i.e.*, zeolites, MOFs), holding similar surface areas or larger. Also, the search for OMCs have motivated development of new synthesis strategies.

3.1 Synthesis of ordered mesoporous carbons (OMC)

In the last 20 years, the synthesis of OMCs has been growing rapidly.[150] The focus of the different reported studies has been the use of templates to form ordered porous structures. These studies have been mainly divided into hard-templating and soft-templating approaches. Based on these, different synthesis parameters have been studied, including formation mechanism and synthesis variables such as carbon precursors, type of block copolymer and mesoporous silica templates, temperature and environment conditions, among others.

3.1.1 Hard-templating synthesis

The first reported hard-templated porous carbon was conducted by Knox *et al.* using silica gel as a template.[151] Although many other methods have emerged further, later on, the main

principle behind this synthesis approach is still applicable: i) preparation of the hard template with ordered structure (silica gel, mesoporous silica), ii) infiltration or impregnation of the template with the carbon precursors, iii) polymerization and/or carbonization of the precursors and iv) dissolution or etching of the template (see Figure 3). The space occupied by the template is transferred to the carbon structure, forming a continuous carbon framework. A long time passed until the first ordered mesoporous carbon was reported in 1999 by Ryoo *et al.* using the MCM-48 silica as a template.[152] In this method, the MCM-48 was impregnated with a sucrose solution and sulfuric acid and subject to temperatures up to 1100 °C. The silica framework was etched with HF or an ethanolic NaOH solution. The average mesopore size was around 3 nm, with a cubic structure and the crystallographic space group $I4_1Ia$.

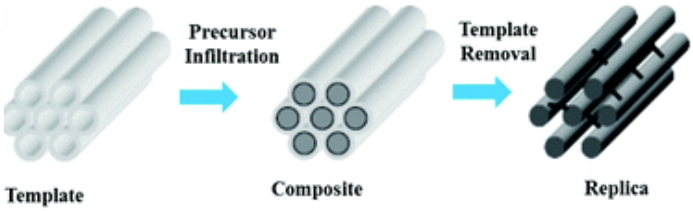

***Figure 3**. Schematic representation of a hard-templating approach to preparing OMCs. (Taken from reference.[153])*

Since then, several silica templates have been used, including MCM, SBA, FDU series, to synthesize OMCs. With these templates, cubic (*e.g.*, FCC, BCC) and hexagonal structures have been obtained with an average pore size range between 2 and 12 nm.[139,154] During the polymerization and subsequent pyrolysis, the chemical structure of the precursor will determine the shrinkage of the framework leading to micropore formation, which has a large impact on the surface area and morphology. Many precursors have been implemented including, low molecular-weight molecules such as sugar, sucrose, furfuryl alcohol, and dense structures as pyrene, polyacrylonitrile, acenaphthene, among others.[12,139] Low-molecular precursors lead to a framework shrinkage, thus increasing the pore size and surface area, and generating some microporosity in the structure. On the other hand, the dense structures replicate the porous structure with a minimal shrinkage of the framework, and therefore no microporosity is formed.[12,139,154]

The advantages of using silica templates are: a facile replication of the highly ordered porous structure, the use of hard templates ensures that the structure is better maintained during pyrolysis and it is a feasible approach to large-scale production. One big drawback is that removing the template is time-consuming, and the use of acid or base treatments is not an easy step in terms of safe handling of such chemicals.

Overall, the experimental protocol of hard templating to synthesize mesoporous carbons employing mesoporous silica is a time-consuming process since many steps are needed so that a mesoporous carbon structure is produced. Especially the time required to prepare and to remove the template. Thus, many efforts have been cast on developing much more facile synthetic methods.

3.1.2 Soft-templating synthesis

The direct preparation of OMCs by self-assembly of surfactants or block copolymers and the carbon precursor has been investigated by many authors.[155,156] The main advantage of this method is that no template must be removed after the pyrolysis step. During the preparation by soft-templating, the interaction between the surfactant and the carbon precursor occurs by hydrogen bonding, which leads to polymerization of the precursor, which afterwards is pyrolyzed to form the mesoporous structure. Reported soft-templated OMCs have shown average pore sizes between 3-7 nm with different morphologies, including spheres, monoliths, films, among others.[157–159] One of the most investigated soft-templating procedure is the evaporation-induced self-assembly (EISA). In the EISA, the ordered structure formation takes place on the surface where the solvent evaporates, thus producing the OMC films. By this soft-templating approach, different ordered porous structures (*e.g.*, hexagonal, lamellar, bicontinuous, BCC) have been easily prepared by only changing the mass ratio between the carbon precursor (*i.e.*, resol) and the surfactant.

The main limitations in soft-templating procedures are related to the availability of block copolymers and the carbon precursor, since the interaction between the precursor and the block copolymer is quite limited. The most investigated carbon precursors have been resol and resorcinol-formaldehyde systems. As block copolymers polystyrene-*b*-poly(4-vinylpiridine) (PS-P4VP) and poly(ethylene oxide)-*b*-poly(propylene oxide)-*b*-poly(ethylene oxide) (PEO-PPO-PEO) are the most commonly used.[139,154] In addition, as a result of the soft-templating, the OMCs are more challenging to graphitize than in hard-templating approaches.

3.1.3 N-doped OMC synthesis

The type of templating approach and chemical nature of the precursor are crucial to tune and tailor some of the properties of the OMCs, including pore size, specific surface area, pore volume, chemical, and thermal stabilities. The incorporation of heteroatoms (*e.g.*, O, N, S, B, P) or doping has improved the electronic properties and enhanced catalytic or sensing performance.[160] These new mesoporous carbons have led to the development of electrodes for energy and conversion applications, specifically supercapacitors and fuel cells.

Doping is the replacement of some carbon atoms in the structure with heteroatoms that significantly modify the electrical and electronic properties of the material. Doping of OMCs can occur by two different methods: *in-situ* incorporation during the synthesis or surface functionalization. The latter only modifies the surface properties, and most of the cases do not change the bulk properties, whereas *in-situ* incorporation can distribute the heteroatoms more homogeneously within the carbon framework. Also, the availability of nitrogen-carbon precursors is high, leading to great a variety of possibilities to prepare N-doped OMCs.

Nitrogen-doped carbons (NCs) have been shown to improve the capacitive properties of porous carbons.[161,162] Thus, N-doped carbons have become the most studied heteroatom doped carbon

for electrode materials over the last decade.[163] In the preparation of N-doped OMCs, hard- and soft templating approaches still apply.

As described previously, silica templates have been the most used template for hard-templating approaches. Various studies have used SBA-15 as a hard template in combination with several nitrogen-containing precursors such as gelatin,[164] dicyandiamides,[165] dopamine,[166] pyrrole, aniline and phenanthroline,[167] urea,[168] aminoacids,[169] among many more. These procedures led to N-doped OMCs with tuned properties, including specific surface areas (700-2000 m^2/g), pore volume (0.9-2.5 ml/g), average pore size (2-10 nm) and nitrogen-doping content (0.5-11 wt-%).[160] Other studies have used other types of silica templates such as porous spheres and KIT-6.

On the other hand, nitrogen-doped OMCs prepared by soft-templating procedures have presented low thermal stability and nitrogen-doping content due to the decomposition of the nitrogen precursor in the presence of high oxygen-content surfactants. Also, the high pyrolysis temperatures can have a strong impact on the nitrogen-precursor decomposition.[163] As mentioned in the previous section, the soft-templating method lacks template availability, and this narrows the available nitrogen sources, limiting the number of studies using this method.

The reported studies in N-doped OMCs synthesized by soft-templating approach have used Pluronic™ block copolymers as the main surfactants and various nitrogen sources, including dicyandiamide,[170] hexamethylene-tetramine,[171] melamine,[172] ammonia.[173] Some of these approaches managed to incorporate nitrogen-doping content higher than 10% (*e.g.*, 13.1 wt-%), but their surface areas were comparably low (*e.g.*, 600 m^2/g).

3.2 Applications of ordered mesoporous carbon in fuel cells

Due to the large surface areas, ordered porous structures, and the availability of functional groups, OMCs have been investigated in environmental applications (*e.g.*, separation of gases, removal of heavy metals, desalination), electrode materials (*e.g.*, supercapacitors, batteries, sensors) and catalyst and catalyst supports, *e.g.* in fuel cell applications.

Fuel cells are electrochemical devices that can convert chemical energy into electrical energy through electrochemical reactions. One of the most common and studied fuel cells is the proton exchange membrane fuel cell (PEMFC), where oxygen and hydrogen react to form water. The reactions are divided into two half-cell reactions. At the anode, the hydrogen oxidation reaction (HOR) takes place, whereas at the cathode the oxygen reduction reaction (ORR) occurs. Without catalysts, the overall reaction is a very slow process, and therefore catalysts are needed to overcome the energetic barriers and increase the reaction rate. Platinum alloys have been the most efficient and commonly used catalysts for both HOR and ORR, and carbon materials have been used to support them.

OMCs have also been used to support platinum nanoparticles, showing better capabilities than those of similar carbon materials due to the formation of small uniform nanoparticles over the mesopores, and better distribution of the nanoparticles over the carbon framework.[174,175] Similar

results have been observed on platinum-based catalysts and other precious metals (*e.g.*, palladium).[176,177] However, the scarcity and cost of platinum are the main reasons against platinum-based catalysts in commercial fuel cells. Therefore, new strategies to prepare non-platinum electrocatalyst have been investigated, especially for the ORR, which needs large amounts of platinum catalyst so that the efficiency reaches sufficient values.

Heteroatom doping of carbons is one studied approach that has shown high metal-free catalytic activity for ORR.[178] Several N-doped carbons have been developed, such as carbon nanotubes, carbon nanofibers, graphite, graphene, and mesoporous carbon.[179,180] The good catalytic activity is attributed to their unique electronic properties due to the conjugation between the electron pair of the nitrogen and the graphene π system.[181] However, very few N-doped mesoporous carbons have shown stability in acidic conditions where PEMFCs are preferably used.[182]

N-doped OMCs have also been used to prepare transition metal and N-doped OMCs. One of the first N-doped OMC was prepared by first preparing an N-doped OMC (CN_x) using polyacrylonitrile (PAN) as a nitrogen precursor and SBA-12 as the hard template.[183] After formation of the N-doped OMC, it was pyrolyzed together with iron acetate at 1000 °C to form Fe-N-doped OMC. This catalyst exhibited better performance towards ORR than the pristine N-doped OMC. Likewise, other Fe-N-doped OMC material was synthesized by preparing N-doped OMC with the different mesoporous silica SBA-12, SBA-15, and SBA-16, and polyaniline as templates and nitrogen precursor, respectively.[184] Subsequently, it was pyrolyzed with $FeCl_3$. The resultant Fe-N-doped OMC exhibited better ORR activity than their pristine N-doped OMC and it was also found that Fe-N-doped OMC prepared from SBA-15 was the most effective catalyst due to the mesopore size of 4.3 nm.

A new class of transition-metal N-doped OMC was reported by Dombrovskis *et al.*[185] Fe- and Co-N-doped OMCs were prepared by a one-step synthesis, conducting a nano-casting process using KIT-6 cubic mesoporous silica with furfurylamine and the transition-metal salts as carbon-nitrogen precursor, and transition-metal source, respectively. This process was done with the intention of simultaneously prepare ordered mesoporous carbon and generate transition-metal nitrogen chelating active sites. As expected, the catalytic activity towards ORR was enhanced by the presence of the transition-metals sites compared to OMC and N-doped OMC materials. Further, it was found that the catalytic activity towards ORR, was superior for Fe-N-doped OMC in comparison with Co-N-doped OMC that showed degradation effects at high temperatures (*i.e.* 80 °C).

Based on this synthetic strategy, further studies followed, wherein the effect of synthetic variables including the degree of hydration of the iron salt, molar ratio of iron salt/C-N-precursor, combination of carbon-nitrogen, and aging time of precursors were investigated.[186–188] It was found that using a sodium hydroxide-based etching method to remove the silica template in Fe-N-doped OMC materials, has a positive effect in the catalytic performance of the materials, in comparison with the traditional HF-etching methods. This effect can be explained by the increase in the carbon mesopore diameter and possibly the improvement in the conductivity when using sodium hydroxide. Besides, the hydration of the iron chloride salt

exhibited an improvement in the structural properties including the specific surface area, pore volume and meso-order, and in the catalytic activity. This result is based on the reactivity of the irons salts towards the precursor polymerization. In case of the hydrated iron salt, it shows that the precursors polymerization has a slower reaction compared to a more violent and exothermic polymerization reaction using anhydrous iron salt.

High iron content, given by the high molar ratio of the iron salt and precursor, seems to impact the catalytic activity but results in large ohmic losses and limited mass transport properties at high current density region. Besides, the ageing effect of mixtures between iron salts and the precursor exhibited a positive impact on the catalytic performance, showing a significant improvement from freshly prepared solution to 24 h ageing time, but then little improvement up to 7 days.

In Chapter 7, a study of varying the iron salt counter anion is presented in order to investigate whether the change in the anion could induce more iron incorporation during the synthesis of Fe-N-doped OMC materials and thereby improving the catalytic activity.

4. Experimental methods for porous materials

4.1 Dynamic light scattering (DLS)

DLS is a particle size analysis method based on the hydrodynamic particle mobility that has been used for the characterization of sub-micron particles and some macromolecules.[189,190] The principle is a time-resolved measurement of the scattered light after the interaction with matter in a solvent. Due to the Brownian motion of the particles in the solvent, the scattered light intensity oscillates around an average value[191]. These fluctuations provide information about the translational diffusion of the particles based on a correlation function that can describe how long the particle remains in the same spot over a specific time. This correlation function can be used to determine the size or the hydrodynamic diameter of the particle from its diffusion constant, *D*, using the Stokes-Einstein equation:

$$D = \frac{k_B T}{6\pi\eta r_H}$$

Where k_B is the Boltzmann constant, T is the absolute temperature of the colloidal sol, η the viscosity of the solvent, and r_H is the hydrodynamic radius of the particle.

However, the data interpretation has to be carefully analyzed since the particle size is determined for dilute suspensions and assumes spherical particles.[192] Thus, limitations regarding shape and concentration are present.

The first use of DLS for semi *in-situ* monitoring of the formation of colloidal zeolite crystals from clear solutions was done by Schoeman and Persson *et al.*[26,64] These studies could be conducted and provide relevant information about zeolite formation due to the nature of the colloidal zeolites at synthesis temperature (< 100 °C) since they have a size less than 100 nm and their shape is practically spherical. It was also observed that the linear growth rate was much lower than those reported earlier for gel-based zeolite synthesis. The positive findings allowed DLS to be an important characterization technique for mechanistic growth studies.

In this thesis, DLS is used to determine particle size evolution over the reaction time and analysis after further reaction treatments in Chapter 5. The DLS instrument used was a Zetasizer Nano ZS from Malvern. Dilution of the samples was needed for better results. The algorithm used for fitting the correlation function is the non-negatively least squares (NNLS), thus calculating the diffusion coefficient and the hydrodynamic radius using the above equation.[189,190]

4.2 X-ray diffraction (XRD)

X-ray diffraction is one of the most common spectroscopy methods for identifying and characterizing the structure of crystalline materials.[193] In short, a collimated beam is irradiated onto the crystal, and a part of the X-rays will be diffracted at certain angles. The crystals have periodic arrays of atom planes that allow the X-rays to diffract as the wavelength is in the range of interplanar distances. Coherent diffraction is expected for crystals and occurs in accordance with the requirements of Bragg´s Law:

$$2d \sin\theta = n\lambda$$

Where d is the spacing between crystallographic planes of atoms, θ is the angle between the incident X-ray and the plane of atoms, n is an integer representing the diffraction integer, and λ is the wavelength.

The most common wavelength in XRD experiments is λ=1.5418 Å, corresponding to the Cu Kα radiation. The diffracted angles can be scanned, and the intensity of the radiation can be measured. A diffraction pattern is obtained from these scans that can be used to identify the unit cell parameters and atomic positions within the lattice. Using structural refinement methods crystallites sizes, sample concentration, and defect or impurity concentrations can be calculated.

Herein, XRD measurements were conducted to identify and confirm the MFI pattern of the synthesized colloidal zeolite particles in Chapter 5 and similarly in the mesoporous zeolite microspheres in Chapter 6. In addition, the Fe/N-doped carbons were also evaluated by XRD in order to study the effect of the anion on the graphitization of the mesoporous carbons in Chapter 7. The measurements were carried out on purified calcined zeolite powders in a Siemens D-5000 X-ray diffractometer using a Cu Kα radiation.

4.3 Scanning electron microscopy (SEM)

Scanning electron microscopy is a standard tool for studying morphology, surface characteristics, size, and homogeneity of materials.[194] SEM uses a high-energy beam of electrons (typically 1-20 kV) ejected from an electron gun and directed onto the surface of the sample. Upon interaction with the sample's surface, secondary electrons, backscattered electrons, and characteristic X-rays are produced and contain information about the sample's topology and chemical composition. The signals of the secondary electrons are transformed and generate the image of the sample, whereas the X-rays emissions determine the general elemental composition of the sample.

In this thesis, the objective was to study the size and morphology of the colloidal zeolite particles, and morphology of the honeycomb structure of the hybrid zeolite foams and mesoporous zeolite microparticles and their distribution throughout the spheres, in Chapter 5 and Chapter 6, respectively. SEM micrographs were obtained on a LEO Ultra 55 SEM from Carl Zeiss.

4.4 Nitrogen physisorption analysis

Nitrogen physisorption is a commonly used method to characterize the textural properties of porous materials such as specific surface area, pore size, pore volume, and pore size distributions.[195] The principle of this method is based on nitrogen adsorption at constant cryogenic temperatures over a certain range of pressures. The physisorption process occurs when the gas molecules interact with the surface atoms of the solid. The solid has a bonding deficiency at this temperature so that neither bonds can be broken nor formed, and only Van der Waals forces are involved.

In a typical experiment, the sample powder is weighed and dried to remove physically adsorbed molecules, and then it is transferred to a tube and attached to the instrument. The physisorption process begins with degassing the sample to remove remaining adsorbed molecules, and nitrogen is administered to increase the adsorptive pressure until the maximum pressure required and then the pressure decreases so the gas molecules are desorbed. The information obtained is transformed into adsorption/desorption isotherms, where the adsorbed gas is quantified against the relative pressure. Surface area, pore-volume, and pore size distributions can be determined from the isotherms. The specific surface area of the material can be calculated from the first adsorbed monolayer of nitrogen, using the well-known Brunauer-Emmet-Teller (BET) method.[196] The mesopore size was determined using he Barrett, Joyner, and Halenda (BJH) method

In this thesis, nitrogen isotherms were measured using a TriStar 3000 instrument from Micromeritics. The samples were degassed for a minimum of 5 h at 200°C under a nitrogen flow before these measurements. Nitrogen physisorption was used to measure the specific surface area, pore size distribution and pore volume in all the samples synthesized and prepared in this thesis in Chapter 5, 6 and 7.

4.5 Solid-state ^{27}Al magic angle spinning (MAS)-nuclear magnetic resonance (NMR)

Solid-state ^{27}Al MAS NMR spectroscopy is a powerful tool to study the aluminum species in zeolite frameworks. This technique can provide information about the chemical and geometrical environments of the aluminum within the framework, including the oxygen coordination, local symmetry, and concentration of aluminum species both in framework and extra-framework locations. In this thesis, we determined the coordination of aluminum within the MFI structure of ZSM-5 particles before and after acid-treatments by means of this method presented in Chapter 5. The ^{27}Al MAS-NMR spectra were recorded using a Bruker 500 MHz AVANCE III Solid State NMR Spectrometer at 130.32 MHz with a 4 mm XH CP MAS probe with acquisition parameters as follows: spinning frequency of 11 kHz, repetition delay was set to 0.5 s and 2048 scans for each sample.

4.6 Compression mechanical testing

Compression tests were conducted to determine the mechanical properties of the hybrid foams in this thesis and presented in Chapter 6. The tests were carried out in an Instron 5966 Dual Column Tabletop Testing System equipped with a load cell of 100 N. Prior to the compression test, the samples were conditioned for 40 h at 50 ± 5% relative humidity and 23 ± 2 °C. The compression test was performed at 25 °C and at a speed of 1 mm/min until the sample was compressed to 80 % of its original height or when 95 N of force was applied.

4.7 Thermogravimetric analysis (TGA)

Thermogravimetric analysis is a method that allows the determination of the mass of a sample as a function of temperature. The TGA measurements provide information about thermal stability, phase transitions, solid-gas reactions, chemi- and pshysorption, among others. In this thesis, TGA was used to measure the content of zeolite in the hybrid foams in Chapter 6 and the residual mass of the Fe/N-doped mesoporous carbons in Chapter 7. For the hybrid foams, the TGA measurements were carried out on a TA Instruments Discovery thermobalance from 30 to 700 °C under air atmosphere at 10 °C/min. For the carbon, the measurements were carried out on a Mettler TGA-DSC from 30 to 900 °C at 30 °C/min and isotherm at 900 °C for 20 min under air atmosphere. In addition, gravimetric gas sorption tests were conducted using N_2 and CO_2 at 25 °C to determine the gas uptake of the hybrid foams by the weight difference upon switching from N_2 to CO_2 atmosphere.

4.8 CO_2 and N_2 volumetric physisorption

This method is based on a mass balance principle which is based on measurements of pressures, volumes and temperatures. The volume adsorbed on the material is determined as a function of the equilibrium pressure at specific temperature. In the thesis, volumetric measurements were carried out for the hybrid foams to study their gas-sorption capacities. The volumetric CO_2 and N_2 adsorption isotherms were recorded using a Micromeritics ASAP 2020 adsorption analyzer at 35 °C. Prior to gas-adsorption measurements, samples were degassed under vacuum conditions for 10 h at 100 °C.

4.9 Small angle X-ray scattering (SAXS)

Small angle X-ray scattering (SAXS) is a technique that investigates the periodicity of materials at the mesoscale (*i.e.*, 1-100 nm) and provides details about the meso-order, morphology, orientation, among others.[197] In the thesis SAXS was used to identify the cubic order and determine the unit cell parameters of the Fe/N-doped mesoporous carbon, presented in

Chapter 7. The SAXS measurements were performed on a Mat:Nordic SAXS instrument from SAXSLAB using a Cu Kα radiation source.

4.10 Rotating disk electrode (RDE) measurements

RDE is a commonly used method for studying the electrocatalytic activity of electrocatalysts towards ORR in terms of both the electron transfer process on the catalyst surface and the kinetics near the catalyst. In this thesis, RDE measurements were carried out using a three electrode RDE setup from Gamry Instrument in 0.1 M $HClO_4$ solution. The results are presented in Chapter 7. In short, $Ag/AgCl_{sat}$ and a graphite rod (6 mm diameter) served as reference and counter electrode, respectively. The catalyst inks were prepared by mixing 10 mg catalyst, 95 µL Nafion® solution (5 wt% in lower aliphatic alcohols and water, Sigma-Aldrich) and 350 µL ethanol (99.5 % Solveco). After sonication (30 min) 5 µL of the ink was deposited on a polished glassy carbon rotating disk electrode (5 mm diameter, Gamry Instrument) and dried in room temperature for 30 min. The ORR polarization curves were recorded following a stepwise program, every 30 mV, with a hold time of 60 s, starting at 1 V to -0.25 V (versus RHE) in O_2-saturated electrolyte. The potential was held at the open circuit potential for 120 s before every polarization experiment. A polarization curve was measured for each catalyst at four different rotation rates (100, 400, 900 and 1600 rpm). The Koutecky-Levich equation was applied to the polarization curves at different rotation rates. The equation is presented below:[198]

$$\frac{1}{i} = \frac{1}{i_L} + \frac{1}{i_k} = \frac{1}{Bw^{1/2}} + \frac{1}{i_k}$$

$$B = 0.62nFAC_0D_0^{2/3}v^{-1/6}$$

Here, i_L is the diffusion limiting current and i_k the kinetic current. The coefficient B used to calculate the number of electron transfer mechanism for each catalyst was obtained from the Faraday constant (F=96485 mol^{-1}), the electrode area (A=0.196 cm^2), the concentration of O_2 in 0.1 M $HClO_4$ (C_0=1.2x10^{-3} mol L^{-1}), the diffusion coefficient of O_2 in 0.1M $HClO_4$ (D_0=1.93x$10^{-5}$$cm^2$ s^{-1}), and the kinetic viscosity in $HClO_4$ (v=0.00893 cm^2 s^{-1}).

4.11 PEM fuel cell tests

Electrochemical evaluations of the Fe-N-doped OMCs were conducted in a commercial 5 cm^2 single cell PEM fuel cell from Scribner Assoc. using an electrode area of 2.56 cm^2. The measurements were carried at 80 °C. The cell was fueled by fully humidified 100% H_2 and using synthetic air (instrumental grade from AGA) as a fully humidified oxidant. A total back-pressure of 1.5 bar was applied at both the anode and cathode side of the cell. Polarization

curves were measured for each catalyst in cycles (cyclic voltammetry) with a Gamry (Reference 600) potentiostat. PEM fuel tests are presented in Chapter 7 and Paper 5.

5. Controlled Growth of Colloidal Zeolites Governed by Solution Equilibria

As described in Chapter 2, zeolite formation has been thoroughly studied, especially for macrocrystal synthesis. However, gel-based synthesis presents multiple phases where the nucleation and growth involve several condensation and equilibria steps. Thus, the elaboration of a more rational explanation of the zeolite formation is still needed. With the advent of the synthesis of colloidal zeolite particles from clear homogeneous solutions over the past three decades, there has been a considerable increase in the number of studies to understand the crystal growth due to the synthesis of well-defined discrete particles. The synthesis of these particles in cooperation of the available characterization techniques facilitate the interpretation of the growth mechanism. In the following sections and in more detail in Paper 1 and Paper 2, we present a new growth model based on the role of chemical solution equilibria on the growth of zeolites and on the properties of colloidal particles.

5.1 Dynamic equilibrium between condensation and dissolution reactions in colloidal silicalite-1 synthesis.

In a study by Persson *et al.*,[26] a series of experiments demonstrated the effect of various synthesis variables on the linear growth rate, final particle size, conversion yield, and particle concentration in the synthesis of colloidal silicalite-1 particles. The study followed a synthesis recipe with molar composition:

$$9\ TPAOH : 0.1\ Na_2O : 25\ SiO_2 : 480\ H_2O : 100\ EtOH$$

After this, several studies followed the same recipe. In this thesis and in Paper 1, we neglected the presence of sodium since at this low amount it has shown limited effect on the synthesis of silicalite-1. Instead, we studied three syntheses with molar composition:

$$x\ TPAOH : 25\ SiO_2 : 480\ H_2O : 100\ EtOH$$

where x corresponds to 5, 9, and 12 to study the effect of the tetrapropyl ammonium hydroxide (TPAOH). Prior to the synthesis, a hydrolysis step was carried out at room temperature for 24 hours. The clear solutions were transferred to an oven and conducted at 98 °C in closed polypropylene bottles. In order to monitor the zeolite formation and characterize the products, different techniques were implemented as mentioned in Chapter 4.

The growth of colloidal silicalite-1 particles was studied for three syntheses and monitored with DLS, as shown in Figure 4. The syntheses are labeled Sx, where x corresponds to the value of TPAOH in the molar composition of the synthesis recipe.

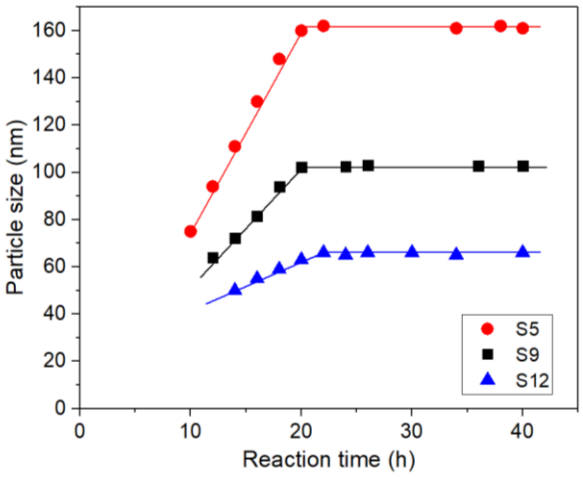

***Figure 4**. The average size of silicalite-1 particles as a function of reaction time for three synthesis mixtures, Sx, with the molar composition x TPAOH : 25 SiO_2 : 480 H_2O : 100 EtOH. S5 - red dots, S9 - black squares, and S12 - blue triangles.*

The three syntheses exhibited linear growth rates and final average particle sizes, in accordance with previous studies.[26,199,200]. It is observed that the linear growth rate and final particle size decreases as the TPAOH content increases. In addition, as the amount of TPAOH increases, the conversion becomes lower, whereas the particle concentration increases, as shown in Table 1.

***Table 1.** Influence of the TPAOH content on conversion yield of SiO_2 to silicalite-1, final average particle size, linear growth rate, particle concentration, and theoretical final average particle size expected for 100 % conversion yield in synthesis mixtures with molar compositions x TPAOH : 25 SiO_2 : 480 H_2O : 100 EtOH.*

Run (Sx)	Conversion yield (%)	Final average particle size (nm)	Linear growth rate (nm/h)	Particle concentration (#/g sol) · 10^{-13}	Theoretical final average particle size at 100 % conversion yield (nm)
S5	87.0	161	10.4	3.10	168.5
S9	65.5	105	5.3	8.01	121.0
S12	45.0	62	2.7	11.2	82.8

For all three runs, the growth of the particles suddenly stops before full conversion has been achieved and it is clear that the conversion yield decreases with increasing TPAOH content. This premature termination has not been extensively studied, and the aim of this thesis and in more detail in Paper 1 is, therefore, to establish that a pH-dependent dynamic equilibrium between the condensation and dissolution reactions can explain this behavior.

There are two realistic explanations for the termination of the zeolite growth. The first being the depletion of nutrients and the second a dynamic equilibrium between the rates of condensation and dissolution reactions has been reached. The first explanation is clearly not the case in this study, as evidenced by the less than 100 % yield and the remaining fraction of

zeolite precursor species in solution at the point when growth stops. Therefore, we will discuss the second explanation in the following to understand the termination of growth.

A series of post-synthesis experiments were conducted to describe the equilibrium between growth and dissolution as well as provide a method to circumvent the premature termination and obtain 100 % conversion yield. To this end, a series of post-growth and mid-growth adjustments were carried out varying the synthesis mixture´s pH using solutions of either 2 M HCl solution or 1M TPAOH. The colloidal particles exhibit almost spherical morphology and show the typical MFI crystalline XRD patterns (see Figure 5b) and textural properties typical of silicalite-1.

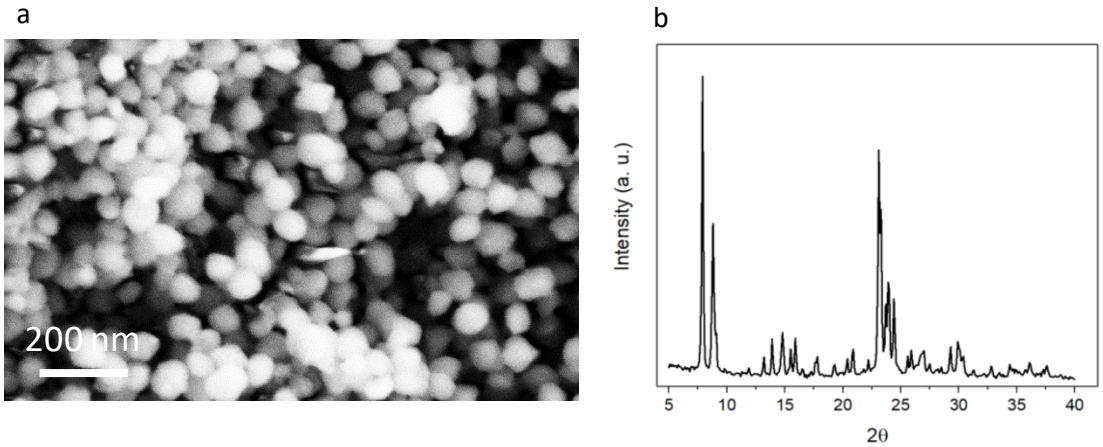

Figure 5. *a) SEM micrographs of colloidal silicalite-1 nanoparticles and b) XRD diffractogram of colloidal silicalite-1 nanoparticles for run S9.*

As an example, Figure 6 shows the development of the colloidal particles of the post-synthesis pH-treatment of the synthesis mixture in run S9 either with acid or base additions.

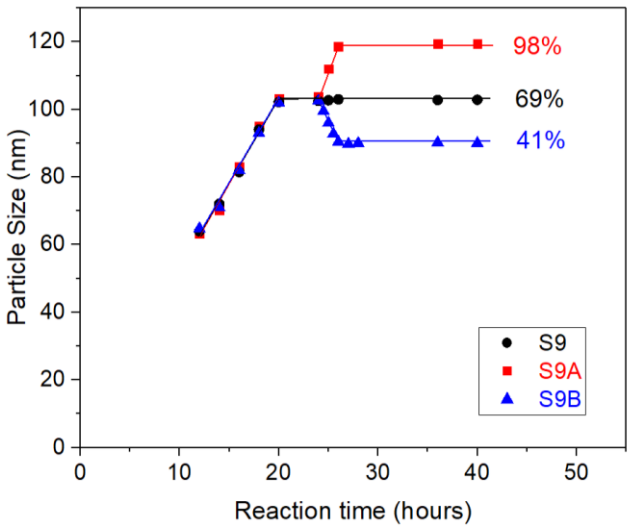

Figure 6*. The average particle size development as a function of reaction time for samples S9 - black dots, S9A – red squares, and S9B – blue triangles, where A and B stands for acid-adjusted and base-adjusted, respectively.*

After adding the HCl solution, a second particle growth is observed. An increase in both the final particle size and yield is obtained, reaching a new equilibrium between the zeolite particles and a new pH of the modified solution. Certainly, this shows that after changing the pH at the equilibrium, the condensation reaction is favored, leading to almost 100 % conversion. On the other hand, when the TPAOH solution was added to the synthesis mixture, a decrease in both the particle size and synthesis conversion is observed, indicating that the increase in solution´s pH favors the dissolution of the zeolites until a new equilibrium is reached again. This equilibrium is considered to be between the colloidal particles, silicate oligomers, and clusters of oligomers. Analogous results were found for the syntheses S5 and S12 following the same trend. Upon acid addition, there is an increase in particle size and conversion. Upon base addition, the particle size and conversion are reduced.

For comparison, we have calculated the diameter of the particle, assuming a spherical shape and constant concentration of particles and 100 % and 41% for S9 (see Table 2). The calculated diameters are in close agreement with the experimental values, thus evidencing that the pH changes do not affect the number of particles and only influence either the condensation or dissolution. The other syntheses show similar results, as shown in Table 2.

Table 2. *Influence of post-synthesis additions of HCl (S9A) and TPAOH (S9B), respectively on the conversion yield, final average particle size, linear growth rate, and particle concentration for a synthesis mixture with molar composition 9 TPAOH : 25 SiO_2 : 480 H_2O : 100 EtOH.*

Run (Sx)	Addition made at 24 hours	Conversion yield (%)	Final average particle size (nm)	Linear growth rate (nm/h)	Particle concentration (#/g-sol · 10^{-13})	Estimated final average particle size at conversion of 100% / (49% for S5, 41% for S9 and 32% for S12) (nm)
S5	-	87.0	161	10.4	3.01	168.6/132.9
S5A	HCl	99.5	170	10.4/6.0	2.92	-
S5B	TPAOH	49.0	134.3	10.4/-5.4	2.8	-
S9	-	65.5	105	5.0	8.01	121.0/89.5
S9A	HCl	98.5	122	5.0/7.4	7.91	-
S9B	TPAOH	41.0	90	5.0/-6.0	7.94	-
S12	-	45.0	62	2.7	11.20	81.0/55.3
S12A	HCl	93.0	80	2.7/8.3	10.97	-
S12B	TPAOH	32.0	56.7	2.7/-6.9	10.86	-

It is well known that the pH of the synthesis mixture increases as the zeolite grows as previously studied and reported.[199,201–203] In this case, the pH of the synthesis mixture was measured after the acid addition and after reaching the second equilibrium, and as expected, there is an increase in the pH value. This increase in the pH is associated with the release of hydroxyl ions during

the condensation reaction of the silicate species. On the other hand, the base adjustment of the synthesis mixture enables the dissolution reaction and, therefore, the consumption of hydroxyl ions, which lowers the pH. Curiously, the pH at the second equilibrium appeared to be lower than at the first equilibrium. This lower pH at the second equilibrium could be explained as a result of the release of silicate oligomers and the complex formation of the TPA cations and the silicate anions consuming hydroxyl ions.[204,205] These results clearly indicate a dynamic pH-dependent equilibrium that upon modification can influence the yield and final particle size. The rapid response to these adjustments favors the molecular growth mechanism over the "nanoslab" aggregation models, which to some extent, must still explain the fact of why colloidal zeolite particles stop growing before the full conversion has been reached.

In order to probe the dynamics of the equilibrium, experiments based on the run S9 were carried out. A series of pH adjustments were applied as outlined in Table 3 and the particle size development monitored , as shown in Figure 7.

Table 3. *Synthesis results at different post-synthesis pH adjustment of a synthesis mixture with the initial molar composition 9 TPAOH : 25 SiO_2 : 480 H_2O : 100 EtOH*

Time of adjusted pH (hours)	Addition acid/base	pH value before adjustment	pH value after adjustment	Initial average particle size (nm)	Final average particle size (nm)
24	Acid	13.35	11.4	103	121
40	Base	12.5	13.75	121	102.5
46	Acid	13.05	11.4	102.5	119
52	Base	12.4	13.65	119	103
58	Acid	13.0	11.4	103	118.5
66	Base	12.35	13.65	118.5	102.8

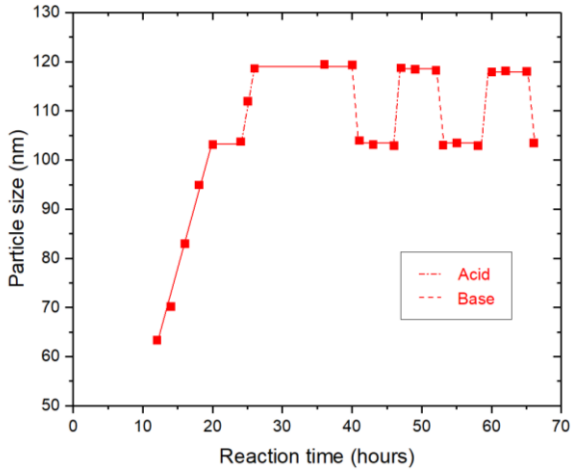

Figure 7*. The average particle size development as a function of reaction time for a synthesis mixture with the initial molar composition 9 TPAOH : 25 SiO2 : 480 H2O : 100 EtOH, following a series of post-synthesis pH adjustments performed by successive additions of acid and base, respectively.*

The cyclic adjustments of acid and base showed similar particle size and conversion results, indicating a robustness of the chemical system in re-establishing the dynamic equilibrium between growth and dissolution.

Supersaturation is considered the driving force for the nucleation and the growth of zeolites, according to previous authors.[206,207] During the formation of zeolites, supersaturation is initially increased and nuclei formation occurs, dictating the nucleation step. Further, as the growth of zeolites reaches the end, supersaturation is zero as the nutrients are typically depleted. However, in our study, the supersaturation is zero when the equilibrium between condensation and dissolution reactions has been reached, but there are still uncreacted nutrients in the solution. We find that supersaturation can be re-established by shifting the synthesix mixtures to conditions of lower solubility of the crystal and the silicate species, favoring condensation reaction over dissolution and resulting in continued growth as observed for the S*x*A runs. In addition, the supersaturation of the post-synthesis shows no effect on the nucleation as the number of particles remains constant.

It is now evident that the synthesis of zeolites follows dynamic chemical equilibria rules as a driving force for the formation or dissolution of zeolites. Besides, the full conversion of colloidal zeolites at low synthesis temperature conditions can be achieved by a proper pH adjustment of the synthesis mixture without modifying the concentration of particles. In addition, this can have a significant benefit to industrial manufacturing economics.

The effect of the post-synthesis acid adjustments revealed that the equilibrium is shifted towards condensation reaction, favoring the growth of zeolites, affecting the yield and final particle size but not the concentration of particles. The latter will be different if the pH-treatment is done at different stages during the reaction course. Thus, a series of mid-synthesis acid adjustment experiments were conducted as outlined in Table 4 to understand the effect of acid treatments on the growth rate, particle size, and more interestingly on the nucleation. Samples are denoted as S9-TH, where S9 refers to the molar composition of the clear solution, and TH is the reaction time in hours when the pH was adjusted.

Table 4. *Synthesis results at different pH adjustment times during modified S9 syntheses of silicalite-1*

Run	Time of adjusted pH (hours)	Conversion yield (%)	Final average particle size (nm)	Linear growth rate (nm/h)	Particle concentration (#/g-sol) $\cdot 10^{-13}$
S9	-	65.5	105	5	8.01
S9-0H	0	95.5	335	13	0.327
S9-1H	1	94.5	210	12.5	1.30
S9-3H	3	96.7	151	12	3.55
S9-4H	4	95.5	142	12	4.20
S9-6H	6	97.5	135	11.4	5.44
S9-8H	8	96.0	131	10.9	5.07
S9-12H	12	98.3	123	9	6.70
S9-18H	18	97.1	124	5 / 9.2	6.01
S9-24H	24	98.5	121	5 / 7.4	7.05
S9-30H	30	97.5	122	5 / 7.5	7.07

All the runs reached a yield between 95 and 99 %, which confirms that condensation reaction was favored over the dissolution throughout the course of the reaction. The effect of pH adjustment on the concentration of particles was more visible at the early stages (0 to 8 hours) of the reaction. The particle size exhibited a more significant increase and then decreased rapidly to a constant value, as shown in Figure 8. The relation of the concentration of particles and particle size indicates that after 8 hours of reaction for S9, no new nucleation occurs. This result indicates that the acid addition to the samples in the range of 8 to 30 hours only affects the growth of zeolites, favoring a second growth, whereas the samples at times earlier than 8 hours, the acid influences both the nucleation and growth. In this context, the nucleation at these samples might be longer than of S9 as a result of the sudden boost of viable nuclei.

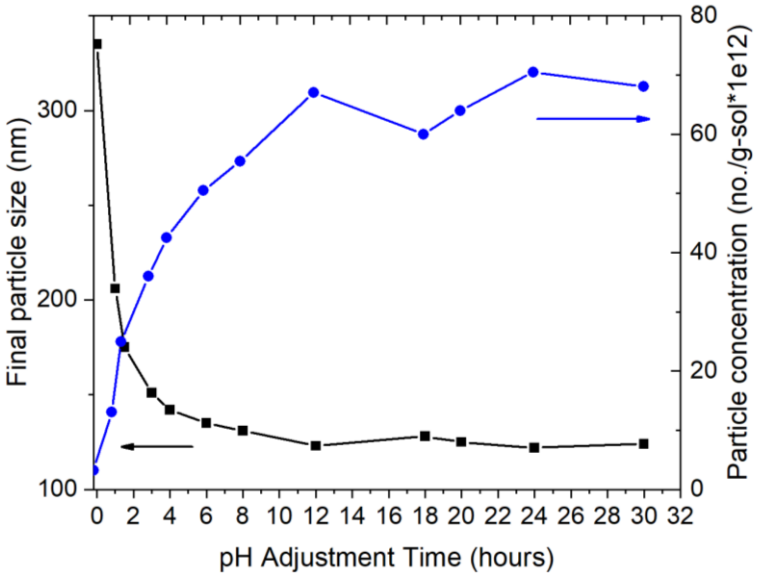

***Figure 8**. Variation of final particle size and particle concentration with pH-adjustment time.*

The linear growth rates are affected by the pH adjustment, observing high growth rates at early stages during the reaction and then decreasing at later stages. The high growth rates can be associated with the high supersaturation as the concentration of nutrients at the beginning of the reaction is also higher compared to the low amount of nutrients by the end of the growth stage. This trend is in agreement with what has been previously reported.[206] However, the higher supersaturation obtained by the acid adjustment does not generate a higher number of viable nuclei based on the presented results. Instead, the samples with the highest initial supersaturation have a lower concentration of particles, which seems to be in contradiction because of the higher the supersaturation, the smaller the viable nuclei radius.[208] This could infer that the increase in supersaturation has a larger impact on the growth rate than on the nucleation stage, resulting in fewer nuclei causing the nucleation time to be larger.

5.2 Solution Equilibria Controlled Growth of Colloidal Zeolite ZSM-5

Colloidal ZSM-5 particles were synthesized for the first time by Persson *et al.*[209] Different synthesis variables *(e.g.*, alkalinity, SiO_2/Al_2O_3 ratio, water content) and their effect on the crystal growth properties were investigated. One of the first findings concluded that as the SiO_2/Al_2O_3 ratio is lowered, the yield is significantly reduced, evidencing the influence of the alumina on the crystal growth. One of the possible explanations given by the authors was that systems with low SiO_2/Al_2O_3 ratios require higher synthesis temperatures so that crystalline products are yielded. Thus, another study in synthesis of colloidal ZSM-5 particles were conducted at higher temperatures (*e.g.*, 160 ºC) for synthetic systems with lower SiO_2/Al_2O_3.[210] Although the increase in temperature did improve the synthesis conversion, it was not enough to reach full conversion.

As presented in the previous section and Paper 1, chemical solution equilibria seem to be the driving force for the growth of colloidal silicalite-1 particles. In this section and in more detail

in Paper 2, we present the solution equilibria model applied to ZSM-5, a system that includes the presence of aluminum.

Three sodium-free ZSM-5 syntheses were considered for this study. Their molar composition:

$$9\ TPAOH : 25\ SiO_2 : x\ Al_2O_3 : 480\ H_2O : 100\ EtOH$$

where *x* is either 0.25, 0.33 or 0.5 (corresponding to SiO_2/Al_2O_3 ratios: 100, 75 and 50).

Figure 9 shows the growth of the three ZSM-5 syntheses compared to silicalite-1 that has the same molar composition except for the alumina content. The three syntheses exhibit linear growth until no change in the particle size is observed. The time when the particles stop growing is gradually decreased as the SiO_2/Al_2O_3 ratio is reduced. This behavior suggests that longer times are needed to crystallize indicating that the growth rate is also reduced.

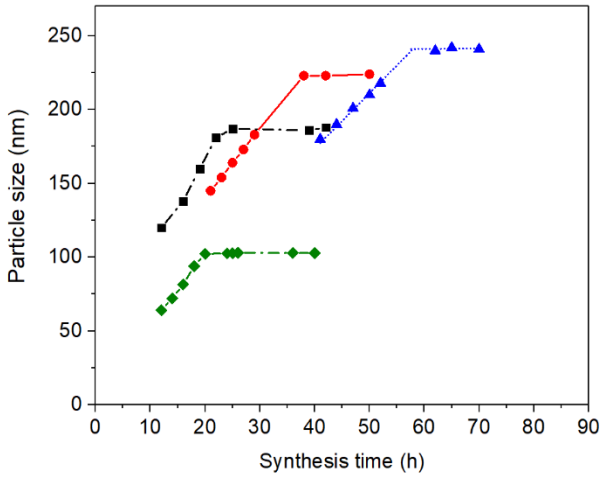

Figure 9. *The average size of ZSM-5 particles development as a function of reaction time for synthesis Z100 (black squares), Z75 (red dots), Z50 (blue triangles) and Al_2O_3-free silicalite-1 (green diamonds).*

In comparison with silicalite-1, the introduction of the aluminum in the synthesis mixture considerably affects the crystal growth and the particle size development. As shown in Figure 9, the particle size increases with the alumina-content in agreement with previous studies. The increase in the particle size also affects the specific surface area of the crystals (see Table 5). Hence, the specific surface areas showed a decreasing trend as the particle size is larger. In addition, the increase in the particle size suggests that aluminum not only affects the growth but also the nucleation, as the number of particles is lower despite the low conversion as shown in Table 5. The low number of particles and large final particle size are indications that the difficulty of the aluminum incorporation in the nuclei has a substantial effect on the nucleation stage, slowing down the formation of nuclei as well as the crystal growth.

The SiO_2/Al_2O_3 ratio of the synthesized ZSM-5 particles was determined by XRF and, as observed in Table 5, showed that all the three determined ratios were higher than the initial composition in the clear solutions. The higher value could be explained by the absence of sodium cations in the synthesis mixture as they act as charge compensators and facilitate the aluminum incorporation into the framework.[211]

Table 5. *Influence of the Al_2O_3 content on SiO_2/Al_2O_3 ratio, specific surface area, linear growth rate conversion yield of ZSM-5 particles, final average particle size and particle concentration in synthesis mixtures with molar compositions 9 TPAOH : 25 SiO_2 : x Al_2O_3 : 480 H_2O : 100 EtOH.*

Sample	Clear solution composition *x*	SiO_2/Al_2O_3 ratio[a]	BET surface area (m^2/g)	Crystal Growth rate (nm/h)	Conversion of MO to MFI (wt.%)[b]	Final average particle size (nm)	Particle concentration (#/g sol) · 10^{-13}
Z100	0.25	118	442	5	51	187	0.58
Z75	0.33	86	423	4.3	38	224	0.23
Z50	0.5	72	406	3.4	15	241	0.11

[a)] The SiO_2/Al_2O_3 ratio was determined by XRF.
[b)] Conversion calculated from the metal oxides (MO) (SiO_2 and Al_2O_3)

By ^{27}Al MAS NMR measurements it was possible to determine that the aluminum incorporated into the framework is tetrahedrally coordinated and no significant extra-framework aluminum was found.

The syntheses showed the characteristic sudden termination of the zeolite growth, as observed in Figure 9 as a constant particle size plateau at the end of the synthesis. Low temperature in the synthesis has been suggested as one of the causes that explains this abrupt termination of the crystal growth, since high temperature is required to overcome the kinetic barrier to generate nuclei faster and boost the crystallization.[210,212] However, this explanation does not completely provide a more mechanistical argument to explain the sudden stop in the crystal growth. In the previous section, we provided a better understanding of such behavior and concluded that it is associated to a dynamic equilibrium between the growth and dissolution reactions. Besides, the equilibrium is pH dependent and involves the solubility of the species in solution and their chemical equilibria to dictate the zeolite growth.

Thus, a series of experiments were performed to attest if the chemical solution equilibria mechanism derived for the growth of silicalite-1 particles could also explain the sudden termination of ZSM-5 growth. Similarly, as in the previous section for silicalite-1 and in Paper 1, the pH of the three systems was reduced using HCl when the particle growth had terminated.

Figure 10 shows the development of the particle size after the pH adjustment of the synthesis mixtures and further continuation of the reaction. It is clear that the acid addition affected the growth, resulting in a second growth stag, proceeding until another equilibrium is reached and the particle once more stop growing. The new final particle sizes and new yields are summarized in Table 6. The acid-adjusted samples are denoted Z*y*-A

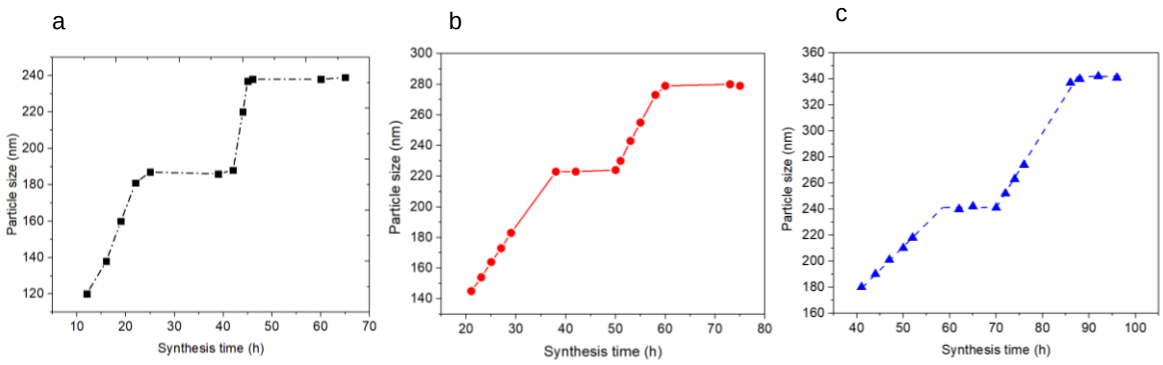

Figure 10. *The average particle size development as a function of reaction time for samples a) Z100-A (black squares); b) Z75-A (red dots) and c) Z50-A (blue triangles).*

Table 6 *Influence of post-synthesis additions of HCl in the Zy-A syntheses on the SiO_2/Al_2O_3 ratio, specific surface area, linear growth rate, conversion yield of ZSM-5 particles, final average particle size and particle concentration in synthesis mixtures with molar composition 9 TPAOH : 25 SiO_2 : x Al_2O_3 : 480 H_2O : 100 EtOH*

Sample	Clear solution composition *x*	SiO_2/Al_2O_3 ratio after pH change	BET surface area (m^2/g)	Crystal Growth rate (nm/h)	Conversion of MO to MFI (wt%)	Final particle size (nm)	Particle concentration (#/g sol) · 10^{-13}
Z100-A	0.25	105	408	10	93	239	0.63
Z75-A	0.33	78	398	6	82	281	0.20
Z50-A	0.50	58	382	5.5	63	343	0.08

.

The increase in the particle size is in agreement with the model of a dynamic equilibrium that controls the crystallization of ZSM-5 particles as evidenced in our previous results for silicalite-1. This equilibrium can be tuned by changing the pH of the synthesis solution. Lowering the pH affects the alkalinity of the synthesis mixture, demonstrating, as previously reported by Persson *et al.*, that reducing the alkalinity shows an increase in the growth rate indicating that the silanol condensation reaction is favored over the dissolution reaction.

This also proves that by lowering the pH, the solubility of the ZSM-5 particles is reduced, which means that the acid adjustment increases the supersaturation of the solution in favor of the condensation reaction causing the particles to continue to grow until a new equilibrium between growth and dissolution is once more reached. Curiously enough, the SiO_2/Al_2O_3 ratio of the Z*y*-A samples is lower in comparison to the Z*y* samples and close the overall synthesis mixture values. This indicates that aluminum was inserted more readily into the zeolitic framework as the pH was lowered. We find that the incorporated aluminum is 100 % tetrahedrally coordinated as evidenced by the ^{27}Al MAS NMR and the XRD patterns of the samples shown in Figure 11, and no differences in these regards were found in comparison with the samples before acid adjustments .

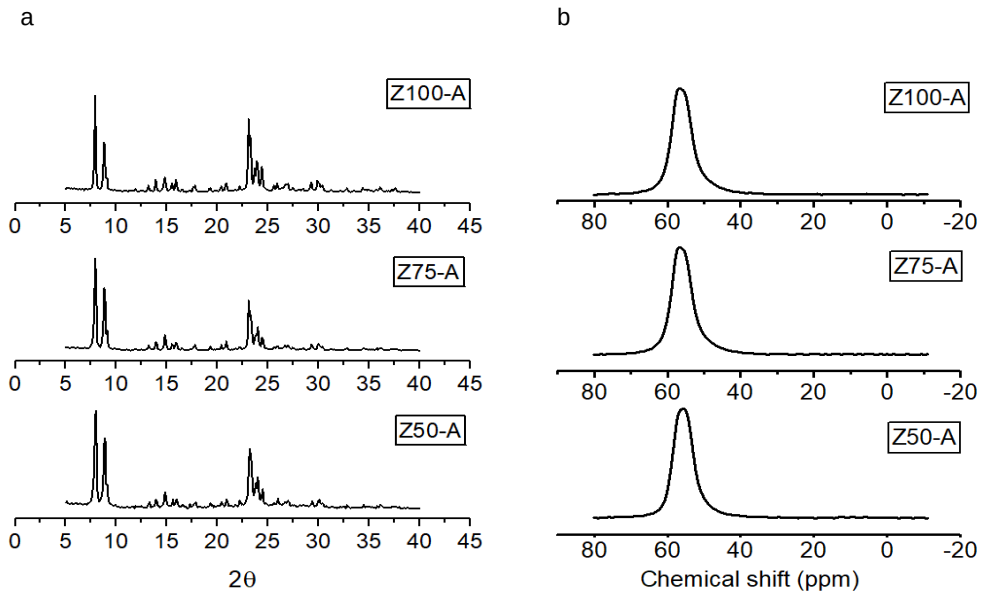

Figure 11. *a) Powder X-ray diffractograms and b) ^{27}Al M.A.S. NMR spectra of colloidal ZSM-5 nanoparticles in the Zy-A series with different SiO_2/Al_2O_3 molar ratio after acid adjustment.*

The incorporation of aluminum to the crystalline framework can be associated with the increase in the pH during the crystallization of ZSM-5.[213] The change in the pH is attributed to the release of OH^- groups as a result of the condensation reactions *via* two mechanisms: i) nucleophilic attack between solvated silicate species and aluminate centers at the surface of the growing zeolites and ii) nucleophilic substitution between deprotonated silanol groups and solvated aluminate species.[214] These dynamic reactions are dependent on the solubility difference of the species in solution. This indicates that upon lowering the pH at the equilibrium, the solubilities of the silicates, aluminates and growing particles are affected and shift the equilibrium towards condensation reaction. The condensation reaction yields a second growth stage and therefore an increase in the pH is observed which is translated into the incorporation of silicon and aluminum into the framework.

In our previous study of silicalite-1, we found that by lowering the pH after the first equilibrium was reached, the condensation reaction was favored sufficiently much that when the second equilibrium was reached, the conversion was very close to 100 %. In the present study for samples Z*75*-A and Z*50*-A, the conversion was only 82 and 63%, respectively when the second equilibrium. In this case, it is worth to mention here that the amount of HCl added to the three Zy samples was different because at the higher alumina content the reduction of the pH in the solution led to a gelation of the synthesis mixture. This is explained by the solubilities of the aluminosilicate species in solution, especially when an increase in the alumina content significantly reduces the solubility of the silica as observed by Iler.[78] In addition, the increase in the alumina content at fixed silica concentration and the change of the pH of the solution generate a solubility boundary that is translated as the stability of the aluminosilicate.[215] Thus, if the pH is reduced, the aluminosilicates form flocs of solid mixtures (*i.e.* gelation) but if the

pH increases, more soluble species are generated. In the present work, each solution was adjusted to a minimum pH value possible without inducing gelling.

This will certainly influence the equilibrium between condensation and dissolution reactions and thus affect the solubility of the species in solution and the supersaturation and thereby result in different yields. Attempts of further post-additions of acid after the second growth were conducted but caused the synthesis solutions to gel and preventing the growth to be followed further.

These findings clearly show that the introduction of alumina shifts the dynamic equilibrium between condensation and dissolution in favor of dissolution, most likely by slowing down the condensation reaction.[78] The result of this is a lower yield for the same 9 TPAOH value compared to silicalite-1 results in Paper 1

6. Applications of colloidal zeolites

In Chapter 5, we studied the synthesis of colloidal zeolites wherein the mechanism of formation allows for control of the particle size, yield, and chemical composition of the product by judicious selection of certain synthesis parameter values. Being able to control and monitor the synthesis of zeolites gives a tremendous advantage on how to tailor the properties of zeolites for more specific applications. Once we can prepare tailor-made zeolites, we may evaluate their use in more target-oriented applications. In the present chapter, we will introduce and study two applications using colloidal zeolite particles and more details are given in Paper 3 and Paper 4.

6.1 Mesoporous zeolites prepared by colloidal assembly

The colloidal assembly of silica nanoparticles has recently been investigated so that mesoporous silica microspheres are prepared with a high level of tuneability over the pore size and pore volume.[216] This strategy exhibits excellent reproducibility and does not require ageing steps, use of a mesoporogen or post-treatment steps. This method was investigated by two different approaches: evaporation-driven and gelation-driven colloidal assemblies. The evaporation-driven colloidal assembly is a method in which the randomly suspended nanoparticles within emulsion droplets are driven into close packing by gradually evaporating the liquid until the nanoparticles assemble into larger particles, called supraparticles or supracolloids.[216–218]

Similarly, in this thesis and Paper 3, we present an evaporation-driven template-free colloidal assembly procedure to prepare hierarchical micro-/mesoporous zeolite microspheres (MZMs). In brief, colloidal sols of silicalite-1 particles were prepared as in Chapter 3, following the recipe from Persson *et al.*[26] The emulsion preparation was conducted by mechanical stirring of a mixture of 3%-wt hydroxypropyl cellulose (HPC, Mw ~100,000 g/mol) solution and phenethyl alcohol as the oil phase. The colloidal zeolite sol was added under constant stirring to form a water-in-oil (W/O) emulsion. After a certain time, the emulsion was transferred to a rotary evaporator, and the emulsion was evaporated at 65 ºC and vacuum condition. The remaining liquid was then vacuum filtered to obtain a white powder that was dried and calcined at 650 ºC. The colloidal silicalite-1 sols were characterized by DLS, and the products were characterized by SEM, XRD, and nitrogen-physisorption.

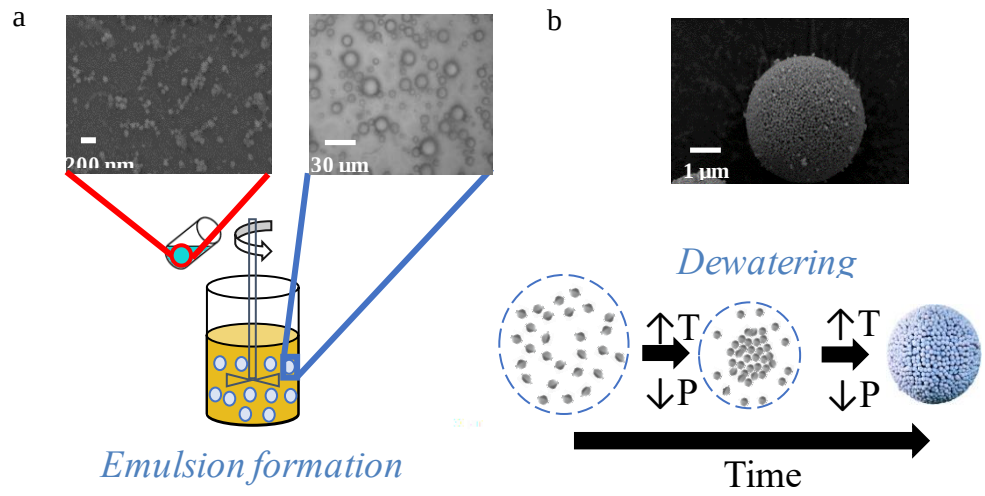

Scheme 2. *General synthesis of mesoporous zeolite microparticles (MZMs) prepared by colloidal assembly. a) Formation of water-in-oil emulsion with colloidal silicalite-1 particles, b) evaporation of emulsion and formation of hierarchical micro-/mesoporous zeolite spheres via assembly of the colloidal silicalite-1 particles(Taken from reference[131]).*

The formation of hierarchical MZMs is shown in Scheme 3. Colloidal silicalite-1 particles are distributed within the spherical water droplets as the emulsion is formed. Afterward, the evaporation at mild temperature and low pressure induces the colloidal assembly, in which the slow shrinkage of the droplets makes the zeolite nanoparticles aggregate and gel, forming spherical micro-sized particles. Such a gelation process occurs due to the formation of siloxane bridges between the silicalite-1 particles through the reaction of superficial isolated deprotonated silanol groups.

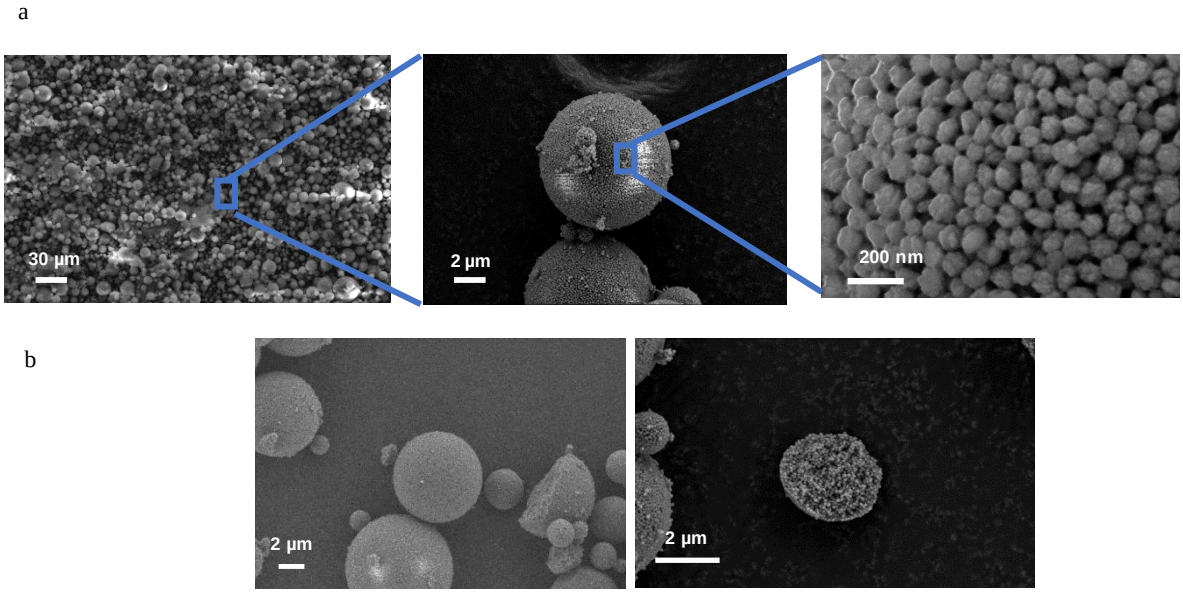

Figure 12. *SEM micrographs of the a) obtained silicalite-1 MZM spherical particles, and b) cracked silicalite-1 MZM particles.*

As products, perfect microspheres are obtained, as shown in the SEM micrographs in Figure 12a. This result indicates that the slow dewatering process induces the colloidal assembly into densely close-packed spheres, and this is evidenced in the cracked spheres (Figure 12b), in which a homogeneous distribution of the colloidal silicalite-1 particles is achieved. The mesopores are formed as a result of the aggregation of the particles creating a gap in between, and therefore, a well-connected porous network is generated. This porosity is evident in the nitrogen-sorption isotherm with a typical Type-IV isotherm, characteristic of the mesoporous materials compared to the colloidal zeolites that exhibited a Type-I isotherm, typical of microporous materials (see Figure 13a). The isotherm also shows a steep uptake at low pressures corresponding to the microporosity. The mesopore size distribution determined by Barrett–Joyner–Halenda (BJH) model have an average size of 38 nm that are in close agreement with SEM that determined pore sizes of 20-40 nm (see Figure 13b). This result clearly shows that the mesopore size, in this case, can be described as the distance generated by stacking spherical particles, which is approximately one-third of the particle diameter, considering that the zeolite nanoparticles have an average diameter of 105 nm based on DLS measurements. This method offers the possibility of tailoring the mesopore size of the mesoporous zeolites by a rigorous selection of zeolite nanoparticles with different diameters.

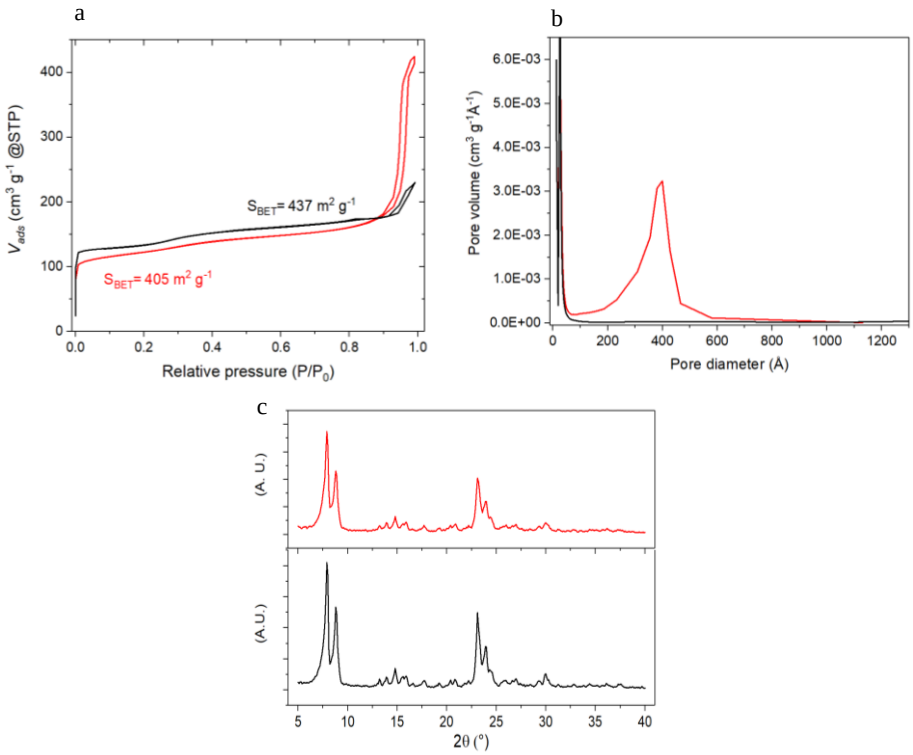

Figure 13. *Characterization of colloidal silicalite-1 sol and silicalite-1 MZM particles. a) N_2 adsorption/desorption isotherms of colloidal silicalite-1 particles and silicalite-1 MZMs, b) N_2 adsorption based pore size distribution of colloidal silicalite-1 particles and silicalite-1 MZMs, and c) X-ray diffraction patterns for colloidal silicalite-1. (Black line: colloidal silicalite-1 particles; red line: silicalite-1 MZMs).*

The synthesized MZMs showed the typical MFI crystalline patterns as observed in Figure 13c, indicating that the colloidal assembly did not affect the crystalline structure of the of the colloidal silicalite-1 particles.

The MZM particles exhibit one of the highest pore volumes (0,64 ml) among the reported mesoporogen-free methods for preparing mesoporous zeolites, as outlined in Table 7, which is a very positive outcome since many applications in adsorption and separation of molecules, require high pore volumes. In addition, this method has a very high yield, close to 100%, as it is a physical process rather than a chemical. Also, this method has the shortest preparation time and lowest preparation temperature, offering the possibility for mass production at a low manufacturing cost.

Table 7. *Comparison of total pore volume, preparation temperature, and time of secondary template-free methods for mesoporous zeolites.*

Method	Type of Zeolite	V_{total} (cm^3/g)	Preparation temperature (K)[a]	Preparation time (days)[b]	Reference
Evaporation-driven colloidal assembly	Silicalite-1	0.64	358	0.5	**This work**
Nanocrystal aggregation	ZSM-5	0.25	408	1-4	**Wang et al.** [219]
Self-pillared zeolite nanosheets	ZSM-5	0.7	388	1-3	**Zhang et al.**[220]
Steam assisted conversion (SAC)	ZSM-5	0.22	443	3	**Jia et al.**[221]
Rod-like nanocrystal assembly	ZSM-5	0.42	423	3	**Zhang et al.** [155]
Crystallization amorphous gel	Silicalite-1	0.11*	370	2-8	**Naik et al.**[222]

This method has thus proven to be very versatile, preparing mesoporous silica particles and now mesoporous zeolites. However, so far solely particles with one narrow size distribution and the same chemical nature have been used. Herein, we have prepared mesoporous zeolites incorporating colloidal silica particles of a different size. For that, we mixed a 50 wt-% sol of colloidal amorphous silica nanoparticles of approximately 30 nm in diameter and 50 wt-% sol of the colloidal silicalite-1 particles and prepared mesoporous microspheres following the procedure described in Scheme 3. Figure 14a shows the SEM micrographs of the resultant mesoporous zeolite/silica microsphere (MZSM) particles and the nitrogen-isotherm and its corresponding pore size distribution.

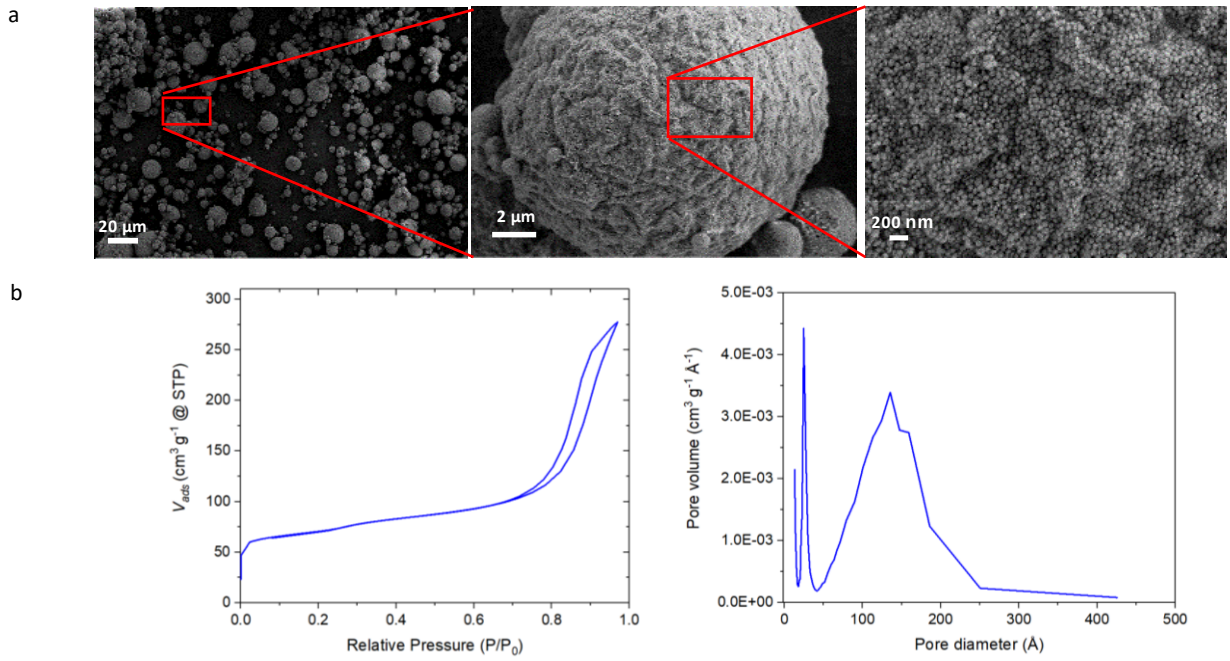

Figure 14. *Characterization of MZSM particles. a) SEM images of the prepared MZSMs particles. b) N_2 isotherm and N_2 adsorption pore size distribution of the MZSMs.*

The MZSMs exhibit a quasi-spherical morphology with a wavy ridge-like surface pattern. The formation of this particular morphology could be caused due to the differences in particle size and morphology of the particles since the silica particles have a smaller particle size and a more spherical morphology compared to silicalite-1 particles and this could affect the homogeneity of the colloidal assembly. In the MZSM particles, a reduction in mesopore size is observed in the SEM micrographs and confirmed by the nitrogen adsorption of the particles. The hysteresis loop of the nitrogen isotherm has a slightly flatter slope, indicating that the desorption of nitrogen from the pore network is more restricted than in the MZMs due to a network with smaller pore size (see Figure 14b). The reduction is also observed in the determined BJH pore size distribution, wherein the average pore size at 38 nm of the MZMs is lowered to 15 nm for MZSMs. This result shows that by mixing smaller silica nanoparticles with the silicalite-1 nanoparticles, a substantial reduction in the mesopore diameter can be achieved, since the small nanoparticles may be placed in between the silicalite-1 nanoparticles as observed in Figure 14a, partly filling the interspace between the silicalite-1 particles and therefore forming a new smaller interspace.

This new method could enable the preparation of multifunctional catalysts by using mixtures of other types of colloidal zeolites or functional nanoparticles. This protocol will be beneficial for specific applications that might require multiple properties in the material, *e.g.*, acid/base/redox catalytic activity or selectivity and/or molecular sieving effects. Besides, this new method provides a new pathway for production of hierarchical porous zeolites with well-defined morphologies or other hierarchically functional materials of industrial importance.

6.2 Hybrid zeolite bio-based foams for CO_2 capture

Zeolites have shown positive results towards CO_2 separation from flue gases. However, zeolites are commonly obtained in aggregated powder form, limiting their implementation in many scaled-up applications such as gas separation systems. The employment of adhesives and inorganic binders from zeolite-based materials typically leads to pore blockage and reduced gas uptake. In this context, a zeolite-composite material using a porous supporting material could potentially improve the system efficiency.

Bio-based polymers, specifically nanocellulose, represent an attractive alternative as porous supporting materials, from the environmental point of view as they are derived from abundant renewable sources and due to their biodegradability, inexpensiveness, versatility of functionalization, and low density. Recently, foams, which are porous materials with open cells and extremely low densities, have been widely investigated for several applications, including heat-insulating materials, supercapacitors, super-absorbents, among others. [9,10] Nanocellulose foams have been used to grow leaf-like zeolitic imidazolate frameworks (ZIF-L), generating a multifunctional composite with ultra-light weight and good mechanical properties and a loading of 21-50% of ZIF-L, which exhibited good CO_2 uptakes in comparison with other MOF materials.[223]

In this work and more detailed in Paper 4, hybrid zeolite-nanocellulose foams with high loadings of zeolites were prepared for CO_2 capture. For such preparation, colloidal silicalite-1 particles were used as a model system. The synthesis of the colloidal silicalite-1 was done following the recipe by Persson *et al.*[26] The matrix of the foams consisted of 2,2,6,6-tetramethylpiperidine-1-oxyl radical (TEMPO)-oxidized cellulose nanofiber (TOCNF) and gelatin.

In short, colloidal silicalite-1 particles were mixed with TOCNF and then combined with a gelatin suspension using a high-speed disperser. The mixture was then transferred to molds and cooled down at 4 ºC for 1 h. Finally, the mixture was degassed and subject to freeze-casting employing dry-ice.

The preparation of hybrid foams using nanocellulose-gelatin exhibited the highest loading of colloidal silicalite-1 particles (*i.e.*, 90 wt.-%) that has ever been reported. This value was determined by gravimetric measurements. The strongly interconnected network generated by the electrostatic interactions between the cellulose and gelatin could support the zeolite particles

(see Scheme 4). As observed in SEM-EDS maps in Scheme 4, the hybrid foams show a homogeneous distribution of the different components, especially the colloidal zeolite particles.

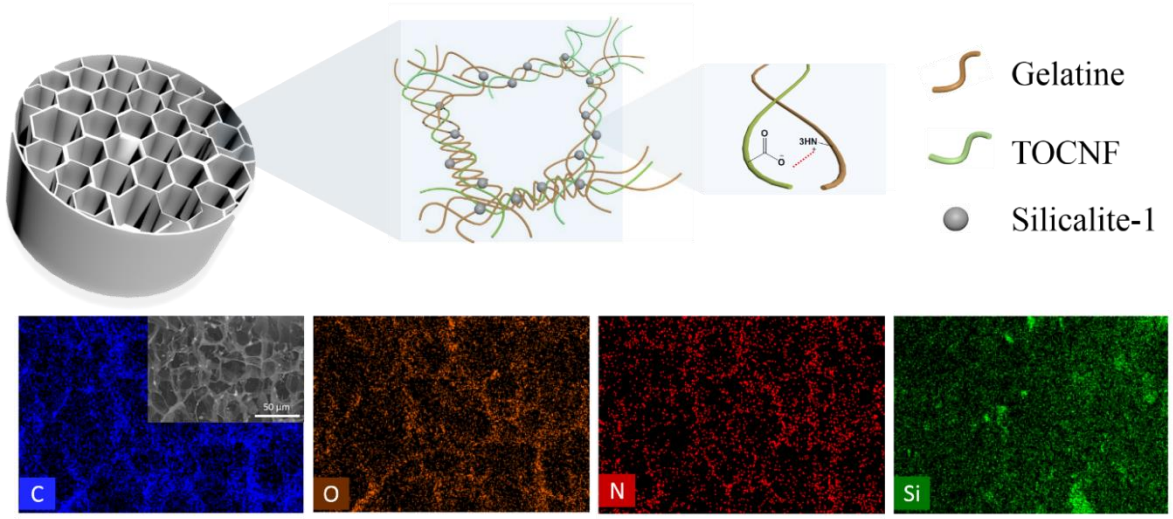

Scheme 3. *Conceptual schematic illustration of the network between gelatin/TOCNF and silicalite-1 and the EDS mapping showing the distribution of the elements in the hybrid foam. (Scale bar = 50 µm) (Taken from reference.*[224]*)*

The hybrid foams have a tubular honeycomb structure, as illustrated in Scheme 4, and imaged in Figure 15. The pore structure of the foam contains macropores of around 40 microns as a result of the unidirectional freeze-casting effect. During the foam preparation, the zeolite particles seem to aggregate and are found to be located at the walls of the foam. Additionally, it was observed that at higher concentrations of silicalite-1, more aggregates appear and show no alteration of the foam's porous structure. This aggregation was indirectly evidenced in the compression tests, as shown in Figure 16. All the samples exhibited the characteristic compressive deformation behavior of foams. However, a detrimental decrease is observed in the stress-strain behavior. Therefore, the elastic modulus as the silicalite-1 content increases, indicating that the foam's stiffness was affected presumably by the zeolite aggregates, as already shown in Figure 15. Although there is a decrease in the stiffness, it is the absorption energy, which is the crucial mechanical property. A significant increase in the absorption energy is observed as the silicalite-1 increases, which could occur due to the increase in the wall density generated by the high content of silicalite-1 particles.

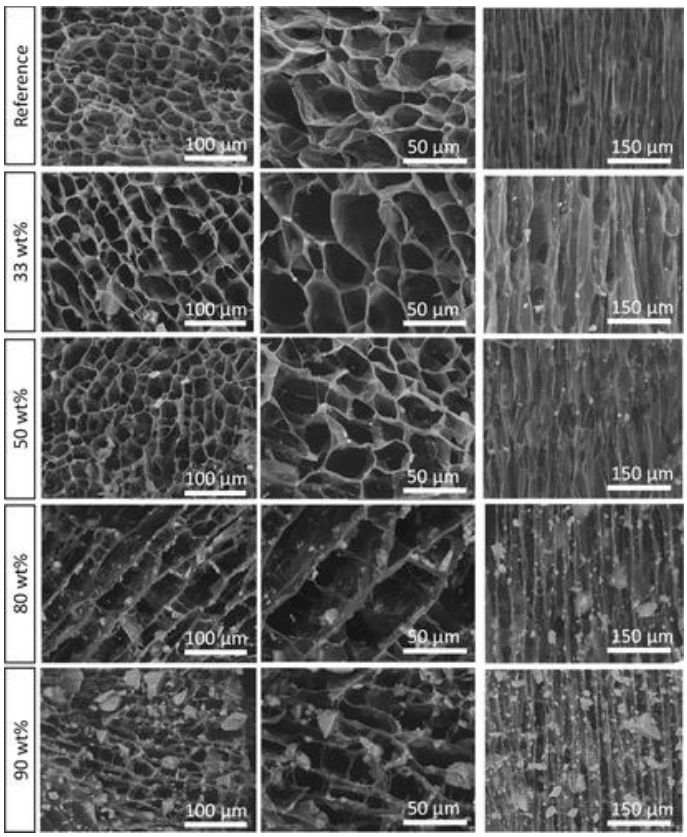

Figure 15. *SEM micrographs of hybrid foams with different mass fractions of silicalite-1. The right column corresponds to the cross-sectional micrographs.*

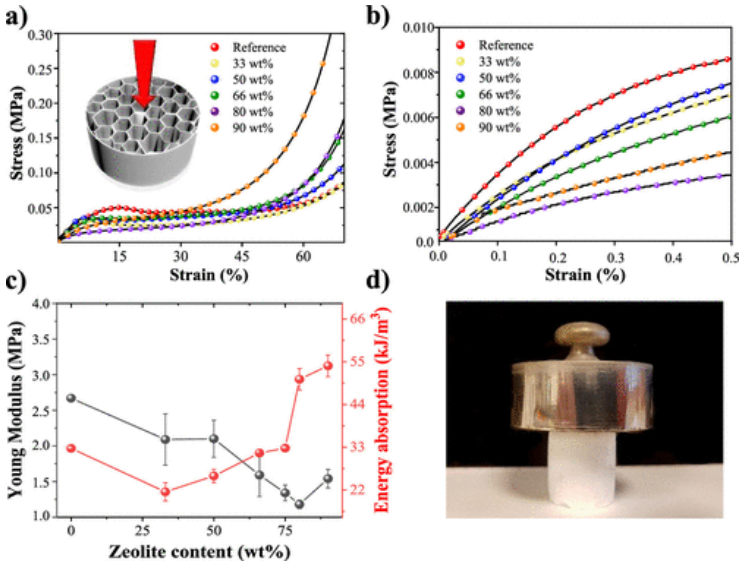

Figure 16*. Stress-strain plots showing the compressive mechanical properties of foams with different zeolite content (a,b); compressive modulus and energy absorption of foams with different zeolite content (c); photograph of hybrid foam comprising 50 wt % content of silicalite-1 withstanding 100 g of weight (d).*

The silicalite-1 content has shown important effects on the morphology and mechanical properties of the hybrid foams, which will also influence other properties. Thus, the specific

surface area and pore size distributions were investigated by N_2-sorption. As shown in Figures 17a,b and c, the silicalite-1 content led to a significant increase of the porosity observed as a quasi-linear relation of the pore volume, microporous surface area, and specific surface area as a function of silicalite-1 content. The presence of silicalite-1 particles enables the introduction of microporosity to the hybrid system, as observed in Figure 17d, in which a steep increase is found below 10 Å. These results evidenced that silicalite-1 particles can be accommodated on the foam´s wall without generating significant pore blockage critical for CO_2 adsorption.

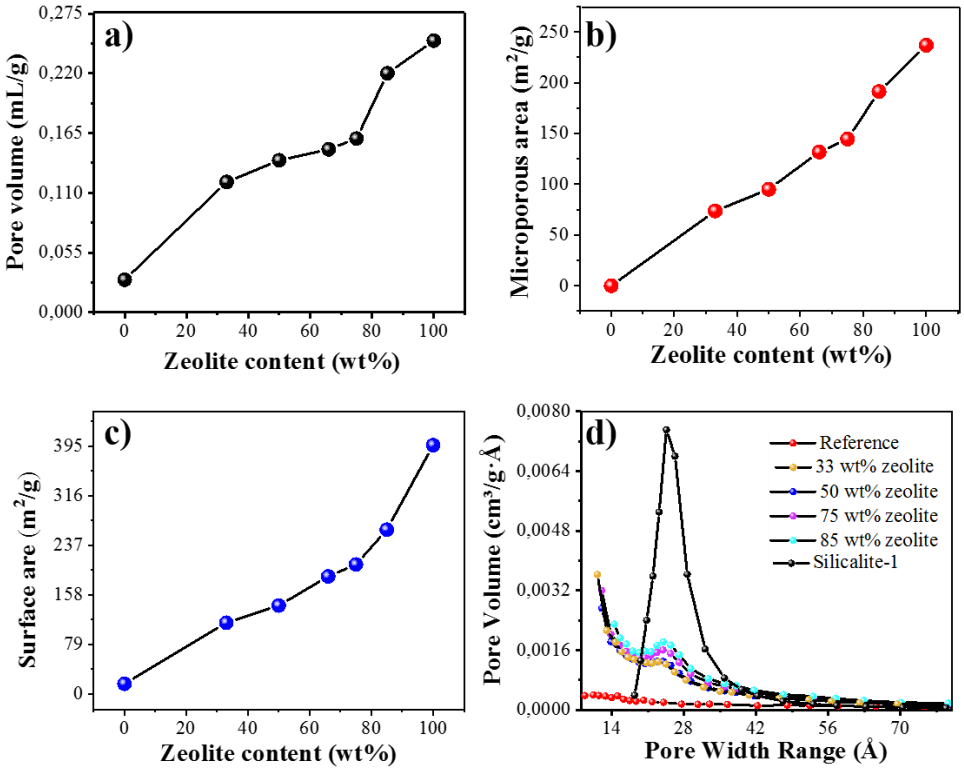

Figure 17. Influence of zeolite content on the specific pore volume (a); specific microporous surface area (b); specific surface area (c); and pore size distribution (d) in the hybrid foams.

The CO_2 adsorption isotherms of the hybrid foams are shown in Figures 18a and b. The incorporation of silicalite-1 particles in the foams increases the CO_2 adsorption capacity due to the microporosity of the zeolites, showing a linear relationship as a function of the silicalite-1 content. The linear relationship also shows that nanocellulose nanofibrils/gelatin porous networks mainly act as support for the zeolite particles and do not block the zeolites´ pores. Instead, the porosity of the network could generate access to the gas molecules. Noteworthy is that despite the silicalite-1 framework is a pure-silica without exchangeable cations, it can adsorb CO_2 molecules through Van der Waals interactions in the channels of the MFI framework.[225]

The N_2 adsorption on the foams was significantly lower as expected for the nitrogen molecule as a result of its low polarizability.[226] This shows that the hybrid foams are more selective

towards CO_2 over N_2, and this suggests that the prepared foams could be potentially used to separate CO_2 in methane-rich gases (see Figures 18c and d).

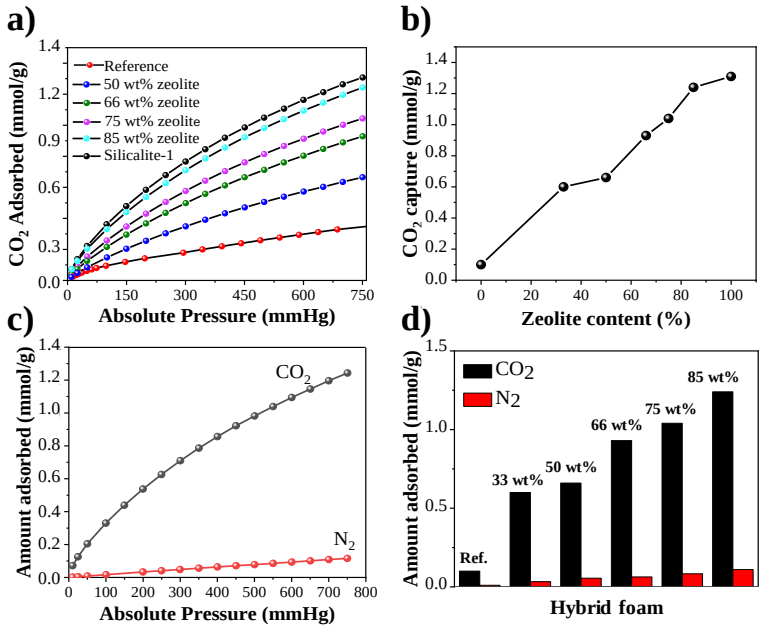

Figure 18. *CO_2 adsorptive properties of hybrid foams. (a) CO_2 adsorption isotherm of hybrid foams; (b) CO_2 capture capacity of hybrid foams as a function of zeolite content; (c) comparison between adsorption of CO_2 and N_2 showing the high selectivity for CO_2 in the foam consisting of 85 wt.-% silicalite-1; and (d) final amount of CO_2 and N_2 adsorbed at 1 bar absolute pressure for different foams.*

The reusability is an important feature that sorbent materials need to have towards CO_2 capture or any other gas sorption. Thus, the reusability capacity was investigated by gravimetric adsorption measurements. In brief, the foams were placed in a gravimetric balance and subject to repeated CO_2/N_2 adsorption/desorption cycles, where the weight-% change was monitored. The cyclability is shown in Figure 19. The reusability of the foams seems to be very high since only a minor decrease in adsorption capacity could be observed after 6 cycles or even after 20 cycles, the reduction was around only 9% (not shown here). The selectivity linearly increases as a function of zeolite content, attributed to the higher adsorption affinity of silicalite-1 for CO_2 molecules compared to N_2.

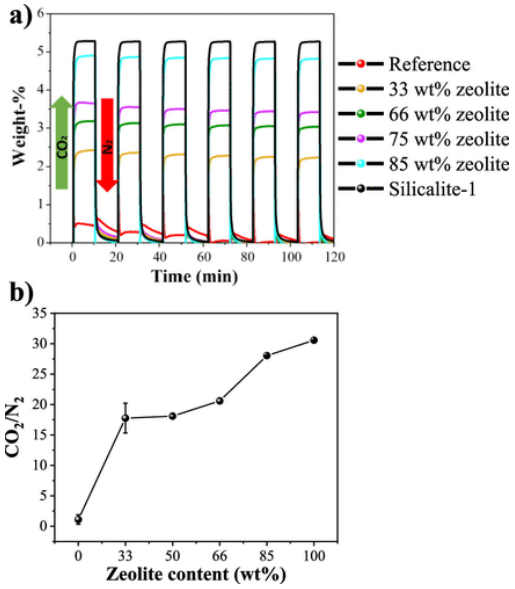

***Figure 19**.Gravimetric gas adsorption measurements of the hybrid foams: (a) cycles of CO_2/N_2 adsorption of hybrid foams measured by TGA and (b) apparent selectivity of foams as a function of zeolite content in the foams.*

7. Synthesis, characterization and evaluation of Fe-N-doped ordered mesoporous carbons as fuel cell catalysts

As presented in Chapter 3, currently, there is a continuous relentless search for platinum-free catalysts for fuel cell technology. One of the most promising non-precious metal catalyst classes is self-supported transition metal nitrogen-doped carbon materials, which have shown good electrocatalytic activity for ORR in alkaline media. These materials have been prepared from different sources such as porphyrines, phtalocyanines and phenanotroline, among others. However, their cost, low stability, poor catalytic activity in acidic media are some of the disadvantages.

Recently, transition metal- and nitrogen-doped OMCs were prepared by impregnating a transition metal salt (*i.e.,* Fe or Co), and a nitrogen and carbon precursor into an ordered-mesoporous silica template (*i.e.* KIT-6) that was subsequently pyrolyzed at high temperatures, resulting in a material, which exhibited good results in terms of stability in acidic media and PEMFC performance, as well as offering a cheaper synthesis alternative. Since then, several variables have been investigated in order to optimize the synthesis and improve the catalytic activity in PEMFC performance. Pyrolysis temperature, carbon-nitrogen precursor, transition-metal salts and their degree of hydration, and template-removal procedures, are some of the synthesis parameters evaluated.[185,186,188]

In Paper 5, we investigated the effect of the counter anion of the transition-metal salt, in this case iron, on the synthesis of Fe-N-doped OMC catalysts. The counter ion can presumably influence the resultant transition the metal OMC in two aspects: the solubility of the salt in carbon-nitrogen precursor used and the simultaneous incorporation of additional dopants. The high solubility of the iron salt in the precursor is, therefore, expected to increase the iron loading in the catalyst, which could also increase the number of active sites in the final Fe-N-doped OMC.

7.1 Synthesis and characterization of Fe-N-doped OMC catalysts

The standard synthesis method used in this thesis is as follows: ordered mesoporous silica KIT-6 template is synthesized, furfurylamine (FA) and iron salt are mixed and impregnated in the template, followed by ageing, first heating at 100 ºC for 2 h and second heating at 160 ºC for 2 h, first pyrolysis treatment from room temperature to 950 ºC at 15 ºC/min and hold at 950 ºC for 4 h, repeat impregnation, ageing, heating cycles, and pyrolysis at 950 ºC for 6 h, silica

template removal with HF at room temperature, sulfuric acid treatment for 6 h, and finally pyrolysis at 950 ºC.

Prior to the synthesis of Fe-N-doped OMCs, the solubility of four different salts in furfurylamine, which is the carbon-nitrogen precursor, was investigated. Iron (III) chloride hexahydrate ($FeCl_3 \cdot 6H_2O$) was used as reference of previous studies, and the other salts studied were iron(II) tetrafluoroborate hexahydrate ($Fe(BF_4)_2$-$6H_2O$), iron(II) trifluoromethanesulfonate ($Fe(OTf)_2$) and iron(II) acetate ($Fe(OAc)_2$). In Table 8, the solubilities of the Fe-salts in FA are summarized.

***Table 8**. Relative solubility of iron salts in furfurylamine*

Fe salt	**Approximate saturation limit**	
	g/L	mol/L
$FeCl_3$-$6H_2O$	60	0.22
$Fe(BF_4)_2$-$6H_2O$	430	1.27
$Fe(OTf)_2$	440	1.24
$Fe(OAc)_2$	300	1.72

To distinguish the iron salts and their respective Fe-N-doped OMC, the samples are designated by their counter anion; for example, the resultant Fe-N-doped OMC from $Fe(OAc)_2$ salt is denoted OAc-Fe-OMC. The solubility of iron salts was increased in the three salts in comparison with the solubility of $FeCl_3$-$6H_2O$, demonstrating that the counter anion plays a significant role in the solubility of the iron salts in FA. For the synthesis of Fe-N-OMCs, the iron loading was noticeably increased solely for OTf-Fe-OMC, despite all salts showing an increase in the solubility in comparison to the reference $FeCl_3 \cdot 6H_2O$ salt (see Table 9). On the other hand, OAc-Fe-OMC exhibited the lowest Fe loading, despite that its precursor iron salt has a 5 times higher solubility in FA than the reference Fe salt.

***Table 9**. Elemental and thermogravimetric analysis for Fe-OMCs.*

Sample	**H_2O[#] (hydration)**	**H***	**C***	**N***	**S***	**Fe[§]**	**Other non-volatiles[§,#]**
Cl-Fe-OMC	3.22	1.00	83.42	3.68	0.11	0.40	0.52
OAc-Fe-OMC	0.45	0.58	93.21	0.92	0.20	0.11	0.21
OTf-Fe-OMC	2.31	1.08	79.97	3.05	2.73	3.88	0.78
BF_4-Fe-OMC	3.03	0.71	85.83	4.23	0.27	0.46	3.52

Determined by TGA
* Determined by EA
§ Determined by XRF

Thus, it is evident that the solubilities of the iron salts are not directly related to the resulting iron loading in the formed Fe-N-doped OMCs.

Further characterization studies using XRD, nitrogen-sorption and SAXS were conducted in order to understand and gain insight to the effect of the counter anion on the textural properties and structure of Fe-N-doped OMCs. From the nitrogen-adsorption measurements and analysis, it is observed that the specific surface area is significantly higher for Cl-Fe-OMC in comparison with the other Fe-OMCs (see Table 10), indicating that the change in the counter anion might have a negative effect on the formation of the Fe-OMCs during the carbonization and therefore affecting the surface area. Additionally, all samples showed different pore diameters with differently broad pore-size distributions as shown in Figure 20a. It is noticeable that Cl-Fe-OMC has a narrower pore size distribution compared to the other samples and OAc-Fe-OMC has the smallest pore size and broadest pore-size distribution.

Table 10.*Surface properties of the Fe-doped OMCs*

Sample	**BET surface area** **($m^2\ g^{-1}$)**	**BJH pore volume** **($cm^3\ g^{-1}$)***	**Pore diameter maximum** **(Å)***
Cl-Fe-OMC	1035	1.29	41
OAc-Fe-OMC	607	1.26	25
OTf-Fe-OMC	709	1.02	52
BF4-Fe-OMC	572	1.19	60

The SAXS patterns for all four samples are shown in Figure 20b The samples Cl-Fe-OMC OTf-Fe-OMC and BF_4-Fe-OMC show the typical patterns of cubic *Ia3d* structure with the typical (211) and (220) reflections for a rod-type nanostructure, as a result of the nanocasting on KIT-6.[227] This result is in agreement with the obtained BET surface area, pore volume and type of pore-size distribution typical for rod-type structures. In contrast, OAc-Fe-OMC exhibits a very weak reflection, indicating lack of meso-order, which is agreement with the broad pore-size distribution.

In addition, the XRD pattern of OAc-Fe-OMC (see Figure 20c) evidences a high degree of graphitization in comparison to the other samples. This is observed with the high intensity of the typical peaks for amorphous carbon at 26º and 43º, corresponding to reflections (002) and (101) and the graphitic peak at 54º.[186,228] This indicates that the acetate anion facilitates the graphitization process and the presence of iron could catalyze it. Because graphitization is known to remove heteroatoms from the carbon framework, the low iron and nitrogen loadings and high carbon content in OAc-Fe-OMC is consistent with its more graphitic structure. Graphitization could also impact strongly the meso-structure and ordered porosity of the

material and this is clearly evidenced by its weak SAXS pattern and broad pore diameter distributions.

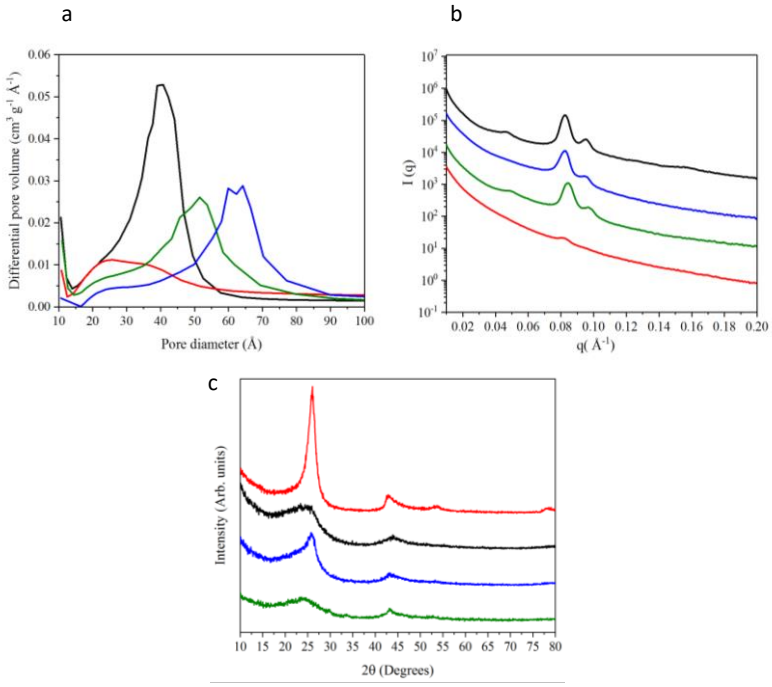

***Figure 20**. Pore diameter distributions based on the adsorption isotherm (a), SAXS plots (SAXS)(b), and X-ray diffractograms (c) for Cl-Fe-OMC (black), OAc-Fe-OMC (red), OTf-Fe-OMC (green), and BF4-Fe-OMC (blue).*

7.2 Electrocatalytic evaluation of Fe-N-doped OMCs

In the previous section, the effect of the counter anion of Fe salts on the structural properties of synthesized Fe-N-doped OMCs was described and discussed. In this chapter, we establish a relationship between the material properties and the catalytic properties. The electrocatalytic activity towards ORR is investigated by means of RDE and the electrochemical performance conducting PEMFC tests.

The evaluation of the electrocatalytic activity of the Fe-N-doped carbons towards ORR provided information of the kinetics and reaction mechanisms of these materials. Such evaluation was carried out in RDE cell under acidic conditions using a O_2-saturated $HClO_4$ electrolyte in order to mimic the PEMFC acidic conditions and the results are shown in Figure 21.

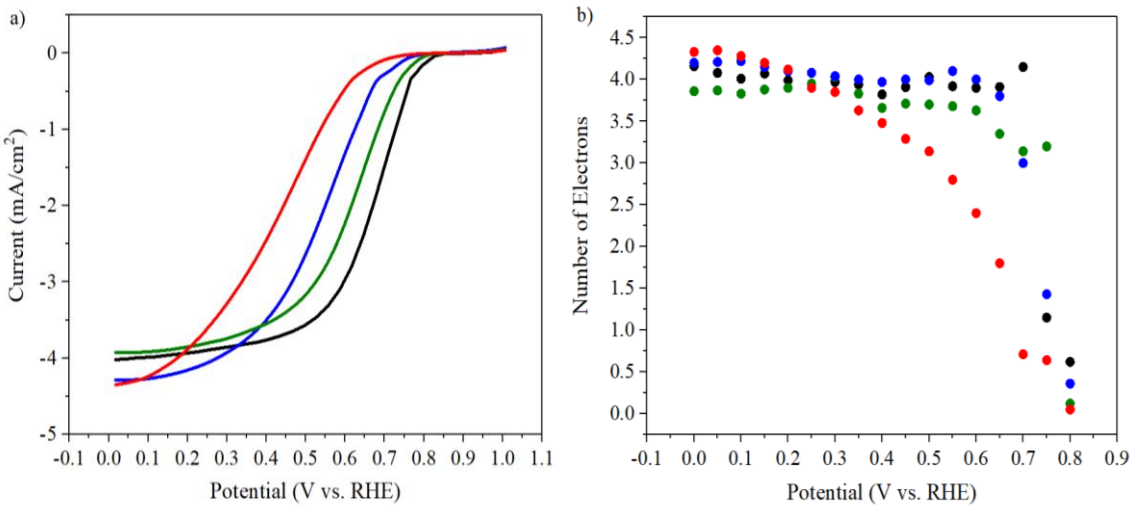

***Figure 21**.a) Rotating Disk Electrode (RDE) polarization plots collected in O2-saturated 0.1 M HClO4 electrolyte with a rotation rate of 900 rpm at room temperature and b) number of electrons transferred for the Fe-N-doped OMC catalysts as determined by the Koutecky-Levich equation for Cl-Fe-OMC (black), OAc-Fe-OMC (red), OTf-Fe-OMC (green), and BF4-Fe-OMC (blue).*

Cl-Fe-OMC shows the highest half-wave potential ($E_{1/2}$) at 0.68 V vs. RHE with OTf-Fe-OMC and BF_4-Fe-OMC slightly lower at 0.62 V and 0.56 V, respectively. OAc-Fe-OMC performs much worse with an $E_{1/2}$ of 0.44 V. The number of transferred electrons was determined by the Koutecky-Levich equation and are shown in Figure 21b. Based on this calculation, Cl-Fe-OMC, BF4-Fe-OMC, and OTf-Fe-OMC follow a four-electron mechanism from 0 to ca. 0.60 V, indicating that the oxygen can be completely reduced to water. In contrast, for OAc-Fe-OMC, the number of electrons is significantly reduced from 0.3 V up to 0.7 V where the number of electrons is one, indicating that the reaction is not a four-electron transfer process.

The poor catalytic activity towards ORR of OAc-Fe-OMC and poor electron transfer can be attributed to many factors observed in the previous chapter: i) low Fe and N contents, which are the main components in the formation of the catalytic active sites;[185,230] ii) broad pore-size distribution, less ordered mesoporosity and relatively low surface area. The ORR catalytic activity for OTf-Fe-OMC, which contains significantly higher Fe loading, shows an improvement, in comparison with BF_4-Fe-OMC and OAc-Fe-OMC, but not better than Cl-Fe-OMC. Certainly, this behavior suggests the incorporation of high loading of Fe in the Fe-N-doped OMC material does not imply that the catalytic activity will be enhanced, since the catalytic activity is strongly limited by the number of active sites. This indicates that not all the incorporated iron is transformed into catalytic active sites.

Further, the polarization plots from the PEMFC electrochemical tests are shown in Figure 22. At the low current region, a similar behavior compared to the RDE results is observed, where the Cl-Fe-OMC shows better performance than the other three Fe-N-doped OMC samples. On the other hand, at high current density region, BF4-Fe-OMC and OTf-Fe-OMC slightly outperform Cl-Fe-OMC. Comparing the properties of BF4-Fe-OMC and Cl-Fe-OMC , it is observed that both have similar iron content, hydration, nitrogen content and hydrogen content. However, one could also interpret this as slight outperformance of BF4-Fe-OMC at high

currents is a result of the degree of graphitization, which seems to be higher and the presence of boron, which could be acting as dopant and take part in the ORR.

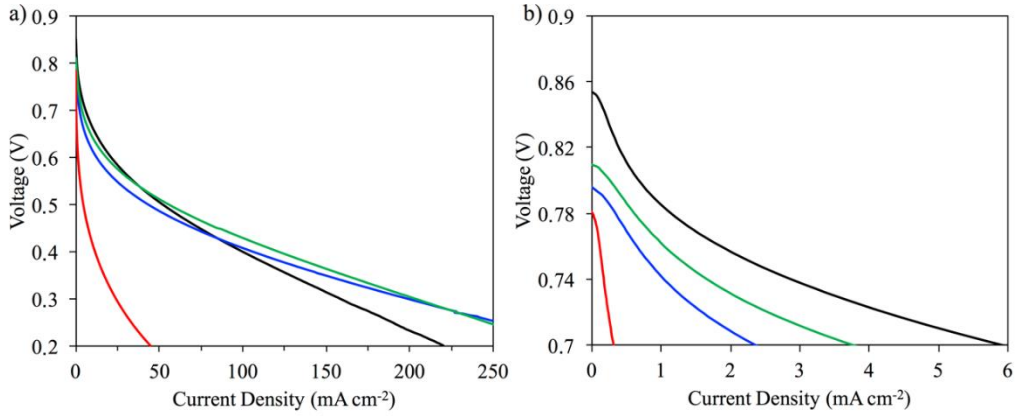

Figure 22. *a) Polarization curves and b) zoom in of low current density regions measured in a single cell PEM fuel cell for Fe-OMCs. Cl-Fe-OMC (black), OAc-Fe-OMC (red), OTf-Fe-OMC (green), and BF4-Fe-OMC (blue).*

Despite of the higher Fe loading in the OTf-Fe-OMC sample, it does not perform noticeably better than the BF4-Fe-OMC and control Cl-Fe-OMC samples. Again, this confirms that the iron incorporated in the sample consist of less active species in comparison to the iron species found in BF4-Fe-OMC and Cl-Fe-OMC. Overall, the electrocatalytic performance of OTf-Fe-OMC, BF4-Fe-OMC and Cl-Fe-OMC is rather similar, indicating that despite the high solubility of their iron salts in FA and noticeably higher loading of iron in OTf-Fe-OMC, the number of catalytic active sites seems to be fairly similar.

The low catalytic activity of OAc-Fe-OMC was observed along the current range in the polarization plot, confirming the results determined by RDE measurements. As mentioned above, this indicates that the low Fe and N contents, have an effect on the formation of active sites. In addition, its lack of order and irregular porous structure could prevent the diffusion of reactants and products within the Fe-OMC structure, further lowering its ORR activity.

8. Catalyst activation protocols for Fe-N-doped OMC catalysts

Over the last decades many efforts have been devoted to optimizing the membrane electrode assemblies (MEAs) and operation conditions of the PEMFC in order to improve their performance and durability. Among the operating conditions, the MEA activation is a procedure that typically has critical influence on the efficiency and long-term performance.[231,232] The activation protocol directly affects: the hydration of the polymer membrane and catalyst, removal of contaminants from the catalyst and electrode, generation of pathways for the reactants, and reaching a stable performance after the activation step. Many of the reported *in-situ* activation protocols are divided in two main groups: constant-potential and constant-low-current procedures. Besides, most of these protocols have been developed and implemented for the activation of platinum-based catalysts. The obtained activity results, post-activation procedure, have shown significant improvement of the catalyst activity but the times required to carry out such protocols vary from 2 to 100 hours, and this has a negative implication for the mass production of PEMFC, where even short activation times can cause production delays.

Although Fe-N-doped porous carbon materials have emerged as the most promising alternative to replace platinum-based catalysts, challenges in the low performance and durability in fuel cells still need to be addressed.[233,234] As investigated for platinum-based catalysts, the activation protocols have shown an improved catalytic activity in PEMFC. In this thesis we present for the first time a comparative study of break-in or activation protocols for Fe-N-doped OMC catalysts as outlined in Table 11, and their catalytic activity for ORR in PEMFC.

A large number of 5 cm^2 MEAs were manufactured using the same catalyst ink batch and deposition procedure and the activation protocols were performed on a different individual MEA sample for each evaluated protocol. All the MEAs have the same low content of Fe-N-doped OMC catalysts (*i.e.* 1.2 mg cm^{-2}) explaining the comparably low catalytic conversion efficiency. The Fe-N-doped OMC material was prepared following the synthesis procedure using $FeCl_3 \cdot 6H_2O$ salt as presented in Paper 5. The experiments were carried out using the same fuel cell (5 cm^2 TP5 Research cell, GreenLight Innovation), at 80 °C, 100 % RH and back.pressure of 2 bar. All the activated MEAs exhibited a stable, constant current after 1 h.

Table 11. *Protocols evaluated for activation of Fe-N-doped OMC in PEMFC performance tests.*

Activation	Description	Note
No activation	Increase temperature up to 80 °C under H_2/Air	Polarization plot is measured after desired temperature is reached
Potential holding @ 0.3 V	Increase temperature to 80 °C under H_2/Air with 0.3 V potential holding	Polarization plot is measured after a stable current is reached
Potential holding @ 0.4 V	Increase temperature to 80 °C under H_2/Air with 0.4 V potential holding	Polarization plot is measured after a stable current is reached
Potential holding @ 0.5 V	Increase temperature to 80 °C under H_2/Air with 0.5 V potential holding	Polarization plot is measured after a stable current is reached
Square wave potential loop 0.3 - 0.6 V	Increase temperature to 80 °C under H_2/Air with cycles of 0.3 V for 15 min → 0.6 V for 15 min → 0.3 V for 15 min	Polarization plot is measured after a stable current is reached no significant change in current is observed for two successive equal potentials
Stepwise potential loop	Increase temperature to 80 °C under H_2/Air with 0.3 – 0.8 V – 0.3 V by 0.1 V step with 5 min holding	Polarization plot is measured after the loop is completed

Figure 23 shows the polarization curves under H_2/air and H_2/O_2, respectively comparing the influence of the preceding activation protocols. Overall, no major difference is observed in the catalytic performance under H_2/air condition between the different catalyst activation protocols. On the other hand, a more noticeable difference is observed under H_2/O_2 conditions, wherein the 0.3V-holding activated catalyst shows somewhat better performance along the current range compared to non-activated and 0.4V- and 0.5V-holding activated catalysts. In addition, the square wave potential protocol seems to give the best performance of all samples at the highest current densities. However, the differences are still comparably small between the samples and statistical significance should be confirmed before firm conclusions are drawn from these results.

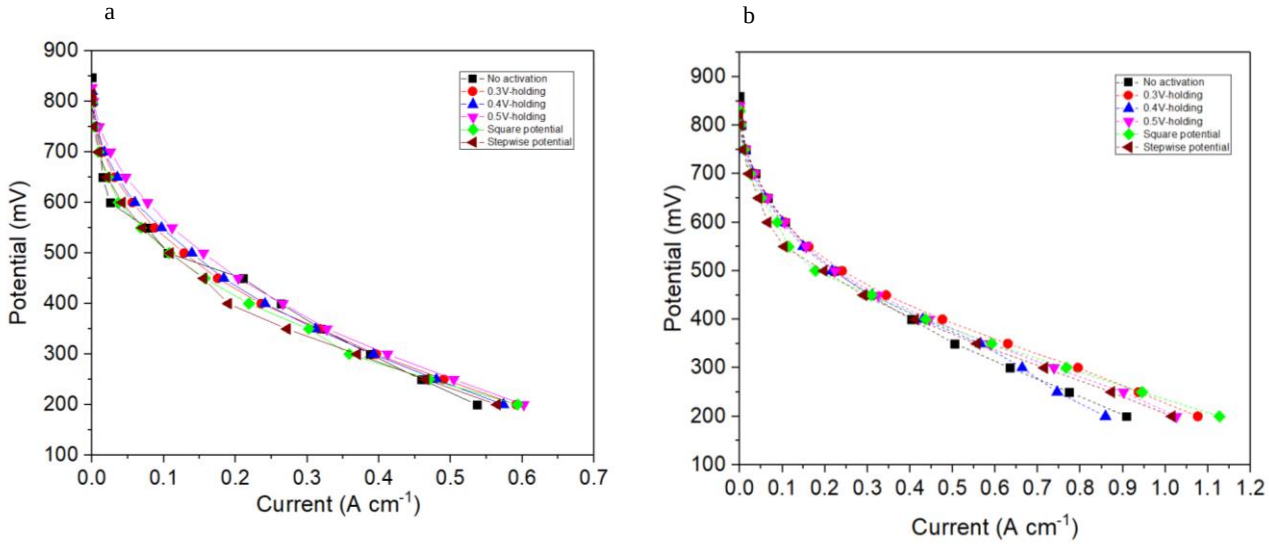

Figure 23. *Polarization plots of activated MEAs by different activation protocols run with a) H_2/air and b) H_2/O_2.*

Three additional activation protocols were evaluated to understand the influence of the pre-heating step and the effect of the gas composition during the activation. The protocols are outlined in Table 12. The polarization curves for the activated catalysts under H_2/air and H_2/O_2 are shown in Figure 24. A significant improvement in performance compared to the best previous protocol of the 0.3V activated sample was found for the activation protocols preheated-N_2 activated and preheated without gases, whereas the 0.3V-holding-O_2 activated catalysts was found to perform worse than the 0.3V activated under H_2/air conditions. The improved performance of the first two samples shows the importance of evaluating activation protocols as their performance at 0.5 V is around 50-70% higher than the previously best protocol. It thus appears beneficial to avoid flow of current through the MEA before the sample has been heat treated and even more beneficial to flush the fuel cell with nitrogen during this heating before operating the fuel cell. The detailed mechanism for this improvement remains to be completely understood.

Table 12. *Protocols evaluated for activation of Fe-N-doped OMC in PEMFC performance tests.*

Activation	Description	Note
Preheating with N_2	1. Increase temperature to 80 °C under N_2/N_2 condition 2. Change to H_2/air after the temperature reaches 80 °C 3. Voltage holding at 0.3 V under H_2/air condition	Polarization plot is measured after a stable current is reached
Preheating with no gases	1. Increase temperature to 80 °C without gas flowing 2. Change to H_2/air after the temperature reaches 80 °C 3. Voltage holding at 0.3 V under H_2/air condition	Polarization plot is measured after a stable current is reached
Potential holding @ 0.3 V-O_2	Increase temperature to 80 °C under H_2/O_2 with 0.3 V potential holding	Polarization plot is measured after a stable current is reached

The lower catalytic performance of the 0.3V-holding-O_2 activated catalyst may be related to accelerated oxidation of the catalyst due to presence of pure oxygen. It is known for other Fe containing catalysts that such oxidation can be caused by corrosion of the carbon matrix and destruction of the F-N moieties due to the presence of peroxide radicals formed through the Fenton reaction that is catalyzed by Fe.[233] However, this mechanism for the Fe-N-OMC catalyst remains to be confirmed.

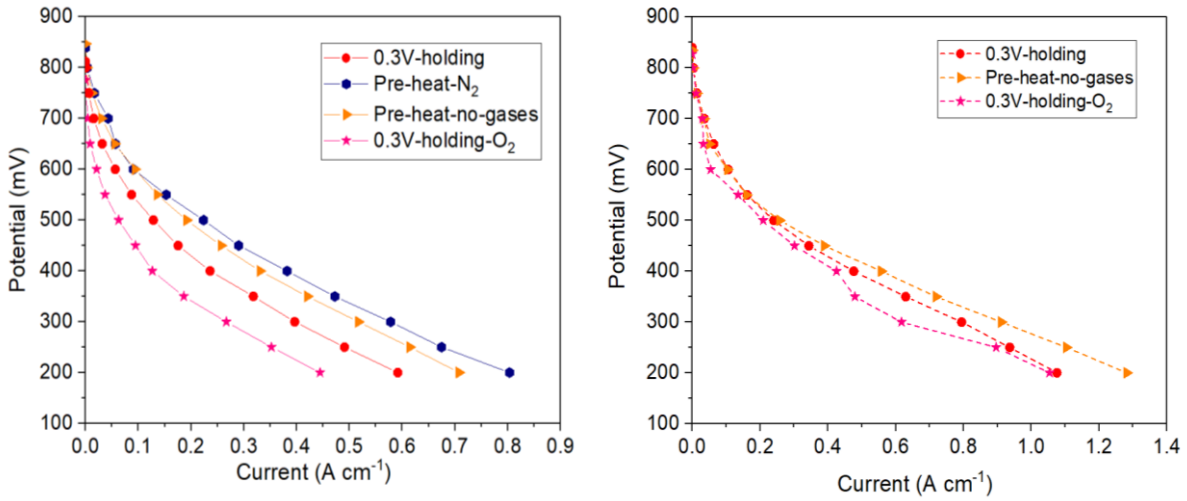

Figure 24. *Polarization plots of activated MEAs by different activation protocols run with a) H_2/air and b) H_2/O_2.*

Although the type of gas condition in the pre-heating step seems to influence the catalytic performance of the MEAs after the activation, it seems not to maintain this higher performance for more than a short period of around 40 hours in durability tests under H_2/air at 0.4 V constant potential as shown in Figure 25. At the beginning of the durability test, the activated catalysts show starting currents following the trend in Figure 24 but thereafter the current decreases to around 0.3 A after 36 hours of test for the three activated catalysts. This suggests that the activation protocol needs to be complemented by suitable operating conditions to preserve the long-term performance of the catalyst. The performance degradation decay is on average 55 % for the three activated catalysts within the 40 hours durability test. Likewise, the durability tests for the activated catalysts by the activation protocols in Table 11 exhibited 50 %-degradation decay (not shown here).

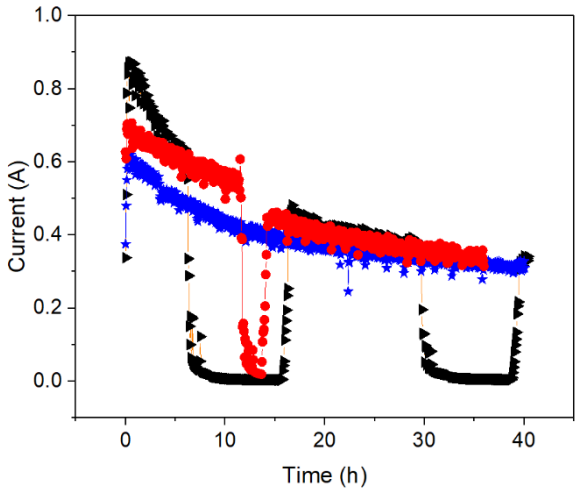

Figure 25*. Stability test measured at 0.4 V under H_2/air condition for activated Fe-N-doped OMC catalysts with activation protocols: preheating N_2 (black triangles), preheating with no gases (red circles) and potential holding at 0.3 V under H_2/O_2 (blue stars).*

From the results presented above, it can be concluded that from the investigated activation protocols in PEMFC, the pre-heating step under different gas conditions influences the performance in the short-term to a large extent, but the advantage is lost during durability tests. This indicates that the Fe-N-doped OMC catalysts requires a different and simpler activation protocol compared to platinum-based catalysts. Certainly, this could bring an economical benefit for mass production of PEMFC, simplifying the catalyst activation step. However, the large degradation decay observed for all the activated MEAs, needs to be better understood and prevented in order to meet long term performance requirements in applications.

9. Conclusions & Outlook

This thesis was divided into two main groups of porous materials: zeolites and mesoporous carbons. Synthesis and characterization of these materials were crucial parts to understand the formation and properties for different applications. The studies, thereby, contributed to gain fundamental knowledge about the formation and tailoring the properties of these materials, their processability into mesoporous and/or hierarchical structures and finally their use in applications towards solutions of global environmental challenges of CO_2 sequestration and energy conversion.

The synthesis of colloidal zeolite particles was used as a basis to monitor the formation of the zeolite crystals. We have determined and quantified the influence of the chemical solution equilibria on the zeolite formation and provide explanation for the premature termination of zeolite growth prior full conversion. By adjusting the pH of the synthesis mixture at this equilibrium, either a condensation (acid adjustment) or dissolution (alkaline adjustment) reactions could be favored. This control has a critical impact on the growth rate, yield and particle size. Likewise, the synthesis of colloidal ZSM-5 particles also followed the chemical equilibria growth model, evidencing the broad applicability of the mechanism. Besides, it was found that by lowering the pH, not only the increase in particle size and yield was achieved but also an improved incorporation of aluminum into the framework was favored.

Two preparation methods using colloidal zeolite particles were introduced. A hybrid zeolite-cellulose/gelatin foam was prepared by using colloidal zeolite particles and nanocellulose fibers in a straightforward synthetic method. The foams exhibited high-loadings of zeolite particles, without the need of using any type of binders or cross-linkers due to the robust structure generated by the nanocellulose fibers and the gelatin that could act as support for the zeolites. The CO_2 sorption capacity of these foams showed a linear trend with respect to zeolite content, evidencing that the organic matrix acts as a support and does not interfere with the sorption process. In addition, a novel colloidal assembly method was developed to prepare perfectly spherical mesoporous zeolite microparticles without employing any mesoporous template. The materials exhibited great pore interconnectivity and high pore volumes. The synthetic strategy has preparation time and temperature conditions that are lower than the previously reported methods, which can have great implications in the production of hierarchical zeolites at the industrial scale. Besides, this new approach opens the possibility of combining nanoparticles sols with differences in particle size and chemical composition and thus to create multifunctional materials towards separation, catalysis or sensing applications. A remaining study for the future is the evaluation of the mechanical properties of these mesoporous zeolites and investigation about their implementation in catalytic reactions and separation processes.

During the synthesis of Fe-N-doped OMC materials for fuel cell catalysts, it was found that the effect of the counter anion of the iron salts, could have a great impact on their solubility in the

carbon-nitrogen precursor solution but this increase in iron was not reflected in the iron content in the resultant Fe-N-doped materials. Besides, it was proven that the change of the iron salt affected some of the structural and catalytic properties of the materials. Special attention was casted on one Fe-N-doped OMC that exhibited significantly higher iron loading compared to the other samples, observing that the high iron content did not show noticeable improvement compared to a Fe-OMC containing Fe. This suggests that most of the incorporated iron species could presumably be inactive or less active towards ORR. A coming step will be to optimize the use of iron salts under different synthesis conditions *e.g.*, temperature, precursor/iron ratio, template-removal strategy, in an effort to take advantage of the high solubility and incorporate more iron as more active species.

Despite the implementation of activation catalyst protocols do not show a large influence on the Fe-N-doped OMC catalyst in PEMFC at long-term performance, it is instead crucial to thoroughly investigate the reasons of the degradation decay in their stability and how to overcome it in order to meet the performance demand needed in fuel cell applications.

10. Acknowledgements

This project was financed by the European Union's Horizon 2020, Research and innovation program under the grant no. 676045-MULTIMAT.

This work would not be possible without the support and help of many people in my surrounding. I would like to take this opportunity to express my sincere gratitude to these people during this journey.

First of all, I would like to thank, Anders Palmqvist, my supervisor, for giving me the opportunity to join the group at Chalmers in 2016 and mentoring me throughout my PhD studies. I think I have not regretted at all to have left the PhD position opportunity in Oulu and come to Sweden. Thank you for trusting me in taking part in many projects, study visits and conferences in which I have learnt a lot from. Your feedback and support in moments of need and desperation was highly valuable. It was great to work with you and achieve so many things.

Magnus Skoglundh, my examiner, thank you for your feedback and help during my studies.

My former colleagues Samuel, Caroline and Johanna, thank you for teaching me so much about fuel cells, carbon synthesis and other important techniques. Caroline, the times we were spending in the lab were unique and enriching both professionally and personally. Sam, amigo gringo, ché! fue un placer conocerte y haber podido escribir un muy buen trabajo juntos.

Luis and Remco, co-authors and MULTIMAT buddies, thank you for the excellent work we have done together. Thank you for the constant discussions, amazing trips and unforgettable beers. You are awesome my friends!

Tae-Hyun, thank you for the support in fuel cell tests, I have learnt a lot from you.

Tim, your research visit in Sweden was very short but very enriching. I want to thank you for all you have taught me about RDE, fuel cells and porous carbons and obviously the nice beers we had. A pity we could not write the paper together.

My research group and former group members, Giulio, Yifei, Milene, Gunnar, Joakim, Sam, Tae-Hyun, Sanna, Caroline, Johanna, Andrey. Thank you for all your support and all the nice moments we shared both inside and outside Chalmers.

My MULTIMAT buddies, Paula, Pallabi, Deniz, Gerardo, Peter, Hang Long, Luis, Remco, Xufeng, Massimiliano and Xiaobin, thank you for all the great memories and adventures during our meetings and courses. Xufi, thank you for helping me in Konstanz. You are the craziest Chinese ever. I would like to thank Prof. Helmut Cölfen at Konstanz University, to have received me in his group for my study visit

Prof. Dongyuan Zhao at Fudan University and his group members, thank you for receiving me in Shanghai and share the knowledge in the synthesis of mesoporous carbons. It was an amazing experience.

Gustav, the best office mate I could have ever had. Thank you for all your help from day 1 in Chalmers. You have been always there when I have needed, that is something I won´t forget. Thank you for joining me in all the racket sports possible and I still feel sorry when you broke your wrist playing tennis.

All the people at Applied Chemistry, thank you for the nice fikas, talks, and memorable moments. Frida, Lotta, Carina, Kristina, and Sara thank for your relentless work in backstage to make all this possible.

My friends Jessica, Maja and Ivan, thank you for taking time to read my thesis and give me constructive feedback.

My friends in Gothenburg, Santiago, Ricardo, Ivan, Maja, Jenifer, Luis, Eva, Oscar, Maria, Melissa, Simon, Dominic, Judith, Renesteban, Ivonne, Angelica, Alejandro, Eirini, Alessandro and Karin. I am very glad to have met you during this journey and more important all your support during my stay in Gothenburg. Nice moments, beers, parties, trips, concerts, and tennis and padel matches.

Eva Jimenez, muchas gracias por todo tu apoyo incondicional en casa, me has tratado como a uno mas de tu familia. Ha sido todo un placer conocerte y ojala sigas siendo parte de mi vida en Suecia.

My friends around the world, Leo, Felipe, Pilar, Mache, Kevin, Adriana, Tota, Fabio, Arley, Carlos, Jose, Mauricio, thank for always being curious about my work and my well-being in Sweden.

Mi madre Luz Marina, gracias por siempre creer en mi, por empujarme a ser un mejor profesional a pesar de que como consecuencia la distancia nos separara Gracias por todas tus oraciones, comprension, amor, sacrificios y entrega. Gracias por ser la mejor mamá del mundo!

Sanna, je n'ai pas les mots pour te remercier pour tout ton soutien et ta compréhension, surtout dans la dernière partie de ma thèse. Ton amour et ta patience ont beaucoup compté pour moi. J'ai beaucoup de chance que nos chemins se sont croisés.

11. Abbreviations

AFM – Atomic Force Microscopy
BCC – Body Centered Cubic
BET - Brunauer-Emmet-Teller
BJH - Barrett–Joyner–Halenda
CCS - Carbon Capture and Storage
DLS - Dynamic Light Scattering
EDS - Energy-Dispersive Spectroscopy
EISA - Evaporation-Induced Self-Assembly
EM – Electron Microscopy
FCC – Face Centered Cubic
FTIR – Fourier-Transform InfraRed
HC1 – Hydrochloric Acid
HOR- Hydrogen Oxidation Reaction
HRTEM – High-resolution transmission electron microscopy
MOFs - Metal Organic Framework
MZM – Mesoporous Zeolite Microsphere
MZSM - Mesoporous Zeolite/Silica Microsphere
NMR - Nuclear Magnetic Resonance
NNLS - Non-Negatively Least Squares
OMC - Ordered Mesoporous Carbons
ORR - Oxygen Reduction Reaction
PAN- Polyacrylonitrile
PDADMAC - Polydiallyldimethylammonium chloride
PEMFC - Proton Exchange Membrane Fuel Cells
SAC - Steam-Assisted Crystallization
SEM – Scanning Electron Microscopy
TEAOH - Tetrathylammonium Hydroxide
TEMPO – 2,2,6,6-tetramethylpiperidine-1-oxyl radical
TEOS –Tetrathylorthosilicate
TGA - Thermogravimetric Analysis
TOCNF – Tempo Oxidized Cellulose Nanofiber
TPAOH -Tetraprpylammonium hydroxide
TS-1 - Titanium Silicalite-1
XRD – X-Ray Diffraction
W/O - Water-in-Oil
ZIF-L - Zeolitic Imidazolate Frameworks
SiO_2–Silica
Al_2O_3 - Alumina

12. References

1. Thommes, M. *et al.* Physisorption of gases, with special reference to the evaluation of surface area and pore size distribution (IUPAC Technical Report). *Pure and Applied Chemistry* **87**, 1051–1069 (2015).
2. Cundy, C. S. & Cox, P. A. The hydrothermal synthesis of zeolites: Precursors, intermediates and reaction mechanism. *Microporous and Mesoporous Materials* **82**, 1–78 (2005).
3. Li, Y. & Yu, J. New Stories of Zeolite Structures: Their Descriptions, Determinations, Predictions, and Evaluations. *Chem. Rev.* **114**, 7268–7316 (2014).
4. Li, Y., Li, L. & Yu, J. Applications of Zeolites in Sustainable Chemistry. *Chem* **3**, 928–949 (2017).
5. Primo, A. & Garcia, H. Zeolites as catalysts in oil refining. *Chem. Soc. Rev.* **43**, 7548–7561 (2014).
6. Corma, A. State of the art and future challenges of zeolites as catalysts. *Journal of Catalysis* **216**, 298–312 (2003).
7. Pérez-Ramírez, J., Christensen, C. H., Egeblad, K., Christensen, C. H. & Groen, J. C. Hierarchical zeolites: enhanced utilisation of microporous crystals in catalysis by advances in materials design. *Chem. Soc. Rev.* **37**, 2530–2542 (2008).
8. Wu, L., Li, Y., Fu, Z. & Su, B.-L. Hierarchically structured porous materials: synthesis strategies and applications in energy storage. *Natl Sci Rev* doi:10.1093/nsr/nwaa183.
9. Lavoine, N. & Bergström, L. Nanocellulose-based foams and aerogels: processing, properties, and applications. *J. Mater. Chem. A* **5**, 16105–16117 (2017).
10. Eisa, W. H., Abdelgawad, A. M. & Rojas, O. J. Solid-State Synthesis of Metal Nanoparticles Supported on Cellulose Nanocrystals and Their Catalytic Activity. *ACS Sustainable Chem. Eng.* **6**, 3974–3983 (2018).
11. Borchardt, L. *et al.* Toward a molecular design of porous carbon materials. *Materials Today* **20**, 592–610 (2017).
12. Lee, J., Kim, J. & Hyeon, T. Recent Progress in the Synthesis of Porous Carbon Materials. *Advanced Materials* **18**, 2073–2094 (2006).
13. Reed, M. W. & Brodd, R. J. Porous carbon for fuel cell electrodes. *Carbon* **3**, 241–246 (1965).
14. Rajagopalan, R., Balakrishnan, A. & Balakrishnan, A. *Innovations in Engineered Porous Materials for Energy Generation and Storage Applications*. (CRC Press, 2018). doi:10.1201/9781315184401.
15. Barrer, R. M. 33. Synthesis of a zeolitic mineral with chabazite-like sorptive properties. *J. Chem. Soc.* 127–132 (1948) doi:10.1039/JR9480000127.
16. Barrer, R. M. & Marcilly, C. Hydrothermal chemistry of silicates. Part XV. Synthesis and nature of some salt-bearing aluminosilicates. *J. Chem. Soc. A* 2735–2745 (1970) doi:10.1039/J19700002735.
17. Milton, R. M. Molecular sieve adsorbents. (1959).
18. Milton, R. M. Molecular Sieve Science and Technology. in *Zeolite Synthesis* vol. 398 1–10 (American Chemical Society, 1989).
19. Barrer, R. M. & Denny, P. J. 201. Hydrothermal chemistry of the silicates. Part IX. Nitrogenous aluminosilicates. *J. Chem. Soc.* 971–982 (1961) doi:10.1039/JR9610000971.
20. Kerr, G. T. & Kokotailo, G. T. SODIUM ZEOLITE ZK-4, A NEW SYNTHETIC CRYSTALLINE ALUMINOSILICATE. *J. Am. Chem. Soc.* **83**, 4675–4675 (1961).
21. Kerr, G. T. Chemistry of Crystalline Aluminosilicates. II. The Synthesis and Properties of Zeolite ZK-4. *Inorg. Chem.* **5**, 1537–1539 (1966).
22. Argauer, R. J. & Landolt, G. R. Crystalline zeolite zsm-5 and method of preparing the same. (1972).
23. Wilson, S. T., Lok, B. M., Messina, C. A., Cannan, T. R. & Flanigen, E. M. Aluminophosphate molecular sieves: a new class of microporous crystalline inorganic solids. *J. Am. Chem. Soc.* **104**, 1146–1147 (1982).
24. Anderson, M. W. *et al.* Structure of the microporous titanosilicate ETS-10. *Nature* **367**, 347–351 (1994).
25. Martens, J. A. & Jacobs, P. A. Crystalline Microporous Phosphates: a Family of Versatile Catalysts and Adsorbents. in *Studies in Surface Science and Catalysis* (eds. Jansen, J. C., Stöcker, M., Karge, H. G. & Weitkamp, J.) vol. 85 653–685 (Elsevier, 1994).
26. Persson, A. E., Schoeman, B. J., Sterte, J. & Otterstedt, J.-E. The synthesis of discrete colloidal particles of TPA-silicalite-1. *Zeolites* **14**, 557–567 (1994).
27. Schoeman, B. J., Sterte, J. & Otterstedt, J.-E. Colloidal zeolite suspensions. *Zeolites* **14**, 110–116 (1994).
28. Schoeman, B. J. A spectroscopic study of the initial stage in the crystallization of TPA-silicalite-1 from clear solutions. in *Studies in Surface Science and Catalysis* (eds. Chon, H., Ihm, S.-K. & Uh, Y. S.) vol. 105 647–654 (Elsevier, 1997).
29. Mintova, S., Olson, N. H., Senker, J. & Bein, T. Mechanism of the Transformation of Silica Precursor Solutions into Si-MFI Zeolite. *Angewandte Chemie* **114**, 2670–2673 (2002).
30. Mintova, S., Olson, N. H. & Bein, T. Electron Microscopy Reveals the Nucleation Mechanism of Zeolite Y from Precursor Colloids. *Angewandte Chemie International Edition* **38**, 3201–3204 (1999).
31. Mintova, S., Olson, N. H., Valtchev, V. & Bein, T. Mechanism of Zeolite A Nanocrystal Growth from Colloids at Room Temperature. *Science* **283**, 958–960 (1999).

32. de Moor, P.-P. E. A., Beelen, T. P. M., Komanschek, B. U., Diat, O. & van Santen, R. A. In Situ Investigation of Si-TPA-MFI Crystallization Using (Ultra-) Small- and Wide-Angle X-ray Scattering. *J. Phys. Chem. B* **101**, 11077–11086 (1997).
33. Cundy, C. S. & Cox, P. A. The Hydrothermal Synthesis of Zeolites: History and Development from the Earliest Days to the Present Time. *Chem. Rev.* **103**, 663–702 (2003).
34. Grand, J., Awala, H. & Mintova, S. Mechanism of zeolites crystal growth: new findings and open questions. *CrystEngComm* **18**, 650–664 (2016).
35. ZHDANOV, S. P. Some Problems of Zeolite Crystallization. in *Molecular Sieve Zeolites-I* vol. 101 20–43 (AMERICAN CHEMICAL SOCIETY, 1974).
36. Nicolle, M. A., Di renzo, F., Fajula, F., Espiau, P. & Courieres, T. D. A MICROPOROUS TETRAETHYLAMMONIUM PERMUTITE AS SYNTHESIS INTERMEDIATE OF THE ZEOLITE BETA. in *Proceedings from the Ninth International Zeolite Conference* (eds. von Ballmoos, R., Higgins, J. B. & Treacy, M. M. J.) 313–320 (Butterworth-Heinemann, 1993). doi:10.1016/B978-1-4832-8383-8.50036-2.
37. Subotić, B., Tonejc, A. M., Bagović, D., Čižmek, A. & Antonić, T. Electron diffraction and infrared spectroscopy of amorphous aluminosilicate gels. in *Studies in Surface Science and Catalysis* (eds. Weitkamp, J., Karge, H. G., Pfeifer, H. & Hölderich, W.) vol. 84 259–266 (Elsevier, 1994).
38. Burkett, S. L. & Davis, M. E. Mechanism of Structure Direction in the Synthesis of Si-ZSM-5: An Investigation by Intermolecular 1H-29Si CP MAS NMR. *J. Phys. Chem.* **98**, 4647–4653 (1994).
39. Yang, H., Walton, R. I., Antonijevic, S., Wimperis, S. & Hannon, A. C. Local Order of Amorphous Zeolite Precursors from 29Si{H} CPMAS and 27Al and 23Na MQMAS NMR and Evidence for the Nature of Medium-Range Order from Neutron Diffraction. *J. Phys. Chem. B* **108**, 8208–8217 (2004).
40. Cundy, C. S., Lowe, B. M. & Sinclair, D. M. Direct measurements of the crystal growth rate and nucleation behaviour of silicalite, a zeolitic silica polymorph. *Journal of Crystal Growth* **100**, 189–202 (1990).
41. Barrer, R. M. (Richard M. *Hydrothermal chemistry of zeolites*. (Academic Press, 1982).
42. Čižmek, A., Subotica, B., Kralj, D., Babić-Ivančić, V. & Tonejc, A. The influence of gel properties on the kinetics of crystallization and particulate properties of MFI-type zeolities. I. The influence of time and temperature of gel ageing on the particulate properties of silicalite-1 microcrystals. *Microporous Materials* **12**, 267–280 (1997).
43. Li, Q., Creaser, D. & Sterte, J. The nucleation period for TPA-silicalite-1 crystallization determined by a two-stage varying-temperature synthesis. *Microporous and Mesoporous Materials* **31**, 141–150 (1999).
44. Li, Q., Mihailova, B., Creaser, D. & Sterte, J. The nucleation period for crystallization of colloidal TPA-silicalite-1 with varying silica source. *Microporous and Mesoporous Materials* **40**, 53–62 (2000).
45. Li, Q., Mihailova, B., Creaser, D. & Sterte, J. Aging effects on the nucleation and crystallization kinetics of colloidal TPA-silicalite-1. *Microporous and Mesoporous Materials* **43**, 51–59 (2001).
46. Thompson, R. W. Comments on the autocatalytic nucleation of (Na, TPA)-ZSM-5. *Zeolites* **12**, 837–840 (1992).
47. Gonthier, S., Gora, L., Güray, I. & Thompson, R. W. Further comments on the role of autocatalytic nucleation in hydrothermal zeolite syntheses. *Zeolites* **13**, 414–418 (1993).
48. Nikolakis, V., Vlacho, D. G. & Tsapatsis, M. Modeling of zeolite crystallization: the role of gel microstructure. *Microporous and Mesoporous Materials* **21**, 337–346 (1998).
49. AIELLO, R., BARRER, R. M. & KERR, I. S. Stages of Zeolite Growth from Alkaline Media. in *Molecular Sieve Zeolites-I* vol. 101 44–50 (AMERICAN CHEMICAL SOCIETY, 1974).
50. Nastro, A. & Sand, L. B. Growth of larger crystals of ZSM-5 in the system 4(TPA)2O-38(NH4)2O-x(Li,Na,K)2 O-A12O3-59SiO2-750H2O. *Zeolites* **3**, 57–62 (1983).
51. Lowe, B. M. Synthesis Mechanisms for Zeolites and Molecular Sieves. in *Studies in Surface Science and Catalysis* (eds. Grobet, P. J., Mortier, W. J., Vansant, E. F. & Schulz-Ekloff, G.) vol. 37 1–12 (Elsevier, 1988).
52. Sano, T. *et al.* In-situ observation of crystal growth of zeolite ZSM-5 under steaming conditions by optical microscopy. *Microporous Materials* **1**, 353–357 (1993).
53. Iwasaki, A. *et al.* In situ measurement of crystal growth rate of zeolite. *Zeolites* **15**, 308–314 (1995).
54. Anderson, M. W. Surface microscopy of porous materials. *Current Opinion in Solid State and Materials Science* **5**, 407–415 (2001).
55. Freund, E. F. Mechanism of the crystallization of zeolite x. *Journal of Crystal Growth* **34**, 11–23 (1976).
56. Thompson, R. W. Recent Advances in the Understanding of Zeolite Synthesis. in *Synthesis* vol. 1 1–33 (Springer Berlin Heidelberg, 1998).
57. Schoeman, B. J., Sterte, J. & Otterstedt, J.-E. Analysis of the crystal growth mechanism of TPA-silicalite-1. *Zeolites* **14**, 568–575 (1994).
58. Cundy, C. S., Lowe, B. M. & Sinclair, D. M. Crystallisation of zeolitic molecular sieves: direct measurements of the growth behaviour of single crystals as a function of synthesis conditions. *Faraday Discussions* **95**, 235 (1993).
59. Iwasaki, A., Hirata, M., Kudo, I. & Sano, T. Behavior of the (010) face of silicalite crystal. *Zeolites* **16**, 35–41 (1996).

60. Tavolaro, A. *et al.* Formation of MFI crystalline zeosilites from fluoride-containing silicate gels. *Zeolites* **12**, 756–761 (1992).
61. Mullin, J. W. *Crystallization*. (Elsevier, 2001).
62. Agger, J. R., Hanif, N. & Anderson, M. W. Fundamental Zeolite Crystal Growth Rates from Simulation of Atomic Force Micrographs. *Angewandte Chemie International Edition* **40**, 4065–4067 (2001).
63. Anderson, M. W., Agger, J. R., Hanif, N., Terasaki, O. & Ohsuna, T. Crystal growth in framework materials. *Solid State Sciences* **3**, 809–819 (2001).
64. Schoeman, B. J. A high temperature in situ laser light-scattering study of the initial stage in the crystallization of TPA-silicalite-1. *Zeolites* **18**, 97–105 (1997).
65. Kirschhock, C. E. A., Ravishankar, R., Jacobs, P. A. & Martens, J. A. Aggregation Mechanism of Nanoslabs with Zeolite MFI-Type Structure. *J. Phys. Chem. B* **103**, 11021–11027 (1999).
66. Nikolakis, V., Kokkoli, E., Tirrell, M., Tsapatsis, M. & Vlachos, D. G. Zeolite Growth by Addition of Subcolloidal Particles: Modeling and Experimental Validation. *Chemistry of Materials* **12**, 845–853 (2000).
67. Watson, J. N. *et al.* TPA−Silicalite Crystallization from Homogeneous Solution: Kinetics and Mechanism of Nucleation and Growth. *J. Phys. Chem. B* **101**, 10094–10104 (1997).
68. Erdem-Şenatalar, A. & Thompson, R. W. Observations on clear solution silicalite-1 growth by nanoslabs. *Journal of Colloid and Interface Science* **291**, 396–404 (2005).
69. Kirschhock, C. E. A. *et al.* Identification of Precursor Species in the Formation of MFI Zeolite in the TPAOH−TEOS−H2O System. *J. Phys. Chem. B* **103**, 4965–4971 (1999).
70. Davis, T. M. *et al.* Mechanistic principles of nanoparticle evolution to zeolite crystals. *Nature Materials* **5**, 400–408 (2006).
71. de Moor, P.-P. E. A., Beelen, T. P. M., Komanschek, B. U., Diat, O. & van Santen, R. A. In Situ Investigation of Si-TPA-MFI Crystallization Using (Ultra-) Small- and Wide-Angle X-ray Scattering. *J. Phys. Chem. B* **101**, 11077–11086 (1997).
72. Fedeyko, J. M., Rimer, J. D., Lobo, R. F. & Vlachos, D. G. Spontaneous Formation of Silica Nanoparticles in Basic Solutions of Small Tetraalkylammonium Cations. *J. Phys. Chem. B* **108**, 12271–12275 (2004).
73. Knight, C. T. G. & Kinrade, S. D. Comment on "Identification of Precursor Species in the Formation of MFI Zeolite in the TPAOH−TEOS−H2O System". *J. Phys. Chem. B* **106**, 3329–3332 (2002).
74. Cheng, C.-H. & Shantz, D. F. 29Si NMR Studies of Zeolite Precursor Solutions. *J. Phys. Chem. B* **110**, 313–318 (2006).
75. Kragten, D. D. *et al.* Structure of the Silica Phase Extracted from Silica/(TPA)OH Solutions Containing Nanoparticles. *J. Phys. Chem. B* **107**, 10006–10016 (2003).
76. Schoeman, B. J. Analysis of the nucleation and growth of TPA-silicalite-1 at elevated temperatures with the emphasis on colloidal stability. *Microporous and Mesoporous Materials* **22**, 9–22 (1998).
77. Burkett, S. L. & Davis, M. E. Mechanisms of Structure Direction in the Synthesis of Pure-Silica Zeolites. 1. Synthesis of TPA/Si-ZSM-5. *Chem. Mater.* **7**, 920–928 (1995).
78. Iler, Ralph K. *The Chemistry of Silica: Solubility, Polymerization, Colloid and Surface Properties and Biochemistry of Silica | Wiley*. (Wiley, 1979).
79. Mintova, S., Jaber, M. & Valtchev, V. Nanosized microporous crystals: emerging applications. *Chem. Soc. Rev.* **44**, 7207–7233 (2015).
80. Vogt, E. T. C. & Weckhuysen, B. M. Fluid catalytic cracking: recent developments on the grand old lady of zeolite catalysis. *Chem. Soc. Rev.* **44**, 7342–7370 (2015).
81. Tosheva, L. & Valtchev, V. P. Nanozeolites: Synthesis, Crystallization Mechanism, and Applications. *Chem. Mater.* **17**, 2494–2513 (2005).
82. Chen, L.-H. *et al.* Hierarchically structured zeolites: synthesis, mass transport properties and applications. *J. Mater. Chem.* **22**, 17381–17403 (2012).
83. Hartmann, M. Hierarchical Zeolites: A Proven Strategy to Combine Shape Selectivity with Efficient Mass Transport. *Angewandte Chemie International Edition* **43**, 5880–5882 (2004).
84. Corma, A. From Microporous to Mesoporous Molecular Sieve Materials and Their Use in Catalysis. *Chem. Rev.* **97**, 2373–2420 (1997).
85. Jiang, J., Yu, J. & Corma, A. Extra-Large-Pore Zeolites: Bridging the Gap between Micro and Mesoporous Structures. *Angewandte Chemie International Edition* **49**, 3120–3145 (2010).
86. Tao, Y., Kanoh, H. & Kaneko, K. ZSM-5 Monolith of Uniform Mesoporous Channels. *J. Am. Chem. Soc.* **125**, 6044–6045 (2003).
87. Xin, H. *et al.* Enhanced Catalytic Oxidation by Hierarchically Structured TS-1 Zeolite. *J. Phys. Chem. C* **114**, 6553–6559 (2010).
88. Kustova, M. Yu., Hasselriis, P. & Christensen, C. H. Mesoporous MEL – Type Zeolite Single Crystal Catalysts. *Catalysis Letters* **96**, 205–211 (2004).

89. Jacobsen, C. J. H., Madsen, C., Houzvicka, J., Schmidt, I. & Carlsson, A. Mesoporous Zeolite Single Crystals. *J. Am. Chem. Soc.* **122**, 7116–7117 (2000).
90. Tao, Y., Kanoh, H. & Kaneko, K. Uniform Mesopore-Donated Zeolite Y Using Carbon Aerogel Templating. *J. Phys. Chem. B* **107**, 10974–10976 (2003).
91. Kang, Y. *et al.* Uniform Nanozeolite Microspheres with Large Secondary Pore Architecture. *Chem. Mater.* **18**, 1861–1866 (2006).
92. Shi, Y. *et al.* Zeolite microspheres with hierarchical structures: formation, mechanism and catalytic performance. *J. Mater. Chem.* **21**, 16223–16230 (2011).
93. Wei, Y., Parmentier, T. E., Jong, K. P. de & Zečević, J. Tailoring and visualizing the pore architecture of hierarchical zeolites. *Chem. Soc. Rev.* **44**, 7234–7261 (2015).
94. Yang, X.-Y. *et al.* Hierarchically porous materials: synthesis strategies and structure design. *Chem. Soc. Rev.* **46**, 481–558 (2017).
95. Liu, S. *et al.* Preformed zeolite precursor route for synthesis of mesoporous X zeolite. *Colloids and Surfaces A: Physicochemical and Engineering Aspects* **318**, 269–274 (2008).
96. Wang, L., Zhang, Z., Yin, C., Shan, Z. & Xiao, F.-S. Hierarchical mesoporous zeolites with controllable mesoporosity templated from cationic polymers. *Microporous and Mesoporous Materials* **131**, 58–67 (2010).
97. Xiao, F.-S. *et al.* Catalytic Properties of Hierarchical Mesoporous Zeolites Templated with a Mixture of Small Organic Ammonium Salts and Mesoscale Cationic Polymers. *Angewandte Chemie* **118**, 3162–3165 (2006).
98. Shanbhag, G. V., Choi, M., Kim, J. & Ryoo, R. Mesoporous sodalite: A novel, stable solid catalyst for base-catalyzed organic transformations. *Journal of Catalysis* **264**, 88–92 (2009).
99. Cho, K., Cho, H. S., de Ménorval, L.-C. & Ryoo, R. Generation of Mesoporosity in LTA Zeolites by Organosilane Surfactant for Rapid Molecular Transport in Catalytic Application. *Chem. Mater.* **21**, 5664–5673 (2009).
100. Choi, M. *et al.* Amphiphilic organosilane-directed synthesis of crystalline zeolite with tunable mesoporosity. *Nature Materials* **5**, 718–723 (2006).
101. Egeblad, K., Christensen, C. H., Kustova, M. & Christensen, C. H. Templating Mesoporous Zeolites. *Chem. Mater.* **20**, 946–960 (2008).
102. Möller, K., Yilmaz, B., Jacubinas, R. M., Müller, U. & Bein, T. One-Step Synthesis of Hierarchical Zeolite Beta via Network Formation of Uniform Nanocrystals. *J. Am. Chem. Soc.* **133**, 5284–5295 (2011).
103. Majano, G., Mintova, S., Ovsitser, O., Mihailova, B. & Bein, T. Zeolite Beta nanosized assemblies. *Microporous and Mesoporous Materials* **80**, 227–235 (2005).
104. Chen, L.-H. *et al.* Highly Stable and Reusable Multimodal Zeolite TS-1 Based Catalysts with Hierarchically Interconnected Three-Level Micro–Meso–Macroporous Structure. *Angewandte Chemie International Edition* **50**, 11156–11161 (2011).
105. Möller, K., Yilmaz, B., Müller, U. & Bein, T. Nanofusion: Mesoporous Zeolites Made Easy. *Chemistry – A European Journal* **18**, 7671–7674 (2012).
106. CO2 Emissions From Fuel Combustion Highlights 2013. 158 (2013).
107. What is CCS? – The Carbon Capture & Storage Association (CCSA). http://www.ccsassociation.org/what-is-ccs/.
108. Hedin, N., Andersson, L., Bergström, L. & Yan, J. Adsorbents for the post-combustion capture of CO2 using rapid temperature swing or vacuum swing adsorption. *Applied Energy* **104**, 418–433 (2013).
109. Lee, S.-Y. & Park, S.-J. A review on solid adsorbents for carbon dioxide capture. *Journal of Industrial and Engineering Chemistry* **23**, 1–11 (2015).
110. Aaron, D. & Tsouris, C. Separation of CO2 from Flue Gas: A Review. *Separation Science and Technology* **40**, 321–348 (2005).
111. Montanari, T. & Busca, G. On the mechanism of adsorption and separation of CO2 on LTA zeolites: An IR investigation. *Vibrational Spectroscopy* **46**, 45–51 (2008).
112. Cheung, O. & Hedin, N. Zeolites and related sorbents with narrow pores for CO2 separation from flue gas. *RSC Adv.* **4**, 14480–14494 (2014).
113. Harper, R. J., Stifel, G. R. & Anderson, R. B. Adsorption of gases on 4A synthetic zeolite. *Can. J. Chem.* **47**, 4661–4670 (1969).
114. Breck, D. W., Eversole, W. G., Milton, R. M., Reed, T. B. & Thomas, T. L. Crystalline Zeolites. I. The Properties of a New Synthetic Zeolite, Type A. *J. Am. Chem. Soc.* **78**, 5963–5972 (1956).
115. Yeh, Y. T. & Yang, R. T. Diffusion in zeolites containing mixed cations. *AIChE Journal* **35**, 1659–1666 (1989).
116. Akhtar, F., Liu, Q., Hedin, N. & Bergström, L. Strong and binder free structured zeolite sorbents with very high CO2-over-N2 selectivities and high capacities to adsorb CO2 rapidly. *Energy Environ. Sci.* **5**, 7664–7673 (2012).
117. Palomino, M., Corma, A., Rey, F. & Valencia, S. New Insights on CO2−Methane Separation Using LTA Zeolites with Different Si/Al Ratios and a First Comparison with MOFs. *Langmuir* **26**, 1910–1917 (2010).
118. Hedin, N., Chen, L. & Laaksonen, A. Sorbents for CO2 capture from flue gas—aspects from materials and theoretical chemistry. *Nanoscale* **2**, 1819–1841 (2010).

119. Khoramzadeh, E., Mofarahi, M. & Lee, C.-H. Equilibrium Adsorption Study of CO2 and N2 on Synthesized Zeolites 13X, 4A, 5A, and Beta. *J. Chem. Eng. Data* **64**, 5648–5664 (2019).
120. Zhang, Z., Zhang, W., Chen, X., Xia, Q. & Li, Z. Adsorption of CO2 on Zeolite 13X and Activated Carbon with Higher Surface Area. *Separation Science and Technology* **45**, 710–719 (2010).
121. Brandani, F. & Ruthven, D. M. The Effect of Water on the Adsorption of CO2 and C3H8 on Type X Zeolites. *Ind. Eng. Chem. Res.* **43**, 8339–8344 (2004).
122. Wang, Y. & LeVan, M. D. Adsorption Equilibrium of Carbon Dioxide and Water Vapor on Zeolites 5A and 13X and Silica Gel: Pure Components. *J. Chem. Eng. Data* **54**, 2839–2844 (2009).
123. Dragan, G. The Individual Adsorption of Carbon Dioxide and Sulphur Dioxide by Y Zeolites. *REV. CHIM.* 6 (2010).
124. Yan, J., Yu, D., Li, H., Sun, P. & Huang, H. NaY zeolites modified by La3+ and Ba2+: the effect of synthesis details on surface structure and catalytic performance for lactic acid to acrylic acid. *Journal of Rare Earths* **28**, 803–806 (2010).
125. Pirngruber, G. D., Raybaud, P., Belmabkhout, Y., Čejka, J. & Zukal, A. The role of the extra-framework cations in the adsorption of CO2 on faujasite Y. *Phys. Chem. Chem. Phys.* **12**, 13534–13546 (2010).
126. Bendenia, S., Marouf-Khelifa, K., Batonneau-Gener, I., Derriche, Z. & Khelifa, A. Adsorptive properties of X zeolites modified by transition metal cation exchange. *Adsorption* **17**, 361–370 (2011).
127. Yang, S.-T., Kim, J. & Ahn, W.-S. CO2 adsorption over ion-exchanged zeolite beta with alkali and alkaline earth metal ions. *Microporous and Mesoporous Materials* **135**, 90–94 (2010).
128. Henrique, A., Karimi, M., Silva, J. A. C. & Rodrigues, A. E. Analyses of Adsorption Behavior of CO2, CH4, and N2 on Different Types of BETA Zeolites. *Chemical Engineering & Technology* **42**, 327–342 (2019).
129. You, H.-S., Jin, H., Mo, Y.-H. & Park, S.-E. CO2 adsorption behavior of microwave synthesized zeolite beta. *Materials Letters* **108**, 106–109 (2013).
130. Bonhomme, F., Welk, M. E. & Nenoff, T. M. CO2 selectivity and lifetimes of high silica ZSM-5 membranes. *Microporous and Mesoporous Materials* **66**, 181–188 (2003).
131. Shin, D. W., Hyun, S. H., Cho, C. H. & Han, M. H. Synthesis and CO2/N2 gas permeation characteristics of ZSM-5 zeolite membranes. *Microporous and Mesoporous Materials* **85**, 313–323 (2005).
132. Yu, L., Fouladvand, S., Grahn, M. & Hedlund, J. Ultra-thin MFI membranes with different Si/Al ratios for CO2/CH4 separation. *Microporous and Mesoporous Materials* **284**, 258–264 (2019).
133. Zhu, W., Hrabanek, P., Gora, L., Kapteijn, F. & Moulijn, J. A. Role of Adsorption in the Permeation of CH4 and CO2 through a Silicalite-1 Membrane. *Ind. Eng. Chem. Res.* **45**, 767–776 (2006).
134. Bakker, W. J. W., Broeke, L. J. P. V. D., Kapteijn, F. & Moulijn, J. A. Temperature dependence of one-component permeation through a silicalite-1 membrane. *AIChE Journal* **43**, 2203–2214 (1997).
135. Lovallo, M. C., Gouzinis, A. & Tsapatsis, M. Synthesis and characterization of oriented MFI membranes prepared by secondary growth. *AIChE Journal* **44**, 1903–1913 (1998).
136. van den Broeke, L. J. P., Bakker, W. J. W., Kapteijn, F. & Moulijn, J. A. Transport and separation properties of a silicalite-1 membrane—I. Operating conditions. *Chemical Engineering Science* **54**, 245–258 (1999).
137. Algieri, C., Bernardo, P., Golemme, G., Barbieri, G. & Drioli, E. Permeation properties of a thin silicalite-1 (MFI) membrane. *Journal of Membrane Science* **222**, 181–190 (2003).
138. Zhou, M., Korelskiy, D., Ye, P., Grahn, M. & Hedlund, J. A Uniformly Oriented MFI Membrane for Improved CO2 Separation. *Angewandte Chemie International Edition* **53**, 3492–3495 (2014).
139. Eftekhari, A. & Fan, Z. Ordered mesoporous carbon and its applications for electrochemical energy storage and conversion. *Materials Chemistry Frontiers* **1**, 1001–1027 (2017).
140. Hu, Z., Srinivasan, M. P. & Ni, Y. Preparation of Mesoporous High-Surface-Area Activated Carbon. *Advanced Materials* **12**, 62–65 (2000).
141. Lamond, T. G. & Marsh, H. The surface properties of carbon—III the process of activation of carbons. *Carbon* **1**, 293–307 (1964).
142. Tamai, H., Kakii, T., Hirota, Y., Kumamoto, T. & Yasuda, H. Synthesis of Extremely Large Mesoporous Activated Carbon and Its Unique Adsorption for Giant Molecules. *Chem. Mater.* **8**, 454–462 (1996).
143. Marsh, H. & Rand, B. The process of activation of carbons by gasification with CO2-II. The role of catalytic impurities. *Carbon* **9**, 63–77 (1971).
144. Ozaki, J. *et al.* Novel preparation method for the production of mesoporous carbon fiber from a polymer blend. *Carbon* **35**, 1031–1033 (1997).
145. Kowalewski, T., Tsarevsky, N. V. & Matyjaszewski, K. Nanostructured Carbon Arrays from Block Copolymers of Polyacrylonitrile. *J. Am. Chem. Soc.* **124**, 10632–10633 (2002).
146. Pekala, R. W. Organic aerogels from the polycondensation of resorcinol with formaldehyde. *J Mater Sci* **24**, 3221–3227 (1989).
147. Pekala, R. W., Alviso, C. T., Kong, F. M. & Hulsey, S. S. Aerogels derived from multifunctional organic monomers. *Journal of Non-Crystalline Solids* **145**, 90–98 (1992).

148. Tamon, H., Ishizaka, H., Yamamoto, T. & Suzuki, T. Preparation of mesoporous carbon by freeze drying. *Carbon* **37**, 2049–2055 (1999).
149. Kyotani, T. Control of pore structure in carbon. *Carbon* **38**, 269–286 (2000).
150. Xin, W. & Song, Y. Mesoporous carbons: recent advances in synthesis and typical applications. *RSC Adv.* **5**, 83239–83285 (2015).
151. Knox, J. H., Kaur, B. & Millward, G. R. Structure and performance of porous graphitic carbon in liquid chromatography. *Journal of Chromatography A* **352**, 3–25 (1986).
152. Ryoo, R., Joo, S. H. & Jun, S. Synthesis of Highly Ordered Carbon Molecular Sieves via Template-Mediated Structural Transformation. *J. Phys. Chem. B* **103**, 7743–7746 (1999).
153. Lu, A.-H. & Schüth, F. Nanocasting: A Versatile Strategy for Creating Nanostructured Porous Materials. *Advanced Materials* **18**, 1793–1805 (2006).
154. Liang, C., Li, Z. & Dai, S. Mesoporous Carbon Materials: Synthesis and Modification. *Angewandte Chemie International Edition* **47**, 3696–3717 (2008).
155. Zhang, H., Wang, L., Zhang, D., Meng, X. & Xiao, F.-S. Mesoporous and Al-rich MFI crystals assembled with aligned nanorods in the absence of organic templates. *Microporous and Mesoporous Materials* **233**, 133–139 (2016).
156. Liang, C., Hong, K., Guiochon, G. A., Mays, J. W. & Dai, S. Synthesis of a Large-Scale Highly Ordered Porous Carbon Film by Self-Assembly of Block Copolymers. *Angewandte Chemie International Edition* **43**, 5785–5789 (2004).
157. Liu, L., Wang, F.-Y., Shao, G.-S. & Yuan, Z.-Y. A low-temperature autoclaving route to synthesize monolithic carbon materials with an ordered mesostructure. *Carbon* **48**, 2089–2099 (2010).
158. Fang, Y. *et al.* A Low-Concentration Hydrothermal Synthesis of Biocompatible Ordered Mesoporous Carbon Nanospheres with Tunable and Uniform Size. *Angewandte Chemie International Edition* **49**, 7987–7991 (2010).
159. Wan, Y., Shi, Y. & Zhao, D. Supramolecular Aggregates as Templates: Ordered Mesoporous Polymers and Carbons. *Chem. Mater.* **20**, 932–945 (2008).
160. Benzigar, M. R. *et al.* Recent advances in functionalized micro and mesoporous carbon materials: synthesis and applications. *Chem. Soc. Rev.* **47**, 2680–2721 (2018).
161. Jurewicz, K., Babeł, K., Źiółkowski, A. & Wachowska, H. Ammoxidation of active carbons for improvement of supercapacitor characteristics. *Electrochimica Acta* **48**, 1491–1498 (2003).
162. Lota, G., Grzyb, B., Machnikowska, H., Machnikowski, J. & Frackowiak, E. Effect of nitrogen in carbon electrode on the supercapacitor performance. *Chemical Physics Letters* **404**, 53–58 (2005).
163. Deng, Y., Xie, Y., Zou, K. & Ji, X. Review on recent advances in nitrogen-doped carbons: preparations and applications in supercapacitors. *J. Mater. Chem. A* **4**, 1144–1173 (2016).
164. Mane, G. P. *et al.* Preparation of Highly Ordered Nitrogen-Containing Mesoporous Carbon from a Gelatin Biomolecule and its Excellent Sensing of Acetic Acid. *Advanced Functional Materials* **22**, 3596–3604 (2012).
165. Lin, T. *et al.* Nitrogen-doped mesoporous carbon of extraordinary capacitance for electrochemical energy storage. *Science* **350**, 1508–1513 (2015).
166. Liang, Y., Liu, H., Li, Z., Fu, R. & Wu, D. In situ polydopamine coating-directed synthesis of nitrogen-doped ordered nanoporous carbons with superior performance in supercapacitors. *J. Mater. Chem. A* **1**, 15207–15211 (2013).
167. Li, X. *et al.* Nitrogen-doped ordered mesoporous carbon: Effect of carbon precursor on oxygen reduction reactions. *Chinese Journal of Catalysis* **37**, 1562–1567 (2016).
168. Yang, Y., Lan, G., Wang, X. & Li, Y. Direct synthesis of nitrogen-doped mesoporous carbons for acetylene hydrochlorination. *Chinese Journal of Catalysis* **37**, 1242–1248 (2016).
169. Gao, X. *et al.* Direct Heating Amino Acids with Silica: A Universal Solvent-Free Assembly Approach to Highly Nitrogen-Doped Mesoporous Carbon Materials. *Advanced Functional Materials* **26**, 6649–6661 (2016).
170. Wei, J. *et al.* A Controllable Synthesis of Rich Nitrogen-Doped Ordered Mesoporous Carbon for CO2 Capture and Supercapacitors. *Advanced Functional Materials* **23**, 2322–2328 (2013).
171. Chen, M., Shao, L.-L., Liu, Y.-P., Ren, T.-Z. & Yuan, Z.-Y. Nitrogen-doped ordered cubic mesoporous carbons as metal-free counter electrodes for dye-sensitized solar cells. *Journal of Power Sources* **283**, 305–313 (2015).
172. Lee, J. H., Lee, H. J., Lim, S. Y., Kim, B. G. & Choi, J. W. Combined CO2-philicity and Ordered Mesoporosity for Highly Selective CO2 Capture at High Temperatures. *J. Am. Chem. Soc.* **137**, 7210–7216 (2015).
173. Wang, X. *et al.* Nitrogen-enriched ordered mesoporous carbons through direct pyrolysis in ammonia with enhanced capacitive performance. *J. Mater. Chem. A* **1**, 7920–7926 (2013).
174. Joo, S. H. *et al.* Ordered nanoporous arrays of carbon supporting high dispersions of platinum nanoparticles. *Nature* **412**, 169–172 (2001).
175. Calvillo, L. *et al.* Platinum supported on functionalized ordered mesoporous carbon as electrocatalyst for direct methanol fuel cells. *Journal of Power Sources* **169**, 59–64 (2007).
176. Hu, G. Z. *et al.* Reduction free room temperature synthesis of a durable and efficient Pd/ordered mesoporous carbon composite electrocatalyst for alkaline direct alcohols fuel cell. *RSC Adv.* **4**, 676–682 (2013).

177. Zhou, J. *et al.* NiCl2 assisted synthesis of ordered mesoporous carbon and a new strategy for a binary catalyst. *J. Mater. Chem.* **18**, 5776–5781 (2008).
178. Gong, K., Du, F., Xia, Z., Durstock, M. & Dai, L. Nitrogen-Doped Carbon Nanotube Arrays with High Electrocatalytic Activity for Oxygen Reduction. *Science* **323**, 760–764 (2009).
179. Liang, J., Qiao, S. Z., Lu, G. Q. (Max) & Hulicova-Jurcakova, D. Chapter 18 - Carbon-based Catalyst Support in Fuel Cell Applications. in *Novel Carbon Adsorbents* (ed. Tascón, J. M. D.) 549–581 (Elsevier, 2012). doi:10.1016/B978-0-08-097744-7.00018-1.
180. Yang, Y. *et al.* N-Doped Mesoporous Carbons: From Synthesis to Applications as Metal-Free Reduction Catalysts and Energy Storage Materials. *Front Chem* **7**, (2019).
181. Liu, R., Wu, D., Feng, X. & Müllen, K. Nitrogen-Doped Ordered Mesoporous Graphitic Arrays with High Electrocatalytic Activity for Oxygen Reduction. *Angewandte Chemie International Edition* **49**, 2565–2569 (2010).
182. Kwon, K., Sa, Y. J., Cheon, J. Y. & Joo, S. H. Ordered Mesoporous Carbon Nitrides with Graphitic Frameworks as Metal-Free, Highly Durable, Methanol-Tolerant Oxygen Reduction Catalysts in an Acidic Medium. *Langmuir* **28**, 991–996 (2012).
183. Liu, G., Li, X., Ganesan, P. & Popov, B. N. Development of non-precious metal oxygen-reduction catalysts for PEM fuel cells based on N-doped ordered porous carbon. *Applied Catalysis B: Environmental* **93**, 156–165 (2009).
184. Dorjgotov, A., Ok, J., Jeon, Y., Yoon, S.-H. & Shul, Y. G. Nitrogen-doped ordered porous carbon catalyst for oxygen reduction reaction in proton exchange membrane fuel cells. *J Solid State Electrochem* **17**, 2567–2577 (2013).
185. Dombrovskis, J. K., Jeong, H. Y., Fossum, K., Terasaki, O. & Palmqvist, A. E. C. Transition Metal Ion-Chelating Ordered Mesoporous Carbons as Noble Metal-Free Fuel Cell Catalysts. *Chem. Mater.* **25**, 856–861 (2013).
186. Dombrovskis, J. K. & Palmqvist, A. E. C. One-pot synthesis of transition metal ion-chelating ordered mesoporous carbon/carbon nanotube composites for active and durable fuel cell catalysts. *Journal of Power Sources* **357**, 87–96 (2017).
187. Janson, C., K. Dombrovskis, J. & C. Palmqvist, A. E. Influence of iron precursor hydration state on performance of non-precious metal fuel cell catalysts. *Journal of Materials Chemistry A* **6**, 3116–3125 (2018).
188. Janson, C. & Palmqvist, A. E. C. Improved Oxygen Reduction Activity of Transition Metal-Chelating Ordered Mesoporous Carbon Fuel Cell Catalysts by Milder Template Removal. *Catal Lett* **149**, 1297–1304 (2019).
189. Finsy, R. Particle sizing by quasi-elastic light scattering. *Advances in Colloid and Interface Science* **52**, 79–143 (1994).
190. ISO 22412. Particle size analysis — Dynamic light scattering (DLS). *International Standard* https://www.iso.org/cms/render/live/en/sites/isoorg/contents/data/standard/06/54/65410.html (2017).
191. Mazo, R. M. *Brownian Motion: Fluctuations, Dynamics, and Applications*. *Brownian Motion* (Oxford University Press, 2002).
192. Xu, R. *Particle Characterization: Light Scattering Methods*. (Springer Netherlands, 2002). doi:10.1007/0-306-47124-8.
193. Rhodes G. *Crystallography Made Crystal Clear*. (Academic Press, 2006). doi:10.1016/B978-0-12-587073-3.X5000-4.
194. Goldstein, J. I. *et al. Scanning Electron Microscopy and X-Ray Microanalysis*. (Springer-Verlag, 2018). doi:10.1007/978-1-4939-6676-9.
195. Thommes, M. & Cychosz, K. A. Physical adsorption characterization of nanoporous materials: progress and challenges. *Adsorption* **20**, 233–250 (2014).
196. Brunauer, S., Emmett, P. H. & Teller, E. Adsorption of Gases in Multimolecular Layers. *J. Am. Chem. Soc.* **60**, 309–319 (1938).
197. Schnablegger, H. & Singh, Y. The SAXS guide: Getting acquainted with the principles. *Anton Paar* 14 (2017).
198. Bard A. J. & Faulkner L. R. *Electrochemical Methods: Fundamentals and Applications, 2nd Edition | Wiley*. (John Wiley & Sons, Ltd, 2000).
199. Tsay, C. S. & Chiang, A. S. T. The synthesis of colloidal zeolite TPA–silicalite-1. *Microporous and Mesoporous Materials* **26**, 89–99 (1998).
200. Yang, S. & Navrotsky, A. Early-Stage Reactions in Synthesis of TPA-Silicalite-1: Studies by in Situ Calorimetry, SAXS, and pH Measurements. *Chemistry of Materials* **16**, 3682–3687 (2004).
201. Yang, S. & Navrotsky, A. Early-Stage Reactions in Synthesis of TPA−Silicalite-1 Studies by in Situ Calorimetry, SAXS, and pH Measurements.pdf. (2004).
202. Tokay, B., Somer, M., Erdem-Şenatalar, A., Schüth, F. & Thompson, R. W. Nanoparticle silicalite-1 crystallization from clear solutions: Nucleation. *Microporous and Mesoporous Materials* **118**, 143–151 (2009).
203. Lowe, B. M. An equilibrium model for the crystallization of high silica zeolites. *Zeolites* **3**, 300–305 (1983).
204. Firouzi, A., Atef, F., Oertli, A. G., Stucky, G. D. & Chmelka, B. F. Alkaline Lyotropic Silicate−Surfactant Liquid Crystals. *J. Am. Chem. Soc.* **119**, 3596–3610 (1997).
205. Rimer, J. D., Trofymluk, O., Navrotsky, A., Lobo, R. F. & Vlachos, D. G. Kinetic and Thermodynamic Studies of Silica Nanoparticle Dissolution. *Chemistry of Materials* **19**, 4189–4197 (2007).

206. Cubillas, P. & Anderson, M. W. Synthesis Mechanism: Crystal Growth and Nucleation. in *Zeolites and Catalysis* 1–55 (John Wiley & Sons, Ltd, 2010). doi:10.1002/9783527630295.ch1.
207. Cundy, C. S., Henty, M. S. & Plaisted, R. J. Zeolite synthesis using a semicontinuous reactor, Part 1: Controlled nucleation and growth of ZSM-5 crystals having well-defined morphologies. *Zeolites* **15**, 353–372 (1995).
208. Kashchiev, D. & Rosmalen, G. M. van. Review: Nucleation in solutions revisited. *Crystal Research and Technology* **38**, 555–574 (2003).
209. Persson, A. E., Schoeman, B. J., Sterte, J. & Otterstedt, J.-E. Synthesis of stable suspensions of discrete colloidal zeolite (Na, TPA)ZSM-5 crystals. *Zeolites* **15**, 611–619 (1995).
210. Gevert, B., Eriksson, L. & Törncrona, A. Preparation of discrete colloidal ZSM-5 crystals with high Al-content. *Journal of Porous Materials* **18**, 723–728 (2011).
211. de Ruiter, R., Jansen, J. C. & van Bekkum, H. On the incorporation mechanism of B and AI in MFI-type zeolite frameworks. *Zeolites* **12**, 56–62 (1992).
212. Ghamami, M. & Sand, L. B. Synthesis and crystal growth of zeolite (NH4, TPA)-ZSM-5. *Zeolites* **3**, 155–162 (1983).
213. Ren, N. *et al.* Unusual Pathway of Crystallization of Zeolite ZSM-5 in a Heterogeneous System: Phenomenology and Starting Considerations. *Chem. Mater.* **24**, 1726–1737 (2012).
214. Lindner, T. & Lechert, H. The influence of fluoride on the crystallization kinetics of zeolite NaY. *Zeolites* **14**, 582–587 (1994).
215. Brace, X. & Matijević, E. Coprecipitation of silica with aluminum hydroxide. *Colloid & Polymer Sci* **255**, 153–160 (1977).
216. Fijneman, A. J. *et al.* Multiscale Colloidal Assembly of Silica Nanoparticles into Microspheres with Tunable Mesopores. *Advanced Functional Materials* **n/a**, 2002725.
217. Manoharan, V. N., Elsesser, M. T. & Pine, D. J. Dense Packing and Symmetry in Small Clusters of Microspheres. *Science* **301**, 483–487 (2003).
218. Gustafsson, H. & Holmberg, K. Emulsion-based synthesis of porous silica. *Advances in Colloid and Interface Science* **247**, 426–434 (2017).
219. Wang, Z. *et al.* Direct, single-step synthesis of hierarchical zeolites without secondary templating. *J. Mater. Chem. A* **3**, 1298–1305 (2014).
220. Zhang, X. *et al.* Synthesis of Self-Pillared Zeolite Nanosheets by Repetitive Branching. *Science* **336**, 1684–1687 (2012).
221. Jia, Y. *et al.* Hierarchical ZSM-5 zeolite synthesized via dry gel conversion-steam assisted crystallization process and its application in aromatization of methanol. *Powder Technology* **328**, 415–429 (2018).
222. Naik, S. P., Chiang, A. S. T., Thompson, R. W. & Huang, F. C. Formation of Silicalite-1 Hollow Spheres by the Self-assembly of Nanocrystals. *Chem. Mater.* **15**, 787–792 (2003).
223. Valencia, L. & Abdelhamid, H. N. Nanocellulose leaf-like zeolitic imidazolate framework (ZIF-L) foams for selective capture of carbon dioxide. *Carbohydrate Polymers* **213**, 338–345 (2019).
224. Valencia, L., Rosas, W., Aguilar-Sanchez, A., Mathew, A. P. & Palmqvist, A. E. C. Bio-based Micro-/Meso-/Macroporous Hybrid Foams with Ultrahigh Zeolite Loadings for Selective Capture of Carbon Dioxide. *ACS Appl. Mater. Interfaces* **11**, 40424–40431 (2019).
225. Fujiyama, S., Kamiya, N., Nishi, K. & Yokomori, Y. Adsorption Process of CO2 on Silicalite-1 Zeolite Using Single-Crystal X-ray Method. *Langmuir* **30**, 3749–3753 (2014).
226. Oschatz, M. & Antonietti, M. A search for selectivity to enable CO2 capture with porous adsorbents. *Energy Environ. Sci.* **11**, 57–70 (2018).
227. Kleitz, F., Choi, S. H. & Ryoo, R. Cubic Ia3d large mesoporous silica: synthesis and replication to platinum nanowires, carbon nanorods and carbon nanotubes. *Chem. Commun.* 2136–2137 (2003) doi:10.1039/B306504A.
228. Kinoshita, K. *Carbon: electrochemical and physicochemical properties*. (Wiley, 1988).
229. Fretz, S. J., Janson, C., Rosas-Arbelaez, W. & Palmqvist, A. E. C. Influence of Iron Salt Anions on Formation and Oxygen Reduction Activity of Fe/N-Doped Mesoporous Carbon Fuel Cell Catalysts. *ACS Omega* **4**, 17662–17671 (2019).
230. Dombrovskis, J. K. & Palmqvist, A. E. C. Recent Progress in Synthesis, Characterization and Evaluation of Non-Precious Metal Catalysts for the Oxygen Reduction Reaction. *Fuel Cells* **16**, 4–22 (2016).
231. Osmieri, L. *et al.* Elucidation of Fe-N-C electrocatalyst active site functionality via in-situ X-ray absorption and operando determination of oxygen reduction reaction kinetics in a PEFC. *Applied Catalysis B: Environmental* **257**, 117929 (2019).
232. Taghiabadi, M. M., Zhiani, M. & Silva, V. Effect of MEA activation method on the long-term performance of PEM fuel cell. *Applied Energy* **242**, 602–611 (2019).
233. Osmieri, L., Cullen, D. A., Chung, H. T., Ahluwalia, R. K. & Neyerlin, K. C. Durability evaluation of a Fe–N–C catalyst in polymer electrolyte fuel cell environment via accelerated stress tests. *Nano Energy* **78**, 105209 (2020).
234. Osmieri, L. *et al.* Status and challenges for the application of platinum group metal-free catalysts in proton-exchange membrane fuel cells. *Current Opinion in Electrochemistry* **25**, 100627 (2021).